Vibrational imaging for label-free cancer diagnosis and classification

Renzo Vanna[1*], Alejandro De la Cadena[2], Benedetta Talone[2], Cristian Manzoni[1], Marco Marangoni[1,2], Dario Polli[1,2] and Giulio Cerullo[1,2*]

(1) Istituto di Fotonica e Nanotecnologie - CNR, Milano, Italy

(2) Dipartimento di Fisica, Politecnico di Milano - Milano, Italy

renzo.vanna@ifn.cnr.it, giulio.cerullo@polimi.it

ORCIDs:
Renzo Vanna: 0000-0001-6218-8393
Alejandro De la Cadena: 0000-0001-8951-972X
Benedetta Talone: 0000-0001-6759-3005
Cristian Manzoni: 0000-0002-4169-8869
Marco Marangoni: 0000-0002-0522-149X
Dario Polli: 0000-0002-6960-5708
Giulio Cerullo: 0000-0002-9534-2702

Abstract

The first key step in the detection and classification of most cancers is the microscopic assessment of thin tissue slices, the so-called "histopathology". This procedure is still nowadays, similarly to 150 years ago, performed by staining the tissue with two or more dyes able to bind to specific biological structures, followed by visual inspection by the histopathologist under the bright-field optical microscope. This approach involves long manual procedures which can be accompanied by human errors, subjectivity, and lack of reproducibility.

Vibrational microscopies are capable of directly providing chemical and biomolecular information on tissues, identifying them through their fingerprint vibrational spectra without the need of staining and thus constitute powerful tools for label-free and objective tumour identification. The two most established techniques, spontaneous Raman scattering and infrared absorption microscopy, suffer respectively from long acquisition times and low spatial resolution. These limitations can be overcome by novel and more technically demanding approaches such coherent Raman scattering and photothermal infrared microscopy.

Here we present an extended overview of the major advances in the field of vibrational imaging for cancer diagnosis. We start from a detailed description of the different technologies and then present examples of their applications to tissue imaging for cancer assessment. We critically compare the presented approaches, discussing the steps required to bring these powerful technologies from bench to bedside.

Keywords: hyperspectral, tumours, Raman, FT-IR, SRS, CARS

1. Introduction

Approximately 19 million new cancer cases and 9.6 million cancer deaths have been reported in 2018, according to the most recent report on the global burden of cancer worldwide [1]. In this context, even if prevention and therapeutic interventions have been dramatically improved in the last decades, both incidence and mortality are rapidly increasing, mainly due to increased lifespan and population growth, and diagnosis still plays a major role. Underdiagnosis (failure to recognize carcinoma), overdiagnosis (false positive report) and misdiagnosis (incorrect identification of the tumour type) are associated to late or wrong interventions, unnecessary invasive procedures and enormous costs for national healthcare systems [2,3].

Despite the promising use of blood-based cancer biomarkers - with the approval of just few of them by the Food and Drug Administration (FDA) for clinical use [4] - and the massive investment on non-invasive imaging approaches as screening tools, tissue biopsies are still the current diagnostic gold standard. Biopsies provide access to the most complete morphological, molecular, and genetic information of the investigated lesions, required for the identification of its benign or malignant nature, and for its classification. According to the current guidelines from the World Health Organization (WHO), for the diagnosis of most tumours, the microscopic examination of the tissue (histopathology) is still among the first fundamental diagnostic steps [5–7].

Histopathology was born in 1838, when Johannes Müller pioneered the use of the microscope in pathology, focusing "On Nature and the Structure Characteristics of Cancer", the first book in the field [8]. And this is still the basic principle of histopathology to date: the detailed examination of the histological (tissue) sample by a medically qualified pathologist who formulates a pathological report based on morphological evidence, compared to those reported on available guidelines. In the standard histopathologic workflow, the tissue samples collected from different organs of the patient (so-called biopsies) are chemically processed for fixation (usually overnight), cut into thin slices, chemically stained, positioned within microscope slides, then visually inspected by the histopathologist, usually a few days after sample collection.

The sample preparation workflow is fundamental to guarantee the final quality of the histological assessment. The tissue itself cannot be observed as it is, for many reasons. First, soft tissues must be cut into thin slices (a few μm thickness) to permit sufficient light transmission. In turn, this requires tissues to be embedded into a denser material (usually paraffin wax) to preserve their structure during the cutting procedure. Second, biological structures and biomolecules need to be preserved from the decay induced by interaction with microorganisms or enzymatic autolysis, which requires their stabilization to enable long-term use and make them compatible with specific staining or labelling procedures. In the standard slide preparation protocol, tissues are first saturated with formalin and then embedded in a paraffin wax block, according to the so-called formalin-fixed paraffin embedded (FFPE) procedure. The obtained tissue block is then cut by a microtome into thin slices, which are subjected to the staining process. The FFPE protocol is the most widespread approach and provides the highest quality for histologic images; in addition, FFPE samples are very stable and can be archived for decades in the so-called "biobanks", for further consultation during patient treatment and for legal purposes. On the other hand, FFPE is laborious and time consuming and the process denatures the tissue proteins, preventing their identification by labelled antibodies.

An alternative tissue preparation protocol consists in rapidly cooling the excised tissue (fresh or snap freezing) for fixation and slice cutting. Frozen tissues can be cut equally well by a dedicated microtome, called cryostat, and subjected to standard staining procedure, bypassing the lengthy FFPE approach thus possibly saving up to 2-3 days. This method is typically used in an intraoperative setting when a rapid lesion assessment is required to guide the

surgical intervention. In this case, the samples are processed and examined immediately (between 20 to 40 min), using approaches which deliver quick information but with a poorer morphological quality, due to a limited fixation process and consequent suboptimal staining results. On the other hand, snap freezing protocols preserve the native non-denatured structure of proteins and preserve most of lipid vacuoles, which are normally removed during FFPE protocols due to the extended use of solvents. Despite these advantages, fresh frozen slices are typically used only for intraoperative assessment and not for routine diagnosis because, for observation of stained tissue slices using standard light microscopies, the morphological and staining quality (see below) guaranteed by the FFPE procedure is more important than the preservation of biochemical features guaranteed by snap freezing. However, a higher priority to fresh-frozen samples and their benefits could be given with the advent of new imaging approaches based on the direct detection of biomolecules, such as those based on vibrational contrast, described in the next sections.

Once the tissue has been fixed and cut into thin slices, the detailed morphological features are still almost invisible, due to the lack of an intrinsic contrast detectable by the sole visible light, so that staining with suitable dyes is required. The haematoxylin and eosin (also known as H&E) staining technique is the gold standard in histopathology laboratories since nearly 125 years [8] and allows the pathologist to distinguish a wide range of normal and abnormal cell and tissue components. Haematoxylin marks the cell nuclei in purple/blue, while eosin gives a pink colour to the cytoplasm and the extracellular connective tissue matrix, with other tissue structures assuming different hues and combinations of these colors.

Tissue staining gives a "structural" information on the tissue, showing its general morphology, the cells distribution and the nuclei to cytoplasm ratio, i.e. the so-called histoarchitecture. Once the staining raises the suspicion of a certain disease, more specific stains or labelling procedures can be applied, for example using antibodies targeted to specific antigens (e.g., proteins, nucleic acids) in the tissue, in the so-called immunostaining approaches. The antibody can be visualized by conjugating it either to a fluorophore such as rhodamine or fluorescein (a method so called "immunofluorescence") or, more commonly for diagnosis, to an enzyme able to produce a coloured precipitate (a method so called "immunohistochemistry" (IHC)). Immunostaining provides a biological information on the sample, allows identifying the distribution and concentration of specific biomarkers, and is typically applied to confirm the diagnosis or to accurately determine the tumour type (grading and staging). However, it is an expensive and long procedure, sometimes based on several optimization steps. Furthermore, for every biomarker to be detected a different immunostaining experiment needs to be performed on a dedicated tissue slice.

Traditionally, H&E-stained or immune-labelled tissue slides are diagnosed by direct visual inspection under the microscope. This approach, besides its subjective nature, requires the action of the pathologist, a highly specialized professional figure. Though representing the current state of the art in pathological diagnostics, H&E and immune staining approaches are neither quantitative nor objective, as they rely upon the opinion of the pathologist. The ideal diagnostic approach for tissue samples would thus include fast sample preparation, reproducibility, and an objective and accurate evaluation.

Very recently, a number of limitations associated to H&E (or similar) staining procedures have been overcome by the introduction of digital pathology (DP), which performs high resolution scanning of the tissue slide and generates a digital image consisting of a matrix of optical density data [9]. In a digital microscope, also known as whole-slide scanner (WSS), a high-resolution image is acquired over a comparatively small field of view (FOV) of the tissue slide, of the order of 200×200 μm, and multiple images obtained by translating the slide are stitched together to reconstruct a whole-slide image (WSI) in a tile-based mosaic pattern. The WSI provides to the pathologist in principle the same information that he/she would obtain by visual inspection under the microscope, but with important

advantages: i) the digital image, despite its large size (several GBs), can be easily transmitted over large distances, enabling prompt diagnosis of samples collected in remote areas, provided that a whole slide scanner is available (telepathology); ii) the same image can be submitted to several pathologists, enabling them to compare their diagnoses and improve accuracy/objectivity through a consensus report; iii) WSI data can easily be stored and retrieved for later consultation, in a much more convenient way than the physical tissue slides in the biobank. DP has only very recently gained FDA approval for diagnostic use, after a multi-center study involving 1992 patients with different tumor types and 16 surgical pathologists showed it not inferior to traditional microscope based approaches [10].

Most importantly, the digital images provided by DP can be analyzed using computer algorithms, which can provide spatial relationships between different cellular or stromal components, such as cell nucleus, cytoplasm and membrane, allowing for more precise association of the tissue morphology to a specific phenotype or pathology. Artificial intelligence (AI) may be particularly powerful in this context, especially machine learning (ML) approaches that, by continuously feeding data to the machine and going through a sequence of training cycles, train it to make safe predictions [11]. Of particular interest are deep learning (DL) approaches, which make use of neural networks (NNs) connecting an input layer to an output layer through a series of hidden layers. DL has already been applied to the analysis of DP data. While DP can alleviate some of the shortcomings of histopathology, at least by improving objectivity, the information content is fundamentally similar to that of H&E - and mainly of morphological nature – and also issues related to sample preparation are identical.

In the last three decades vibrational spectroscopies have shown the capability to directly provide chemical and biomolecular information (and image contrast) on tissues and cells, identifying them through their fingerprint vibrational spectra without the need of staining and labelling, and virtually without any additional sample preparation step (here we suggest three general review articles on vibrational based approaches for biomedical applications [12–14]). Vibrational-based microscopy approaches are non-contact, non-invasive and non-destructive methods. Every component of a biological specimen is characterized by a vibrational spectrum made up of several peaks with different frequencies and amplitudes, each representing a specific chemical bond found within the tissues and cells being measured (see **Fig. 1**). This includes the four main biological macromolecules (i.e. nucleic acids, proteins, lipids and carbohydrates) but also the so called "small molecules", generally defined as smaller than 900 Da (i.e., g/mol) (e.g. small hormones, metabolites, etc.) that are hardly visible by standard staining or immunolabeling approaches. The vibrational spectrum is a superposition of all these peaks and provides a detailed picture of the biochemical composition of the cells and tissues being measured. These endogenous and chemically specific molecular fingerprints thus become reliable biomarkers, allowing crucial properties/phenotypes of cells (e.g., subtype, differentiation, cell cycle state) and tissues (e.g. normal, cancerous, extracellular matrix content) to be identified, and used for cancer diagnosis and classification.
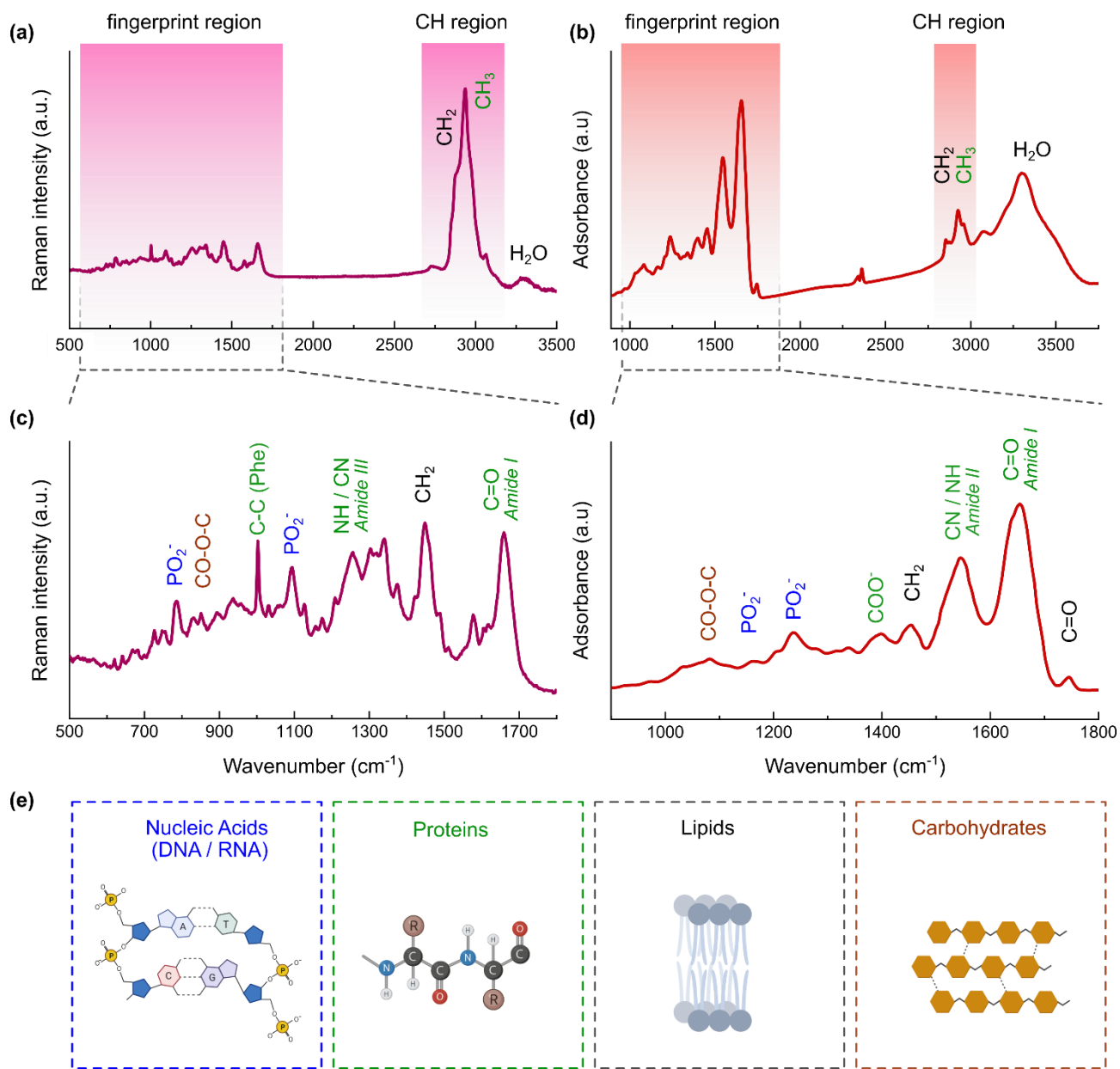
Fig. 1 representative biological Raman (**a**) and IR (**b**) spectra in the respective typical full ranges and the corresponding fingerprint region (**b** and **d**, respectively). The peak assignments are reported for the most representative and abundant chemical bonds in biological samples, belonging to the four major biological molecules (**e**). Both Raman and infrared (IR) spectra were plotted using the same x-axis orientation for clarity even if IR are typically plotted with decreasing wavenumbers. The Raman spectrum was collected by the authors using a home-built spontaneous Raman microscope (Prof. Cees Otto group, Twente University, NL; ref. [15]. The IR spectrum was collected using a FT-IR microscope and kindly provided by Prof. Nick Stone and colleagues (Exeter University, UK). Both spectra are the average of multiple spectra, wavenumber and intensity calibrated, without further processing steps. a.u.: arbitrary units. Created with BioRender.com.

Measuring the vibrational spectrum at every pixel allows one to identify simultaneously the above-mentioned target molecules or macromolecules and to map their distribution within tissues in a completely non-destructive and label-free way. This information can then be used to generate false-color images, possibly mimicking those obtained by the standard H&E approach, and to which histopathologists are used. This approach is called virtual histopathology, as it enables to obtain images comparable to H&E staining but without the need to add any labels

to the tissue slide. Virtual histopathology has the potential to work on fresh unprocessed samples, which is especially important for an intra-operative setting; in addition, it provides a digital information that can be achieved and shared, similar to DP, avoiding the operator-dependent staining procedure and thus enhancing reproducibility. However, it fundamentally delivers the same kind of structural information on the tissue architecture that is provided by H&E, or by similar approaches. Recording the full vibrational spectrum (or even single disease-related frequencies) for every pixel of the image has however the potential to deliver an information which goes well beyond that provided by standard approaches. This so-called "spectral histopathology" approach would disclose an unprecedented level of detail on the biochemical composition of the cells and tissues, combining the structural information of H&E with the detailed biomolecular information provided by the biochemical profile of the sample.

Spectral histopathology, being an imaging approach, sets rather demanding requirements on the vibrational microscopy technique: i) high spatial resolution (up to 400-500 nm), comparable to that of standard H&E, in order to possibly visualize the internal structure of cells; ii) broad spectral coverage to enable molecular identification; iii) high acquisition speed, enabling to scan a tissue slide, or a diagnostically significant portion of it, in a time of the order of minutes to a few hours, compatible with the standard histopathology workflow.

Coming back to vibrational spectroscopies enabling spectral histopathology, we can introduce two main complementary players: Raman microscopy, also called spontaneous Raman (SR) microscopy, and infrared (IR) absorption microscopy. Raman microscopy (better detailed in **section 2.1**) measures the inelastically scattered light (Stokes) from vibrations which involve a change in the molecular polarizability (the so-called Raman-active modes) (**Fig. 2**a). IR microscopy (better detailed in **section 2.3**) directly measures the absorption in the mid-infrared range ($\approx$2.5-25 μm wavelength) of vibrational transitions which involve a change in the dipole moment (the so-called IR-active modes) (**Fig. 2**d). While the selection rules for IR and Raman active transitions are different and (generally) complementary, both yield comparable spectroscopic information on the bio-chemical nature of the interrogated sample (between 500-3200 cm^{-1}) (see **Fig. 1**).

SR and IR microscopy each have advantages and drawbacks. In a nutshell, SR provides very good spatial resolution, as it makes use of visible light which can be focused to diffraction-limited spots of 500 nm or smaller, combined with very rich chemical information, as it records a full vibrational spectrum, with little or no interference by water signals. On the other hand, it comes with a very low acquisition speed due to the very small cross-section of the SR process (only one over 10^9-10^{12} incident photons is inelastically scattered), preventing acquisition of high-spatial resolution images in a short time. IR microscopy, on the other hand, exploits the very large absorption cross sections of vibrational transitions to produce intense signals, allowing in principle high acquisition speeds; however, the long IR wavelengths and the low numerical aperture of IR objectives typically limit the spatial resolution to 4-5 μm, which is about one order of magnitude worse than for SR and standard H&E staining and comparable to the size of a cell, thus preventing the imaging of intra-cellular structures. In addition, the IR absorption of water is significant in a rather large part of the fingerprint region, thus limiting the study of water-containing samples (e.g. cells or fresh/frozen tissues).

There are however more advanced vibrational microscopy techniques that, at the price of an increased technical complexity, overcome some limitations of SR and IR microscopies. Coherent Raman Scattering (CRS) microscopy, including stimulated Raman scattering (SRS) and coherent anti-Stokes Raman scattering (CARS) (better detailed in **Section 2.2**) generates the Raman signal from a coherent superposition of the molecular vibrations induced by two synchronized ultrashort laser pulses of different color, the pump (at frequency ω_p) and the Stokes (at frequency ω_s)

1 (**Fig. 2**b,c). When the difference between pump and Stokes frequencies matches a vibrational frequency Ω, then all
2 molecules in the focal volume are resonantly excited and vibrate in phase. This vibrational coherence enhances the
3 Raman response by many orders of magnitude with respect to the incoherent SR process, thus decreasing the
4 acquisition times by several orders of magnitude.

5 Photo-thermal IR (PT-IR) microscopy (better detailed in the **Section 2.4**) is a very recent variant of IR microscopy
6 which uses a pump-probe approach, imaging the local thermal effect induced by the absorbed IR radiation using a
7 visible probe beam. In PT-IR microscopy, an IR pump beam heats the sample by selective resonant excitation of a
8 vibrational transition (**Fig. 2**e). The heating results in a change of the sample refractive index, inducing a phase shift
9 on a co-propagating visible probe beam that is measured by the detector giving a signal proportional to the
10 absorbed IR power. The PT-IR approach elegantly combines the high spatial resolution (<400 nm) given by the visible
11 probe beam with the vibrational sensitivity afforded by selective IR excitation of the molecular vibration of interest.
12 CRS and PT-IR microscopies are currently under intense technological development, with rapid improvements in
13 acquisition speed, sensitivity and spectral coverage being constantly reported.

14

15   **a** - RAMAN SCATTERING   **b** - SRS   **c** - CARS   **d** - IR ABSORPTION   **e** - Photothermal effect
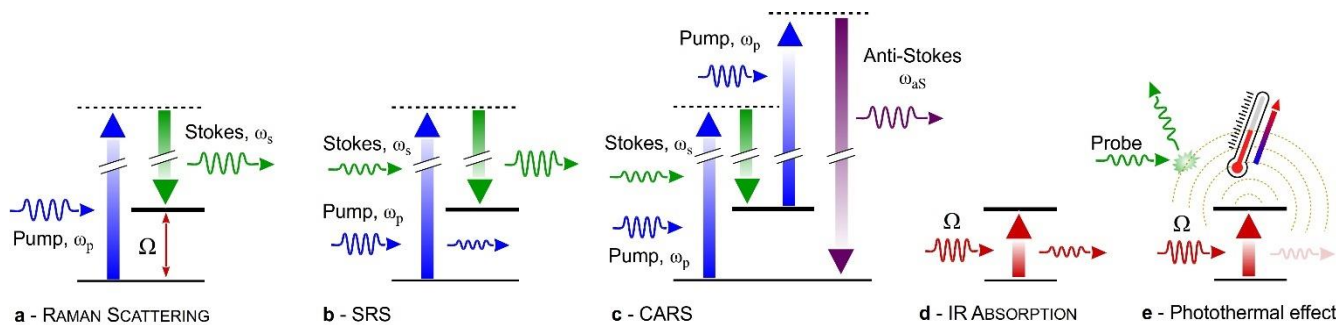
16 **Fig. 2**: sketch of the transitions involved in the different vibrational spectroscopies of a level of frequency Ω. Dashed lines
17 represent virtual levels involved in the transitions. **a** Spontaneous Raman scattering; **b** Stimulated Raman Scattering (SRS); **c**
18 Coherent anti-Stokes Raman Scattering (CARS); **d** infrared (IR) absorption; **e** Photothermal effect, the energy stored after IR
19 absorption produces localized temperature increase.

20

21 This paper aims at extensively reviewing the state of the art of label-free vibrational spectroscopies for biomedical
22 applications and their application to virtual and spectral histopathology for label-free tumor identification. Section
23 2 discusses in detail the physics, the operating principles, the performance, and the limitations of the four
24 vibrational microscopy techniques introduced above: SR, CRS, IR and PT-IR. Section 3 presents examples of
25 application of vibrational microscopies to tissue imaging and cancer diagnosis by a quasi-historical approach, thus
26 focusing on the most relevant steps in this field. Finally, Section 4 briefly compare the state of the art of the different
27 techniques and devises some perspectives for future developments.

28

1 **2. Vibrational microscopy techniques**

2 **2.1 Spontaneous Raman microscopy**

3 SR microscopy exploits the Raman effect, i.e., an inelastic frequency shift on the scattered light relative to the
4 incident radiation originated from an exchange of energy between photons and molecular vibrations. This inelastic
5 light-matter interaction is the result of three simultaneous events: (i) the annihilation of a photon from the incident
6 field with energy $\hbar\omega_p$ upon interaction with the molecule; (ii) a vibrational transition of the interacting molecule
7 with energy $\hbar\Omega$; (iii) the spontaneous emission of a second red-shifted "Stokes" photon with energy $\hbar\omega_S$. A classical
8 description cannot fully explain the SR effect, yet it is adequate to illustrate its conceptual basis. Within the classical
9 approximation, the electric field $E = E_0\cos(\omega_p t)$ of a monochromatic plane wave of amplitude E_0 and frequency ω_p
10 drives the electron-cloud of the molecule, inducing an electric dipole μ:

11 $$\mu(t) = \alpha(t)E(t) \qquad \textbf{(1)}$$

12 where $\alpha(t)$ is the polarizability of the molecule [16] (**Eq. 1,** this and most equations reported in this sub-section
13 were adapted from [17]); the driven dipole in turn radiates a light field. The nuclear motions of the optically
14 perturbed molecule are responsible for the time-varying $\alpha(t)$, making it dependent on the molecular coordinate
15 $x(t)$. Assuming that the nuclei of the molecule vibrate near their equilibrium positions according to a harmonic
16 motion $x(t) = x_0\cos(\Omega t)$ of amplitude x_0 and frequency Ω, a Taylor expansion allows to express the polarizability
17 around its equilibrium configuration α_0 as:

18 $$\alpha(t) \approx \alpha_0 + \left(\frac{\partial \alpha}{\partial x}\right)_{x=0} x(t) \qquad \textbf{(2)}$$

19 As we assumed small nuclear displacements, we neglected high order terms in **Eq. 2**. By inserting **Eq. 2** into **Eq. 1**
20 and making use of basic trigonometry it is easy to show that the induced dipole moment contains three different
21 frequency components, namely ω_p, $\omega_p-\Omega$, and $\omega_p+\Omega$. As a consequence of the radiative nature of an oscillating
22 dipole, the first term leads to the generation of light with the same frequency of the incident radiation, i.e. ω_p,
23 known as elastic (Rayleigh) scattering. The second term generates red-shifted light known as Stokes radiation, while
24 the third term causes blue-shifted light known as anti-Stokes radiation. Thus, relative to the monochromatic
25 excitation field, the inelastically scattered radiation either increases or reduces its frequency by an amount equal
26 to that of the vibrational mode of the interacting molecule, i.e., $\omega_p \pm \Omega$. Since the population of scatterers follows a
27 Boltzmann distribution, with lowest energy levels occupied at thermal equilibrium, the Stokes component results
28 to be much more intense than the anti-Stokes component, which is why Stokes photons are typically detected in
29 SR microscopy.

30 It is useful to express the intensity of the SR signal at the Stokes frequency in terms of a SR cross section $\sigma_{SR}(\omega_S)$,
31 which is similar to the absorption cross section in Lambert-Beer's law:

32 $$I_{SR}(\omega_S) = Nz\sigma_{SR}(\omega_S)I_0 \qquad \textbf{(3)}$$

33 where N is the volume density of scatterers and z is the sample thickness. Due to the very small Raman-scattering
34 cross section ($\sigma_{SR}(\omega_S)$), typically around 10^{-30} cm^2, the number of SR photons is typically a minimal fraction of the
35 Rayleigh scattered photons or the photons emitted by fluorescence [18]. Therefore, the Rayleigh scattering and
36 fluorescence background may hamper the detection of SR scattering. The low scattering cross section also
37 drastically reduces the acquisition speed of SR relative to other imaging techniques, such as fluorescence

1   microscopy. Nevertheless, SR microscopy has the remarkable advantages of combining high spatial resolution
2   ($\approx$300-400 nm) with rich spectral information and of being technically simple to be implemented.

3   Although Brillouin [19] and Smekal [20] theoretically predicted the inelastic scattering of light, it was Raman and
4   Krishnan [21] who experimentally observed such effect using as a light source a focused sunlight beam. The
5   invention of the laser in the early '60s [22] spurred an ever growing development of Raman spectroscopy. By the
6   end of that decade, the progress in Raman spectroscopy allowed the observation of the Raman effect with a
7   diffraction-limited spatial resolution, starting the field of Raman-microspectroscopy. Thus, by the mid-1970s, the
8   first reports on the development and application of Raman-microscopy emerged [23]. At the end of the very same
9   decade, this progress led to the first commercial Raman microscopes [24].

10 The conceptual scheme of a basic SR microscope in the so-called point scanning configuration is rather simple and
11 consists of four fundamental elements, as illustrated in **Fig. 3**: a relatively intense monochromatic laser beam, a
12 high numerical-aperture objective to tightly focus the beam and collect the generated SR signal, a sequence of long-
13 pass optical filters to remove the Rayleigh-scattered light, and a grating-based dispersive spectrometer (typically
14 associated to a CCD detector) to record the SR spectrum. This configuration provides an SR spectrum for each
15 raster-scanned position of the sample. This architecture has not changed significantly in the last four decades;
16 however, technological advances (see Ref. [25] for a detailed discussion) have allowed increasing the acquisition
17 speed by nearly three orders of magnitude. The monochromatic excitation beam is generated by a continuous wave
18 laser of a few tens of mW power, usually in the visible and near infrared range (e.g. 532, 633, 785, 1063 nm),
19 depending on the application and on the setup configuration. For most studies on tissue samples, near-infrared
20 wavelengths (e.g., 785 nm) are preferred as they reduce auto-fluorescence of the sample.

21 A high numerical aperture (NA) microscope objective is used to illuminate the sample and to collect the backward
22 scattered SR light (epi detection), which is then directed to the spectrometer. Epi detection is preferred because it
23 is simpler, requiring only one microscope objective, and because the spatially incoherent SR light is radiated
24 isotropically in all directions, including the backscattered light which is easily collected by the same objective. The
25 geometry of point-scanning microscopes is well suited for confocal SR microscopy [26,27], in which an iris,
26 conjugated with the object plane and with the entrance slit of the spectrometer, reduces fluorescence background.
27 Thus, with synchronized readings of spatial coordinates and spectra, point-scanning microscopes generate a Raman
28 spectrum per point of the image with diffraction-limited spatial resolution and spectral-resolution down to 1 cm^{-1}.
29 This rich dataset, containing one spectrum per image pixel, is known as hyperspectral data cube or hypercube. The
30 point-scanning architecture is the conventional one used for SR microscopes, as shown in **Fig. 4**a. Alternative SR
31 modalities are line scanning and wide-field-excitation (see **Fig. 4**b,c).
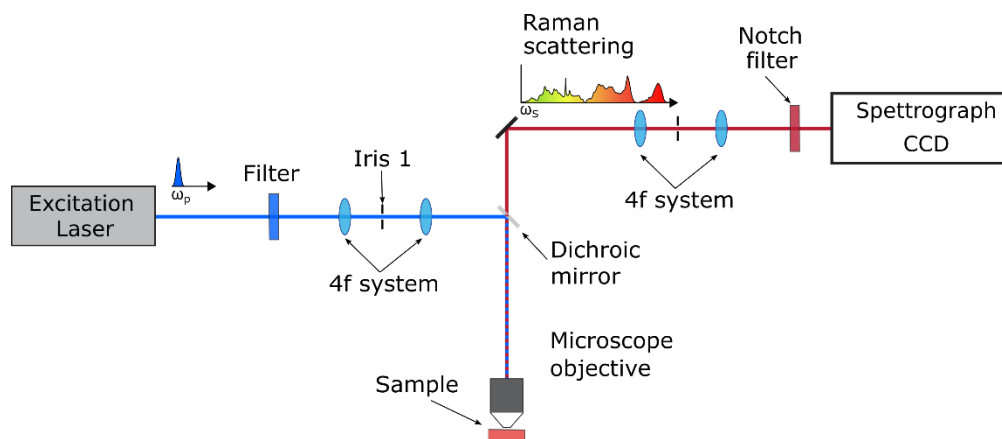
32

Fig. 3 Schematic lay-out of a SR microscope. Adapted with permission from [28]. CCD: charge coupled device.

Line-scanning microscopes focus a line of light onto the specimen and acquire the SR signal simultaneously from all illuminated points. There are two common approaches to generate a line profile at the focal plane. The first one employs a galvanometric scanner that quickly moves a tightly focused beam over a line on the sample plane, with a scanning rate higher than the sampling rate of the detector. The second approach attains the line illumination by focusing with a cylindrical lens. In both approaches, collection optics images the line-shaped SR signal onto the slit of a dispersive spectrometer in such a way that a matrix-detector, typically a CCD, may register the Raman-spectrum along one direction (e.g. rows) and the spatial location along the other direction (e.g. columns). This allows a parallel measurement of the SR spectra of all points of the illuminated line before moving the excitation to a second line (push-broom imaging). To this end, either a single-axis galvanometer scanner moves the excitation line, or a mechanical stage displaces the specimen. In both cases the scanning is uniaxial. In the geometry shown in **Fig. 4b** the scanning takes place along the *x*-axis. As compared to a point-scanning configuration, line-scanning increases the acquisition speed of the Raman hypercube. In particular, if a point-scanning microscope performs N×N measurements to retrieve the Raman hypercube, its line-scanning counterpart requires only N measurements. However, due to the line profile of the excitation and of the scattered light, line-scanning microscopes are not entirely confocal, hampering the rejection of fluorescence and out-of-focus contributions. The implementation of line-scanning Raman microscope dates back to the 1970s, but it was not until the recent development of two-dimensional CCDs that applications with substantial impact on the biomedical sciences were shown [29]. Stone and collaborators, and Renishaw Plc. (UK), reported a similar line-mapping approach based on the use of an expanded line-focused laser coupled with a CCD readout synchronized with the movement of the stage [30]. Fujita and colleagues [31,32] have also demonstrated the potential of the line-scanning architecture by employing it to observe molecular dynamics in living cells.

Wide-field-excitation SR microscopes, shown in **Fig. 4c**, distribute the excitation light homogeneously over the sample plane, while a CCD camera records the SR signal at a specific vibrational frequency. Early reports on the applications of this architecture selected the imaged Raman bands using narrow-band tunable lasers coupled with narrow-band fixed filters, rotating filters, or dispersive gratings [28,33]. The introduction of liquid-crystal tunable filters [34] and acousto-optical tunable filters [35] invigorated the development of wide-field-excitation SR microscopy, as these technologies allow automatized imaging at Raman-bands of interest with enhanced spectral resolution. Schlucker et al. [36] systematically compared wide-field Raman-microscopy with point-scanning and line-scanning regimes. The researchers noted that, despite the necessity to collect several images at different

vibrational frequencies to assemble an entire Raman-hypercube, wide-field SR microscopy, at a specific Raman band, outperforms single-point and line-scanning architectures in terms of speed and image quality. To date, widefield-excitation for SR microscopy has found limited applications in biosciences, succeeding only in imaging tissues containing calcified material, which produces strong Raman signals [37,38].

Despite their appealing characteristics, modern SR microscopes still suffer from one main pitfall: due to the low Raman cross-sections and the lack of coherence among the individual dipole moments that originate the scattered photons, they are still slow for tissue imaging.
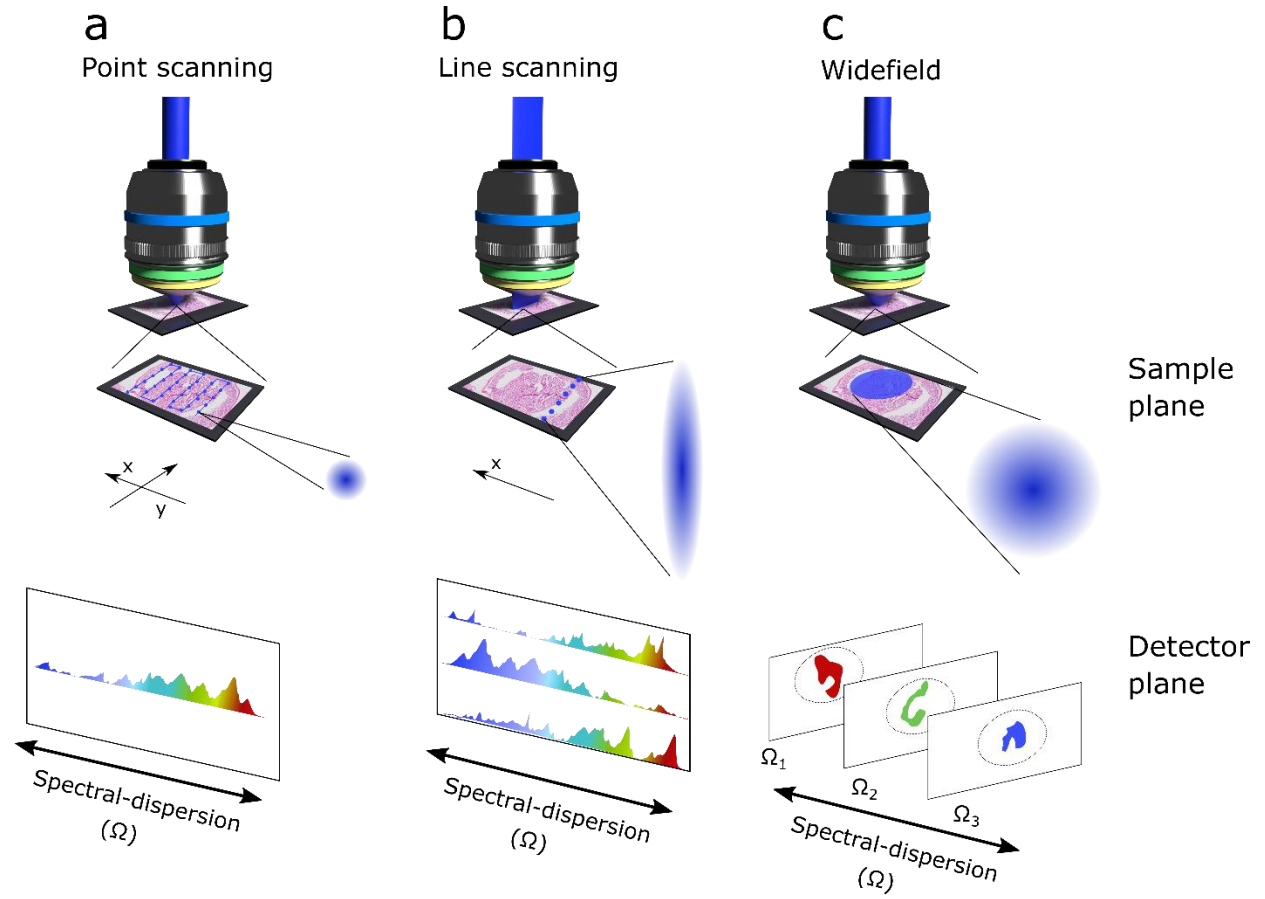
Fig. 4 Architectures for Raman-microscopy. **a** point-scanning, **b** line-scanning, and **c** wide-field excitation. The second row shows a magnified view of the sample-plane and the irradiance on the sample. The third row depicts the spectral information obtained from each architecture.

1 **2.2 Coherent Raman microscopy**

2 **2.2.1 Fundamental principles**

3 CRS is a class of third-order nonlinear optical processes which generates the Raman signal from a coherent
4 superposition of oscillating molecular dipoles in the sample, illuminated by two synchronized ultrashort laser
5 pulses of different frequencies, the pump (at frequency ω_p) and the Stokes (at frequency ω_S). When the
6 difference between pump and Stokes frequencies matches a vibrational frequency Ω, i.e. $\omega_p - \omega_S = \Omega$, then all
7 the molecules in the focal volume are resonantly excited and vibrate in phase. This vibrational coherence is the
8 key aspect, which differentiates CRS from the incoherent SR process, as it enhances the Raman response by many
9 orders of magnitude, decreasing the acquisition times from seconds down to microseconds per pixel. The two
10 most widely employed CRS techniques are CARS [39] and SRS [40,41] (**Fig.5**). In SRS (**Fig. 5**b) the coherent
11 interaction with the sample induces stimulated emission from a virtual state of the sample to the investigated
12 vibrational state, resulting in a Stokes-field amplification (Stimulated Raman Gain, SRG) and in a simultaneous
13 pump-field attenuation (Stimulated Raman Loss, SRL). In CARS (**Fig. 5**c) the vibrational coherence is read out by
14 a further interaction with the pump beam, generating a coherent radiation at the anti-Stokes frequency $\omega_{aS} = \omega_p$
15 $+ \Omega$, which is detected by spectrally filtering it from the co-propagating pump and Stokes beam.

16

17   **a** - RAMAN SCATTERING   **b** - SRS   **c** - CARS
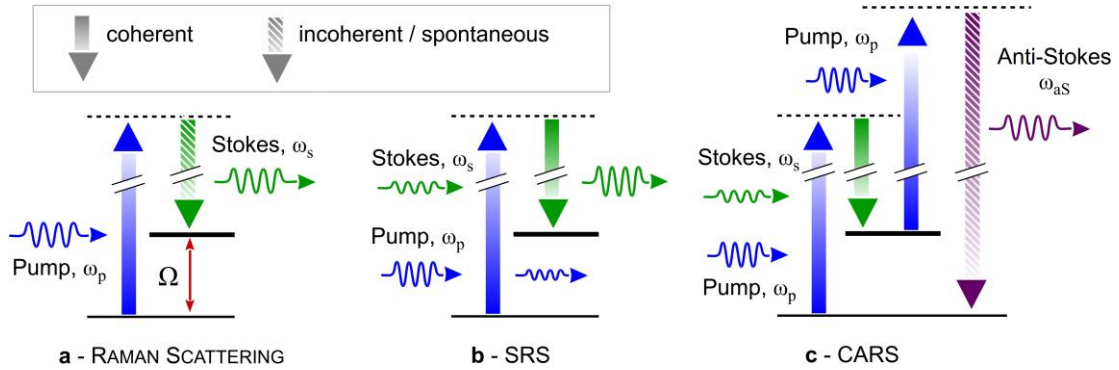
18 **Fig. 5** sketch of the transitions involved in coherent CRS based approaches, compared with those involved in
19 spontaneous Raman scattering. Dashed lines represent virtual levels involved in the transitions. **a** Spontaneous Raman
20 scattering; **b** Stimulated Raman Scattering (SRS); **c** Coherent anti-Stokes Raman Scattering (CARS).

21

22 CARS and SRS are four-wave-mixing (FWM) processes, of the type $\omega_1 + \omega_3 = \omega_2 + \omega_4$, mediated by the third-order
23 nonlinear optical response of the sample, which can be generally written as:

24
$$\chi^{(3)}(\omega) = \chi_{NR}^{(3)} + \chi_R^{(3)}(\omega) \qquad \textbf{(4)}$$

25 where $\omega = \omega_p - \omega_S$ (this and most of equations reported in this sub-section were adapted from [17,42]). The term
26 $\chi_{NR}^{(3)}$, also known as non-resonant background (NRB), describes the non-resonant electronic interactions of the
27 pump and Stokes fields with the molecules under study and with the surrounding environment, and is typically
28 assumed to be real and frequency independent. The resonant term $\chi_R^{(3)}(\omega)$ is the complex vibrational
29 susceptibility, which contains the chemical information on the sample, and can be written as a sum of Lorentzian
30 responses:

$$\chi_R^{(3)}(\omega) = \sum_i \frac{A_i}{\Omega_i - \omega - i\Gamma_i} \qquad \textbf{(5)}$$

where for the ith vibrational resonance, the amplitude $A_i \propto \sigma_i N_i$ is proportional to the cross section (σ_i) and to the volume concentration of molecular bonds (N_i), Ω_i is the vibrational frequency, and Γ_i the corresponding linewidth.

In a generic FWM process, the third-order polarization at frequency $\omega_4 = \omega_1 + \omega_3 - \omega_2$ can be expressed as:

$$P^{(3)}(\omega_4) \propto \chi^{(3)}(\omega_1, \omega_2, \omega_3, \omega_4) E_1(\omega_1) E_2^*(\omega_2) E_3(\omega_3) \qquad \textbf{(6)}$$

and the equation describing the evolution of the light field at ω_4 along the propagation direction z can be written as:

$$\frac{\partial E_4}{\partial z} = -i \frac{3\omega_4}{4cn_4} P^{(3)}(\omega_4) e^{i\Delta kz} \qquad \textbf{(7)}$$

where c is the speed of light, n_4 the refractive index of the medium at frequency ω_4 and $\Delta k = k_4 + k_2 - k_1 - k_3$ is the so-called wave vector mismatch.

In the CARS process one has $\omega_1 = \omega_3 = \omega_p$, $\omega_2 = \omega_S$, $\omega_4 = 2\omega_p - \omega_S = \omega_{aS}$. In a tight focusing configuration characteristic of microscopy, leading to a short interaction length $L \approx 1$ μm, one can neglect the phase mismatch between the interacting fields ($\Delta kL \approx 0$) and write the anti-Stokes field as:

$$E_{aS}(\omega_{aS}) \propto -i\chi^{(3)}(\omega_p - \omega_S) E_p^2(\omega_p) E_S^*(\omega_S) \text{L} \qquad \textbf{(8)}$$

Since the anti-Stokes field is at a different frequency with respect to pump and Stokes, its intensity can be directly measured following spectral filtering and is:

$$I_{CARS}(\omega_{aS}) \propto \left| \chi^{(3)}(\omega_p - \omega_S) \right|^2 I_p^2(\omega_p) I_S(\omega_S) L^2 =$$

$$= \left[\left| \chi_R^{(3)}(\omega_p - \omega_S) \right|^2 + \chi_{NR}^{(3)2} + 2\chi_{NR}^{(3)} Re\left[\chi_R^{(3)}(\omega_p - \omega_S) \right] \right] I_p^2(\omega_p) I_S(\omega_S) L^2 \qquad \textbf{(9)}$$

Equation 9 shows both the advantages and the drawbacks of CARS. On the one hand, CARS has the important advantage of being a background-free process, as its signal is measured against a zero linear background, thus making its detection very easy. On the other hand, the NRB significantly affects the CARS spectrum, by introducing both a frequency independent term ($\chi_{NR}^{(3)2}$) and a dispersive interference term $2\chi_{NR}^{(3)} Re\left[\chi_R^{(3)}(\omega_p - \omega_S) \right]$ that distorts the typical Lorentzian peaked lineshapes of SR spectra.

One can consider two limiting cases. If $\chi_{NR}^{(3)} \ll \chi_R^{(3)}$ Eq. 9 can be simplified in the following form:

$$I_{CARS}(\omega_{aS}) \propto \left| \chi_R^{(3)}(\omega_p - \omega_S) \right|^2 I_p^2(\omega_p) I_S(\omega_S) L^2 \qquad \textbf{(10)}$$

In this regime, the CARS spectrum is dominated by the resonant term and presents the expected peaked lineshapes. However, the CARS signal scales as N^2, where N is the number of vibrational oscillators in the focal volume, so that its sensitivity rapidly drops with decreasing oscillator concentration, making it difficult to quantify molecular concentrations and to detect the less abundant bonds such as those that occur in the fingerprint region. If, on the other hand, $\chi_{NR}^{(3)} \gg \chi_R^{(3)}$ one can approximate the CARS signal as follows:

1 $$I_{CARS}(\omega_{aS}) \propto \left[\chi_{NR}^{(3)2} + 2\chi_{NR}^{(3)}Re\left[\chi_R^{(3)}(\omega_p - \omega_S)\right]\right]I_p^2(\omega_p)I_S(\omega_S)L^2 \qquad \textbf{(11)}$$

2 In this case, despite the presence of a large background and of a severe lineshape distortion, the CARS signal
3 scales linearly with N, making this regime more favorable for the detection of the weak signals in the fingerprint
4 region. In this regime the NRB can act as a local oscillator (LO), intrinsically phase coherent with the resonant
5 vibrational signal of interest and allowing its amplification through the product of $\chi_R^{(3)}$ by $\chi_{NR}^{(3)}$. In this regime,
6 however, in order to distinguish the resonant signal from the NRB, it is necessary to detect the complete CARS
7 spectrum (see **Section 2.2.3**) and not just the response at a single frequency.

8 For the case of SRS, one can write (considering SRG detection) $\omega_1 = \omega_2 = \omega_p$, $\omega_3 = \omega_S$, so that $\omega_4 = \omega_S$ and the
9 phase matching condition $\Delta k = 0$ is automatically satisfied. The nonlinear signal then becomes:

10 $$\Delta E_S(\omega_S) = -i\frac{3\omega_S}{4cn_S}\chi^{(3)}(\omega_p - \omega_S)|E_p(\omega_p)|^2 E_S(\omega_S)\mathsf{L} \qquad \textbf{(12)}$$

11 and is emitted at the same frequency and with the same propagation direction as the Stokes field, so that the
12 detector measures the overall Stokes intensity:

13 $$I_S(\omega_S) = |E_S(\omega_S) + \Delta E_S(\omega_S)|^2 \cong |E_S(\omega_S)|^2 + 2E_S(\omega_S)Re[\Delta E_S(\omega_S)] \qquad \textbf{(13)}$$

14 where we have assumed $\Delta E_S \ll E_S$. In this way, the nonlinear signal ΔE_S is superimposed to the Stokes field E_S,
15 which allows its amplification (self-heterodyne detection).

16 The SRG signal, i.e. the differential Stokes intensity in the presence and absence of pump, thus becomes:

17 $$SRG = \Delta I_S(\omega_S) = 2E_S(\omega_S)Re[\Delta E_S(\omega_S)] \propto Im\left[\chi_R^{(3)}(\omega_p - \omega_S)\right]I_p I_S L \qquad \textbf{(14)}$$

18 The SRS signal is thus proportional to the imaginary part of the third-order susceptibility tensor $\chi^{(3)}$. Since the
19 NRB is a real quantity, SRS is inherently free from NRB. Furthermore, thanks to the heterodyne amplification, SRS
20 scales linearly with *N*, thus allowing the detection of low-concentration species and signals in the fingerprint
21 region. On the other hand, SRS requires the detection of a weak differential SRG(SRL) signal sitting on the large
22 linear background given by the Stokes(pump) light. Extraction of this signal (which can be as small as 10^{-4}-10^{-5})
23 calls for the use of sophisticated techniques, involving high-speed modulation and lock-in detection, to overcome
24 the laser fluctuations and achieve shot-noise limited detection. Such techniques are challenging to be
25 implemented at high speeds, with integration times of few tens of microseconds, and over a broad spectrum,
26 required to extract the entire Raman fingerprint of the molecules. It is worth noting that, since $Im[\chi^{(3)}]$ is
27 proportional to σ_{SR}, SRS spectra faithfully replicate SR spectra, allowing the Raman database to be used to
28 interpret SRS measurements.
29 Taken together, CARS and SRS each present advantages and drawbacks, which make one or the other technique
30 preferable according to the configuration and the sample to be studied. In the following sub-sections, we will
31 discuss experimental implementations of CARS and SRS relevant to histopathology, both in the narrowband and
32 in the broadband configurations.
33

34 **2.2.2 Narrowband CARS/SRS microscopy**

Narrowband (single-frequency) CARS/SRS is the simplest and most widely employed CRS configuration, and for this reason its experimental layout is rather well established. **Figure 6** reports the typical experimental setup of a narrowband CARS/SRS microscope. The two imaging modalities share many common elements, such as the laser source and the microscope architecture, and differ essentially in the detection chain. Narrowband pump and Stokes pulses, generated by a suitable laser source, are synchronized by an optical delay line, collinearly combined by a dichroic mirror and sent to a scanning unit, consisting of two galvanometric mirrors, and to a first microscope objective, which focuses them on the sample. So-called scan and tube lenses are in general placed between the galvanometric mirrors and the objective in order to conjugate the mirrors with the back aperture of the objective in a standard 4-f configuration. In the transmission configuration, the light transmitted by the sample is collected by a second microscope objective. In the case of CARS, the anti-Stokes light is spectrally selected by a sequence of short-pass filters and detected by a photomultiplier. In the case of SRS, a high-frequency modulator (either electro- or acousto-optic) is inserted in the pump (Stokes) beam path and the transmitted Stokes(pump) beam, spectrally selected by a series of long-pass(short-pass) filters, is sent to a photodiode followed by a lock-in amplifier (LIA), which synchronously demodulates it and measures the SRG (SRL) signal. Typically, modulation frequencies of the order of 1-40 MHz are used in SRS, which allow working in a region of low relative intensity noise of the laser source, approaching shot-noise-limited detection. For CARS, also the so-called "epi" configuration can be used (not shown in **Fig. 6**), in which the back-scattered light is collected by the focusing objective and then sent to the detection chain via a dichroic beam splitter. While epi CARS is commonly used for thick tissues[43] epi SRS, although possible, is more challenging to implement [44]. Single-frequency CARS/SRS microscopy require the same laser source, capable of generating synchronized narrowband pump/Stokes pulses, with the following specifications: i) 3-5 ps transform-limited pulse duration, corresponding to <10 cm^{-1} bandwidth, in order to guarantee the required spectral resolution and at the same a maximized peak power to enhance the nonlinear optical effects; ii) high repetition rate of the order of 40-80 MHz, to enable high-speed imaging; iii) at least 100 mW average output power per beam, to allow illuminating the sample with 10-20 mW power level after considering the various optical losses, which is a typical threshold before reaching optical damage in tissues/cells; iv) emission in the near-infrared range (700-1200 nm) to combine high transmission within cells and tissues with reduced multi-photon absorption cross sections; v) fast and automatic tunability of at least one of the pulses, in order to access different vibrational frequencies of interest. Such characteristics are not easy to obtain and a number of laser systems for CRS microscopy have been proposed. Initial configurations relied on electronically synchronized picosecond Ti:sapphire lasers [45] which, due to their complexity, have been rapidly superseded by optical parametric oscillators pumped by picosecond mode-locked neodymium optical parametric oscillators (OPOs), which are the current gold standard for CRS microscopy [46]. These configurations are however bulky, complex and expensive and not suitable for deployment outside research laboratories and in a clinical environment. For this reason, several architectures of fiber-format lasers sources have been proposed. Fiber lasers are compact, alignment free and potentially low cost. One architecture relies on a femtosecond Er:fiber oscillator followed by two Er:doped fiber amplifier branches, from which narrowband tunable pump and Stokes pulses are generated by nonlinear frequency conversion [47,48]. Another approach relies on the combination of a picosecond Yb:fiber oscillator with a fiber-based OPO exploiting third-order nonlinearities [49].

Overall, narrowband CRS microscopy is a rather mature technology and has reached very high acquisition speed, with pixel dwell times below 1 µs for both CARS and SRS implementations [50,51], allowing video rate acquisition

1 of images. However, for many applications the amount of delivered information is not sufficient and broadband
2 approaches, described in the following paragraphs, are required.
3
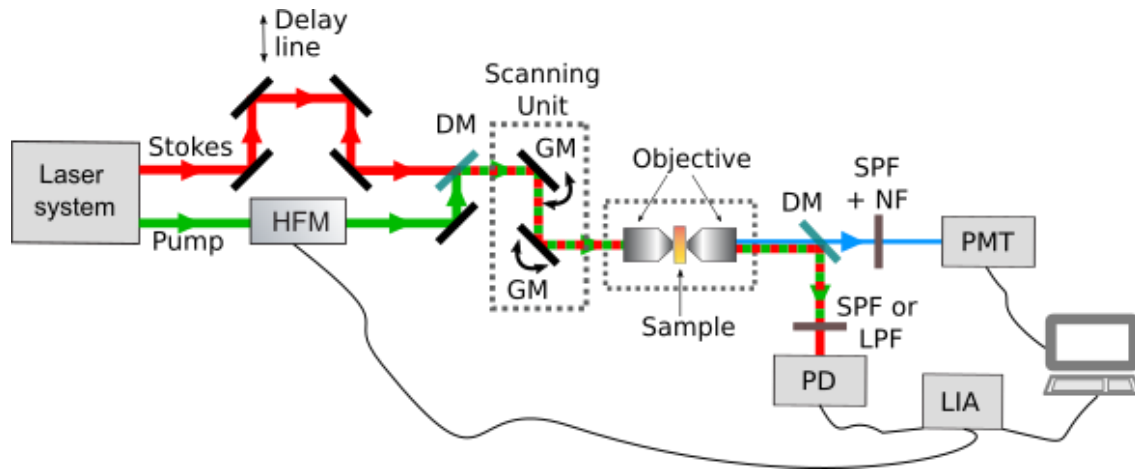
6 **Fig. 6** CARS/SRS microscope setup. HFM, high-frequency modulator; DM, dichroic mirror; GM, galvanometric mirror; LPF,
7 long-pass filter; SPF, short-pass filter; NF, notch filter; PD, photodiode; PMT, photomultiplier tube; LIA, lock-in amplifier.
8 Adapted with permission from [52].
9

10 **2.2.3 Broadband CARS microscopy**

11 Broadband CARS approaches can be generally classified as hyperspectral or multiplex. In hyperspectral CARS, the
12 signal at a single Raman frequency is recorded at a given time and the pump-Stokes detuning is swept to record
13 the CARS spectrum sequentially. In multiplex CARS the Stokes pulse is broadband, and the CARS spectrum is
14 measured in parallel using a multichannel detector.

15 One approach to hyperspectral CARS uses the single-frequency CARS apparatus discussed above, employing two
16 narrowband ($\leq$10 cm^{-1}) picosecond pulses, and rapidly tunes the wavelength of one of the pulses to scan the
17 Raman frequency. In another approach, known as spectral focusing (see **Fig. 7**), both pump and Stokes pulses
18 are broadband, with spectra covering several hundreds of wavenumbers and transform-limited durations of <
19 100 fs. Before the nonlinear interaction, pump and Stokes pulses are chirped with the same frequency vs. time
20 dependence up to picosecond duration, so that their instantaneous frequency difference (IFD) is kept constant
21 and matches a single vibrational frequency (indicated as Ω_1 in **Fig. 7**). By finely adjusting the relative arrival time
22 of the pulses (indicated as Δt in **Fig. 7**), it is then possible to tune the IFD and thus the Raman detuning (see the
23 new frequency Ω_2 in **Fig. 7**) without the need for tuning the pulse spectrum. Note that the maximum tuning range
24 for the Raman frequency is limited by the pulse bandwidth.

25

26
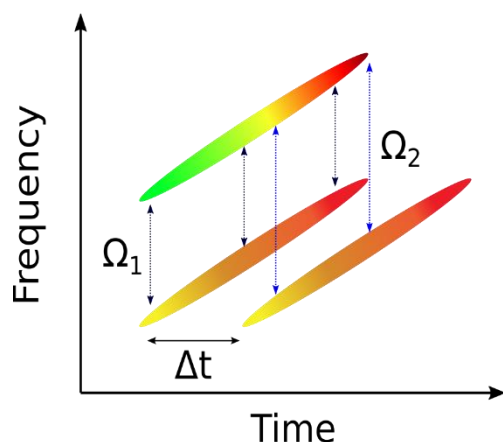
Fig. 7 Concept of spectral-focusing CARS/SRS, showing the time-dependent frequencies of pump and Stokes pulses and the frequency tuning performed by varying the relative arrival time Δt.

Special care must be taken to impart the same chirp onto the two laser pulses [53], to avoid spoiling the spectral resolution. This can be a difficult task: as the two pulses are tuned to different wavelengths, the same optical system employed to chirp the pulses (typically a double-pass grating or prism pair, a prism/lens or grating/lens combination or a long block of highly dispersing glass) could result in different second-order or third-order dispersion contributions. To this aim, a rather complex and expensive but also very powerful solution is the use of a pulse shaper, in which a spatial light modulator is placed in the Fourier plane of a grating [53,54]. Several approaches have been proposed to rapidly scan the pump-Stokes delay and thus vary the IFD, including galvanometric mirrors and acousto-optic programmable dispersive filters; these methods are described more in detail in the following paragraph dealing with broadband SRS.

In multiplex CARS [55–60], on the other hand, only the Stokes pulse is broadband, while the pump pulse is kept narrowband (≤10 cm^{-1}, corresponding to ≥1 ps duration). In this configuration, schematized in Fig. **Fig. 8**, a band-pass filter (BPF) selects a narrow (≈10 cm^{-1} bandwidth) spectral component of the output of a femtosecond Ti:Sapphire laser oscillator, serving as the pump for the CARS process. The remainder of the laser output is then sent to a nonlinear fiber (NLF, either a tapered or a photonic crystal one) for spectral broadening. A long-wave-pass filter (LPF) selects the red-shifted portion of the spectrum, to be used as broadband Stokes pulses for the CARS process. A delay line synchronized the two pulses, and a dichroic mirror (DM) combines them in a collinear geometry before entering the microscope stage. After the sample, the generated anti-Stokes beam is then selected using a short-wave-pass filter (SPF) and its spectrum detected using a spectrograph equipped with a multi-channel detector (typically a CCD camera). In this way, the entire CARS spectrum is recorded in parallel over both the fingerprint and the C-H stretching region.
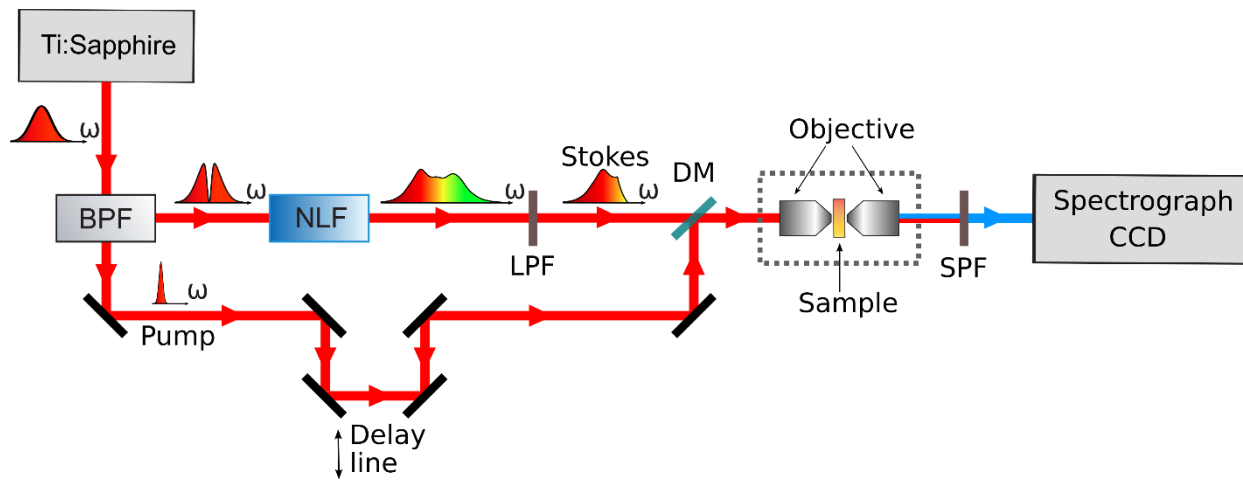
1
2
Fig. 8: Broadband CARS: Schematic setup of a Ti:sapphire-based broadband CARS microscope. BPF, reflective bandpass filter; NLF, nonlinear fiber; LPF, long-pass filter (wavelength); DM, dichroic mirror; SPF, short-pass filter (wavelength).

To enhance the weak signal generated in the fingerprint region due to the low cross section of the Raman signal, Cicerone *et al*. [61,62] employed ultrashort (16-fs) pulses on the sample to take advantage of the interplay of the so-called "2-colour" and "3-colour" CARS schemes, as illustrated in **Fig. 9**. The "2-colour scheme" corresponds to two interactions with the narrowband pump pulse and one interaction with the broadband Stokes pulse. The achievable Raman frequencies correspond to the differences between the narrowband pump frequency and the frequencies contained in the broadband Stokes pulse spectrum.

18
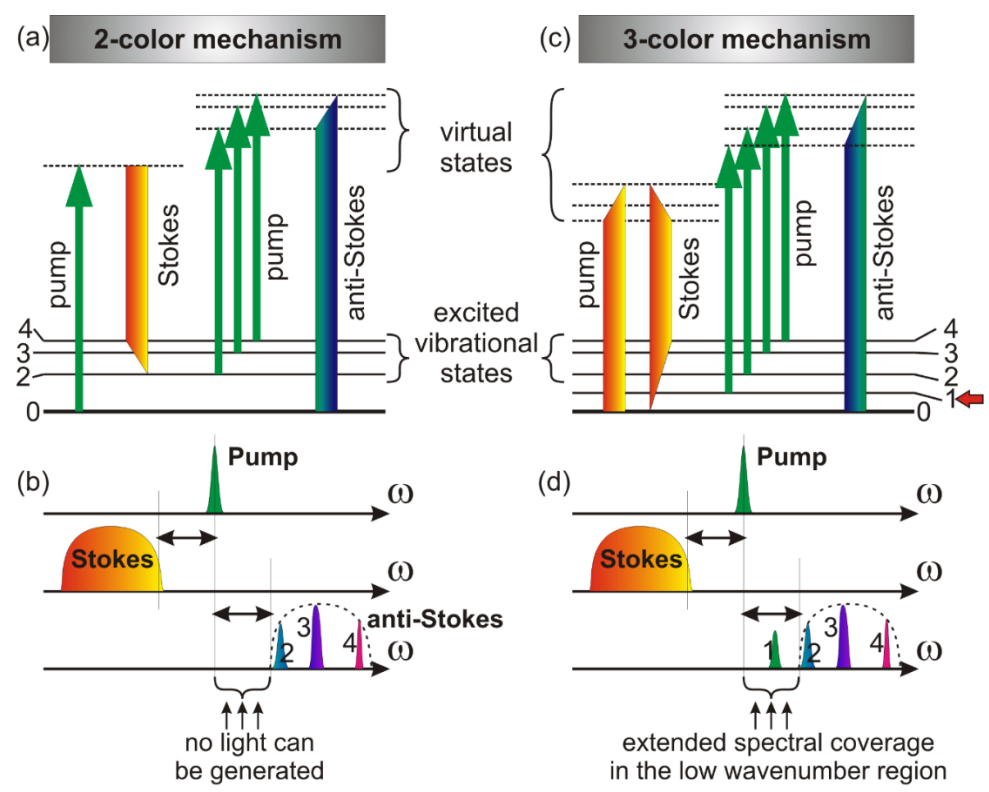
Fig. 9 (**a-b**) 2-colour and (**c-d**) 3-colour generation mechanisms. Note that only the 3-colour mechanism can access the low-frequency vibrational mode numbered "1" (red arrow).

In the "three-color" (also called "intra-pulse") approach (see **Fig. 9** (c-d)), two interactions with the broadband pulse impulsively promote molecules to vibrationally excited states, by the so-called impulsive stimulated Raman scattering mechanism [63]. The excitation profile is thus determined by the permutations of all available pump frequencies: for adjacent frequencies, the possible permutations are higher in number, so that the three-color mechanism is more effective for lower vibrational frequencies. This makes it perfectly suited for stimulating Raman transitions within the vibrational fingerprint region. This is also illustrated in **Fig. 9** : the vibrational mode number "1" is efficiently excited (panel (c)) and appears in the CARS signal (panel (d)).

In both hyperspectral and multiplex CARS approaches, the resonant vibrational signal is mixed with the NRB, which distorts the lineshapes with respect to those measured in SR. This problem is particularly severe in the fingerprint region, where the resonant Raman features are weaker than in the C-H stretching region. For hyperspectral CARS based on spectral focusing, the NRB can be removed using a frequency-modulation approach [64]. In this implementation, a double pass into a Pockels cell, modulated at high frequency, generates two pump pulses with different arrival times on the sample, thus effectively modulating the pump-Stokes IFD in and out of the vibrational resonance. A LIA demodulates the signal and extracts SR-like spectra with largely reduced NRB contributions. On the other hand, NRB can be beneficial in multiplex CARS, acting as an inherently phase-locked local oscillator (LO) for heterodyne amplification of the nonlinear CARS signal (see **Eqs. 9 and 11**] to retrieve the absorptive imaginary part of the nonlinear susceptibility. At the same time, the measurement of the entire CARS spectrum unlocks the possibility to use analytical techniques, such as the Maximum Entropy Method [65] and the time-domain Kramers–Kronig transform [62,66] or artificial-intelligence-based methods [67,68], to retrieve the absorptive imaginary part of the nonlinear susceptibility.

Other approaches to broadband CARS, different from the aforementioned hyperspectral and multiplex ones, have been demonstrated, such as time-resolved CARS and Fourier-Transform (FT) CARS, but they have not yet been extensively employed for biological tissue analysis and tumor identification. Briefly, time-resolved CARS [69–71] generates a vibrational coherence in the sample by exciting the Raman modes with two interactions with the pump and Stokes fields, which could be either taken from two independent pulses or from the same broadband pulse with ultrashort (≈10-20 fs) duration, via the aforementioned ISRS mechanism. Such coherence lasts for a few picoseconds, as determined by the vibrational dephasing time T_{2v} of the molecules. A delayed probe pulse reads out such coherence, thus generating the anti-Stokes signal. The advantage of this technique is the removal of the NRB, which is a purely electronic process requiring temporal overlap between the pump/Stokes and the probe pulses. The drawback is the rather weak extracted signal, as the vibrational coherence decays in time as $exp(-2t/T_{2v})$, where t is the delay of the probe with respect to the pump/Stokes pulses. FT-CARS [72–74], on the other hand, is a time-domain technique employing two ultrashort (≈10-20 fs duration) pulses with variable relative delay on the sample. The first (pump) pulse excites, via ISRS, those molecular vibrations in the focal spot whose oscillation period is (at least slightly) longer than the pulse duration, thus making the technique suitable mainly for the fingerprint Raman spectral region and not for the high-frequency Raman modes in the CH-stretching region. The second (probe) pulse is then modulated by the time-dependent refractive index generated by the ISRS process. Fourier transform of this temporal trace provides the

spectrum of the excited Raman modes. As NRB is a purely electronic process, not involving any interaction with the sample vibrational levels, FT-CARS has the advantage of removing it by excluding the signals around zero-time delay. However, it also has the drawback of requiring short pulses at the sample, which are difficult to handle and can induce damage to cells and tissues.

2.2.4 Broadband SRS microscopy

Broadband SRS microscopy is an emerging technology that is undergoing a rapid development. As for broadband CARS, it can be classified in two main categories: hyperspectral and multiplex. In hyperspectral SRS microscopy the frequency detuning between pump and Stokes beams is sequentially scanned, resulting in a single Raman vibrational frequency measured at a time. The large tunability of OPOs [75,76] is particularly suited to the purpose, as well as their favourable noise properties that allow the speed of single-frequency SRS imaging to be pushed up to the video rate [44]. On the other hand, the relatively low tuning speed of OPOs results in a time-consuming approach when broad bands have to be scanned. In this area, excellent results were obtained by Schweikhard and colleagues using a Leica SP8 CARS laser scanning microscope with SRS option (Leica Microsystems, Mannheim, Germany) [77]. This has been the first fully integrated SRS commercial microscope. A PicoEmerald S OPO (APE, Berlin, Germany) provides both the pump beam fixed at 1030 nm and a Stokes beam tunable from 720 to 980 nm. This system allows exciting vibrational frequencies in the spectral range from 4200 to 500 cm^{-1} with a spectral resolution of ~12 cm^{-1}. An electro-optic modulator(EOM) modulates the Stokes beam and the SRS signal is acquired in the forward direction through a single photodiode and a LIA.

The state of the art of hyperspectral SRS microscopy in terms of imaging speed was achieved by Ozeki et al. [78]. The experimental setup, presented in **Fig. 10**, employs a narrowband picosecond Ti:sapphire laser at 76 MHz repetition rate as a pump and an electronically synchronized broadly tunable Yb:fiber oscillator with a factor of two lower repetition rate (38 MHz) as a Stokes. This enables lock-in detection of the SRL signal at the maximum frequency with no need for external modulation [79]. High-speed tuning of the Stokes pulse is achieved by a high-resolution tunable bandpass filter, which selects a single wavelength within the 30-nm bandwidth of the Yb:fiber laser by angle tuning of a galvanometric mirror with a millisecond response time [80]. This setup allowed acquiring up to 90 spectral images consisting of 480 x 500 pixels in 3 seconds, over a wavenumber range of 300 cm^{-1} with a spectral resolution of ~3 cm^{-1}. In another implementation, Kong et al. [81] performed hyperspectral SRS imaging using a custom-made electronically controlled Lyot filter to quickly command an OPO and tune the output wavelength in a line-by-line mode.
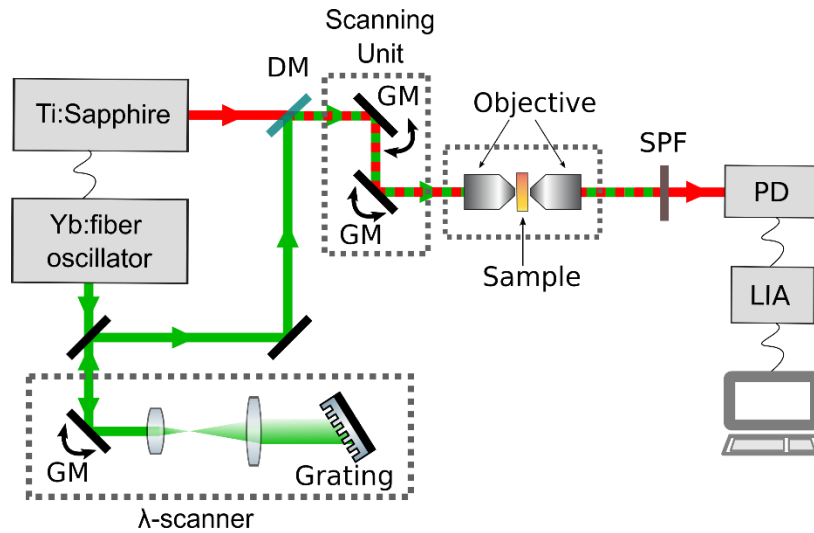
Fig. 10 Scheme of a fast hyperspectral SRS microscope used by Ozeki and colleagues. DM, dichroic mirror; GM, galvanometric mirror; SPF, short-pass filter (wavelength); PD, photodiode; LIA, lock-in amplifier. Adapted from [78].

A different approach to hyperspectral SRS microscopy is based on the previously described spectral focusing concept [75,76], which exploits broadband frequency-chirped pump/Stokes pulses whose time delay is varied to sweep their IFD (see **Fig. 7**). In earlier implementations the detuning was obtained by a motorized translation stage in a frame-by-frame approach that resulted to be detrimental for the overall acquisition speed of the microscope [82]. Recently, taking inspiration from optical coherence tomography (OCT), significant progress in terms of tuning speed has been achieved [83]. As depicted in the sketch of **Fig. 11**, Liao et al. [84] sent the Stokes beam to the edge of a 12-kHz resonant scanning mirror. The light is then focused with a lens on a flat mirror, so that the retro-reflected light experiences a millimeter-scale optical path difference during the scan. The beam crosses twice a quarter-wave plate (QWP), so that after the resonant delay line a polarizing beam splitter (PBS) redirects the beam to the microscope setup. In this way, the authors acquired SRS spectra over a range of ~200 cm^{-1} with a pixel dwell time of 83 μs and 25-cm^{-1} spectral resolution.

Another variation of this approach was proposed by He et al. [85]. In this case, the system is based on a rapid scanning optical delay line, already used in OCT, composed of a grating, a lens and a galvanometric mirror in a 4-f configuration. Figueroa and colleagues [86] developed a system based on parabolic fiber amplifier that could cover more than 600 cm^{-1} spectral bandwidth at a resolution of ~10 cm^{-1}. Fu and co-workers [87] added frequency modulation to a hyperspectral SRS microscope and, in this way, they effectively removed imaging backgrounds. With this setup, they successfully imaged a non-labelled neurotransmitter directly in live tissue.
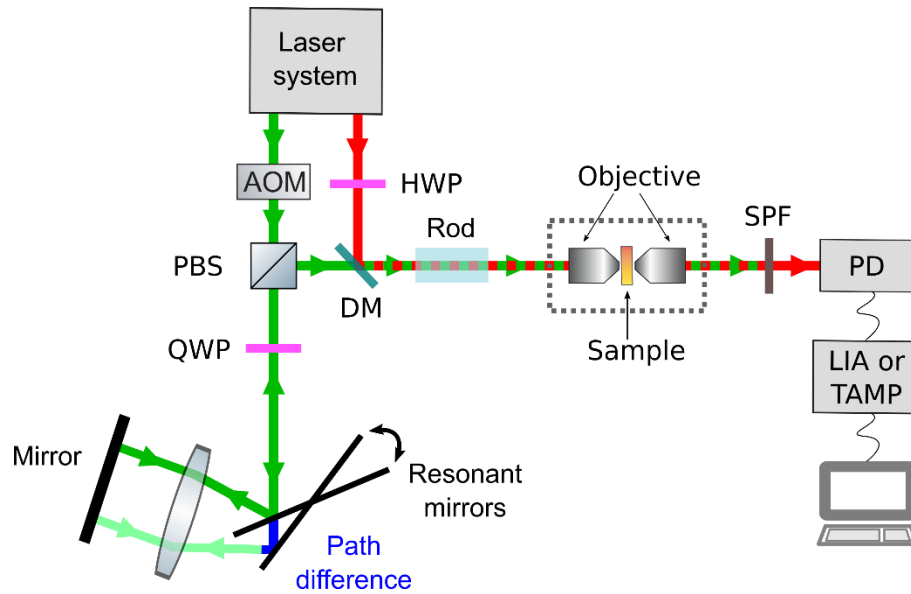
Fig. 11 Sketch of the setup for hyperspectral SRS imaging based on spectral focusing, employing a microsecond delay-line tuning. AOM, acousto-optic modulator; HWP, half-wave plate; PBS; polarizing beam splitter; QWP, quarter-wave plate; DM, dichroic mirror; SPF, short-pass filter (wavelength); PD, photodiode; LIA, lock-in amplifier; TAMP, tuned amplifier. Adapted from [84].

Another approach to achieve fast delay tuning uses acousto-optic programmable dispersive filters (AOPDFs) [88,89]. This solution is particularly interesting because it does not employ any mechanical element. The working principle of the AODPF relies on the interaction, under phase-matched conditions, between an ultrashort laser pulse and an acoustic wave, both collinearly propagating inside a birefringent crystal. AOPDFs allow sweeping a range of delays of a few picoseconds at kHz repetition rate. Alshaykh and colleagues [90] developed a hyperspectral SRS microscope using an AOPDF and succeeded in acquiring 400 x 400 pixels hyperspectral images in 5.3 s. Recently, Audier et al. [91] created a fast and low-noise SRS imaging platform combining spectral focusing and optimized AOPDFs. They reported hyperspectral SRS imaging over a 200 cm^{-1} spectral range with 12 μs of pixel dwell time and demonstrated the possibility to perform label-free histology on human tissues.

The acousto-optic tunable filter (AOTF) is another device exploited in recent SRS apparatuses that allows obtaining fast wavelength tunability without any mechanical movement. In an AOTF, an acoustic wave propagating in a birefringent crystal induces diffraction of an optical wave propagating in the same crystal. By control of the frequency and the amplitude of the acoustic wave, one can regulate the wavelength and the intensity of the diffracted one. This technology can be used for both hyperspectral and multiplex SRS microscopies. In the first case, the hyperspectral image is acquired tuning a single wavelength at a time and sequentially sweeping the spectral range of interest. In the second case, the image is acquired using multiple excitation wavelengths at the same time, which are distinguished by applying radio frequency (RF) signals at different frequencies to the modulator. Fu et al. [92] performed multiplex SRS microscopy employing an AOTF driven by 8 RF channels with 33 cm^{-1} spectral resolution. The two laser sources utilized were a femtosecond Ti:sapphire laser for the pump beam and a picosecond Yb laser for the Stokes beam. They decided to use just three channels of the AOTF, modulated at 125, 100, and 75 kHz, to avoid crosstalk between them. Each channel was set to excite a different vibrational frequency of the sample under investigation. Then, they applied a 20-

MHz modulation to the Stokes beam through an EOM and the detection was performed collecting pixel-by-pixel the whole SRS signal on a photodiode. At this point, by demodulating with a LIA at 20 MHz and then performing a real-time digital FT, the three SRS signal components were recovered and multiplex SRS imaging was demonstrated. More recently, C. Liberale and co-workers [93] demonstrated a broadly tunable SRS microscope based on a narrowband and fast scanning AOTF filter covering the entire 800-3600 cm^{-1} Raman spectrum with an enhanced 8 cm^{-1} spectral resolution.

Similar to CARS, the multiplex approach allows acquiring the full SRS spectrum in a single shot. Technically, it requires a modulated narrowband pump and a broadband Stokes beam which are temporally and spatially overlapped and sent to a microscope. A multichannel detector, either digital or analog, records the broadband Stokes signal from which, after analog or digital demodulation, the SRG spectrum is extracted. For the case of SRS, also the combination of a broadband pump with a narrowband Stokes and detection of SRL can be employed. Digital demodulation employs a spectrometer based on a CCD detector, while analog demodulation employs an array of photodiodes coupled to a multi-channel LIA. Several multiplex SRS setups have been proposed that make use of digital demodulation [94–96] but, since no extensive biological applications have been reported for any of them, they will not be described here. **Fig. 12** shows a general scheme of multiplex SRS setup based on analog multi-channel lock-in amplifier. A beam splitter (BS) separated the two beams: the broadband pump is generated using a broadband OPO, while the narrowband ($\approx$10 cm^{-1}) Stokes is retrieved by simply spectral narrowing (SN) the laser source using an transmission etalon or an ultra-narrowband interference filter or a spectral filter in the Fourier plane of a 4-f grating or prism system. A acoustic-optical or electro-optical modulator modulates the narrowband Stokes at high frequency. A delay line synchronizes the two pulses that are then combined using a dichroic mirror (DM) and sent to the microscope setup. After the sample, a short-pass filter selects the modulated broadband pump, which is then dispersed using a grating. Its spectrum is then imaged on a photodiode detector array, couple to a multi-channel lock-in amplifier (M-LIA) [97,98] for analog demodulation.
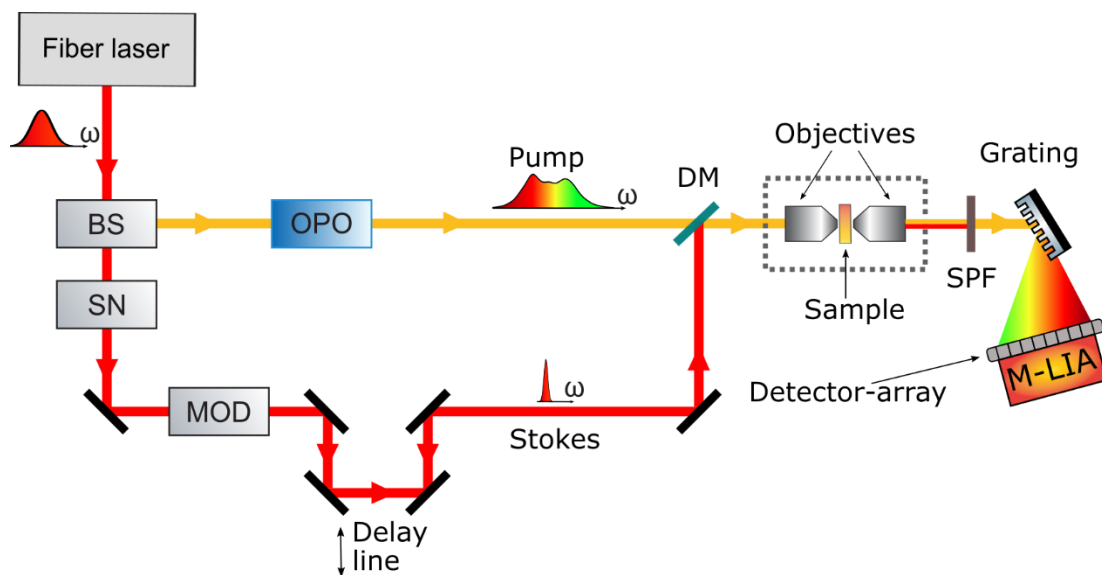
Fig. 12 Multiplex SRS setup. PBS, polarizer beam splitter, SN, spectral narrowing, MOD, modulator; DM, dichroic mirror; LPF, long-pass filter; M-LIA, multi-channel lock-in amplifier.

A first multi-colour SRS setup was reported by Lu and co-workers [99]. From a broadband femtosecond laser, used as a pump beam, three narrowband peaks are selected employing a grating-based pulse shaper. Each selected peak corresponds to a particular vibrational frequency. On the detection side, the pump pulse transmitted through the sample is again sent to a grating, in order to disperse the three narrowband peaks and to collect each of them on an independent photodiode coupled to a LIA and measure the corresponding SRL signal.

Liao et al. [100,101] replaced the LIAs in the detection system with an array of 16 tuned amplifiers (TAMPs), which have a simplified circuitry with respect to commercial LIAs. A TAMP is composed of an LC circuit, a preamplifier, an amplifier, a band-pass filter, a rectifier and, at the end, an analog-to-digital converter (ADC) to measure the demodulated signal. This system permits fast multiplex SRS imaging over 16 channels in the C-H stretching vibrational region with 32-μs pixel dwell time and it has been used in several different biological applications [101].

1 **2.3 IR microscopy**

2 Hyperspectral IR microscopy has the goal of measuring, for every pixel of the image, the vibrational absorption
3 spectrum of a sample. The key parameters qualifying an IR hyperspectral microscope are: (a) the spatial
4 resolution, (b) the spectral resolution and (c) the acquisition time. (a) and (b) contribute to the convergence of
5 numerical methods of image analysis and thereby to reliable chemical characterization [102], while (c)
6 determines the imaging speed of the sample, such as live cells or tissue. One of the challenges of IR spectral
7 imaging is measuring spectra. While spectra in the ultraviolet, visible, or near-infrared ranges are typically
8 measured by frequency-domain spectrometers (in which light is spectrally dispersed by a prism or a grating, and
9 collected by a single scanning detector or an array of static detectors), this is not practical in the IR due to the
10 high read-out noise of the detector. For this reason, spectra in the mid-infrared (MIR) are measured with two
11 alternative approaches. The first one is by illuminating the sample with a tunable monochromatic source and
12 collecting the transmitted/reflected light at a discrete set of frequencies [103]. The second is the time-domain
13 approach known as FT spectroscopy [104]. In this technique the waveform is split in two delayed replicas, and
14 measured by a detector as a function of their delay τ. This produces an interferogram, whose FT with respect to
15 τ yields the intensity spectrum of the optical waveform.

16 Standard IR microscopes are hence composed of three building blocks, sketched in **Fig. 13:** (I) an IR light source,
17 which illuminates the sample; (II) an interferometer which generates the two delayed replicas; (III) an optical
18 imaging system equipped with an IR detector, designed to perform microscopy. In the following, we will detail
19 the properties and the state of the art of these subsystems.
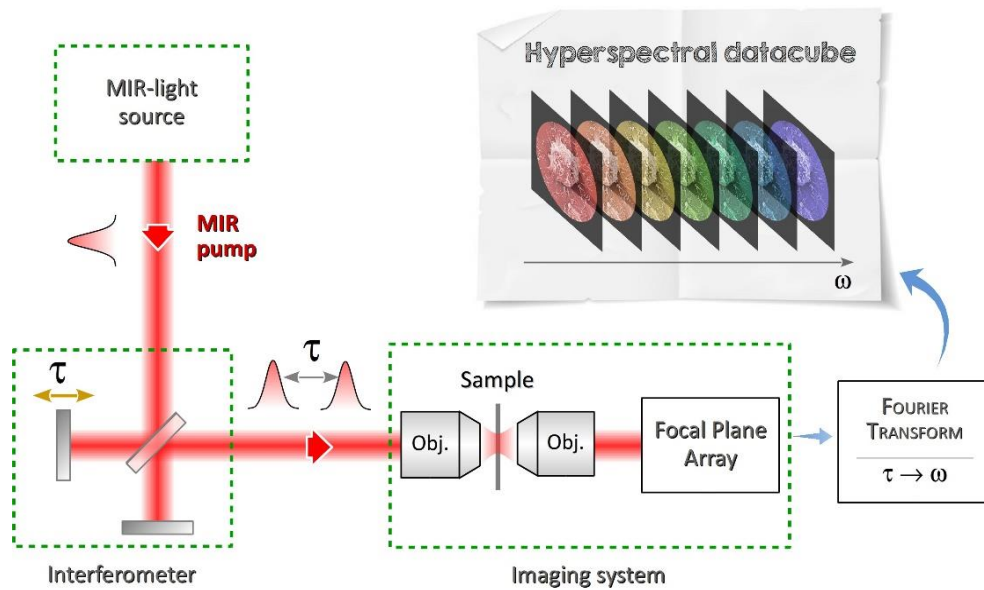
20

21 **Fig. 13** sketch of a typical hyperspectral microscope in the IR spectral range

22 (I). *The MIR illumination source*

23   The IR source illuminating the sample strongly influences the acquisition speed, the spatial resolution, and
24 the bandwidth of the hyperspectral microscope. The first two parameters strongly depend on the brightness of
25 the source, defined as the number of photons emitted per unit time, surface area, solid angle, and bandwidth;

in practice, the brightness quantifies not only the total emitted photon flux, but also its directionality. A large photon flux enables measurements with high signal-to-noise ratio, while high directionality enables sharp focusing of the light, and hence better spatial resolution of the image. In an ideal far-field system, the best achievable spatial resolution is fundamentally determined by diffraction and is thus wavelength-dependent; in addition, it strongly depends on the aperture size and the spatial coherence of the light source [105]. The best spatial resolution is obtained using infinite apertures and sources with full spatial coherence. Another relevant figure of merit of the light source is its bandwidth, which directly determines the spectral coverage of the spectrometer and consequently of the spectral imager: for IR applications, it should at least cover the whole fingerprint range.

Until recently, most IR microscopes, including many commercial products, used a spatially incoherent illumination based on a Globar. It is a thermal source, typically made of a silicon carbide rod which is electrically heated up to ≈1650°C, emitting black-body radiation from 4 to 15μm wavelength. This source is very popular because of its simplicity and broadband emission. However, black-body radiation is spatially incoherent: hence it cannot be collimated efficiently, deteriorating its brightness and -hence- the spatial resolution of any imaging application. Coherence, and consequently spatial resolution, can be increased only by decreasing the aperture size of the source; this, however, drastically reduces the number of photons reaching the sample and degrades the signal-to-noise ratio of the measurement, which can only be restored by significantly longer acquisition times. Thermal sources, essentially, force a trade-off between spatial resolution and signal-to-noise ratio. For this reason, hyperspectral IR microscopes using globars typically require long acquisition times (of the order of 5-10 minutes per image) [102,106–109] (see **Fig. 14**a).
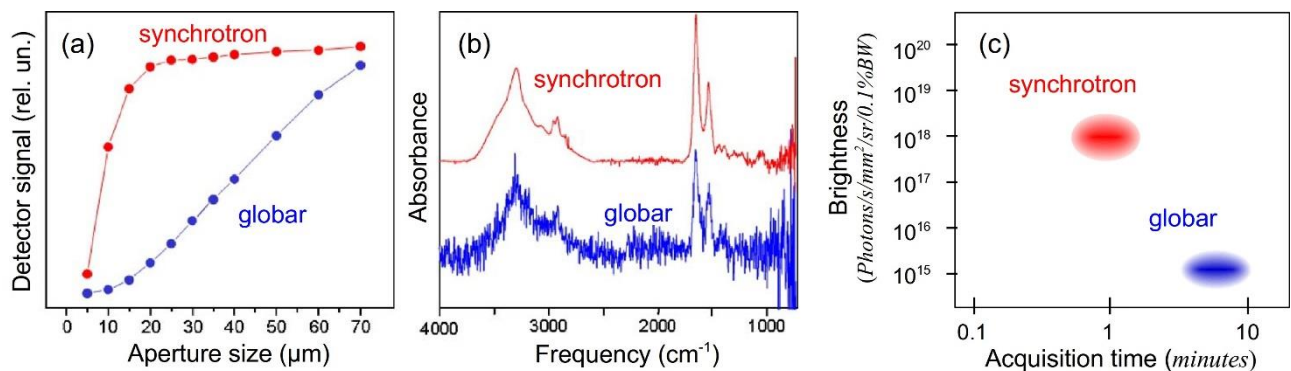
Fig. 14 Brightness of MIR sources. **a** Infrared signal through various aperture sizes comparing a synchrotron versus globar source. **b** Infrared spectra of a single red blood cell collected with a synchrotron versus globar source. The acquisition time is the same for both spectra; a square aperture of 5 × 5 μm was used. Figures are elaborated with permission from [106]. **c** Comparison of the brightnesses of different IR sources and their corresponding acquisition time of a spectral image.

The low brightness of thermal sources induced many groups to explore alternative sources for IR imaging, from synchrotron radiation [105,110,111], to lasers [112,113]. As opposed to thermal emission, synchrotron radiation is spatially coherent, which makes its brightness in the IR range about 3 orders of magnitude higher than that of thermal sources [114,115] (see **Fig. 14**c). Synchrotron radiation has been successfully applied to MIR spectroscopy and imaging [105,106,110] showing excellent performances (see **Fig. 14**b): thanks to its high

brightness, acquisition times could be dramatically reduced [116]**Errore. L'origine riferimento non è stata trovata.**. However, since imaging experiments at a synchrotron facility are obviously unpractical, various groups developed table-top spatially coherent IR sources with comparable brightness: the best candidates are laser sources.

Currently, the laser that offers in the IR range the best combination of optical power, compactness and spatial coherence is the Quantum Cascade Laser (QCL), a type of semiconductor quantum-well laser first demonstrated in 1994 [113]. It can be designed to emit narrowband light from 2.6 to 250 μm. IR spectral imaging with QCLs is currently performed by sweeping the laser emission frequency and acquiring various images as a function of the frequency. In practice, this technique samples the IR spectrum over a discrete number of frequencies [103], hence it is called multispectral rather than hyperspectral imaging. The tunability of a single QCL is however limited to <300 cm^{-1} [117] which is not sufficient to cover the broad fingerprint range (1000-1800 cm^{-1}) as required in many applications [109]. This issue is overcome by using multiple parallel QCLs, nowadays commercially available (such as MIRcat-QT™ from Daylight solutions, with tunability of 1000 cm^{-1}).

(II). *The spectrometer*

Spectra in the ultraviolet, visible, or near-infrared ranges are typically measured by frequency-domain spectrometers: light is spectrally dispersed by a prism or a grating, and each frequency is recorded by a pixel of a multichannel detector (based on silicon or InGaAs). Unfortunately, in the IR spectral range, the most suitable detectors are based on HgCdTe (Mercury Cadmium Telluride, MCT), which may provide sensitivity from 2.5 up to 16 μm (4000-600 cm^{-1}). These detectors, due to the low bandgap of MCT, introduce high read-out noise even at cryogenic temperatures, so that multichannel detectors have low performance, limited number of pixels and high cost. For this reason, spectra in the IR are measured with two alternative approaches. The first one is by illuminating the sample with a tunable monochromatic source, and collecting the transmitted/reflected light at a discrete set of frequencies [103]. The second is the time-domain approach known as FT spectroscopy [104] (see **Fig. 15**). In this technique the waveform is split in two delayed replicas (**Fig. 15**a and measured by a detector as a function of their delay τ. This produces an interferogram, whose FT with respect to τ yields the intensity spectrum of the optical waveform, as sketched in **Fig. 15**b.)
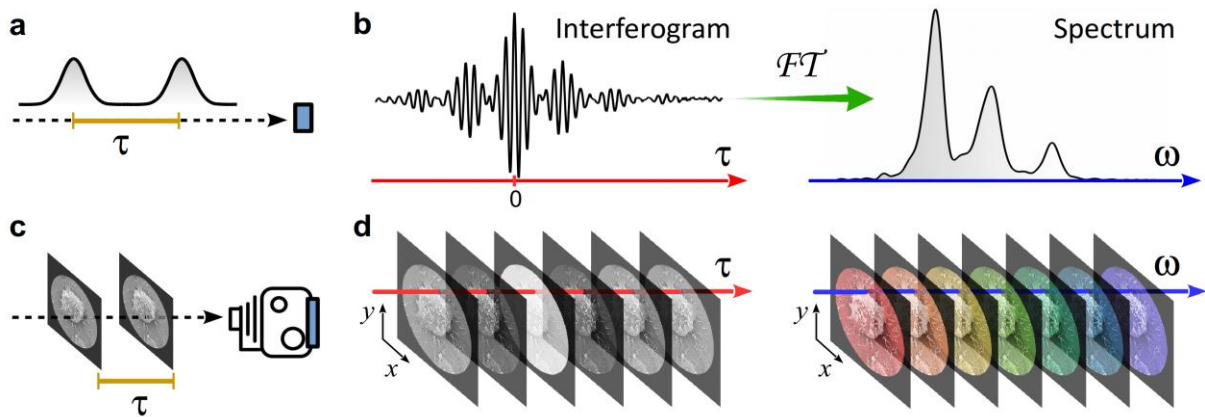
Fig. 15 Fourier transform spectrometer. **a** Two delayed waveform replicas are measured by a point detector. **b** The Fourier transform of the delay-dependent intensity (interferogram) is the intensity spectrum of the waveform. The same technique, applied to imaging: **c** Two delayed image replicas are measured by a camera. **d** The approach sketched in **b** can be repeated for any pixel of the image. The two stacks of images sketched in panel **d** are the (x,y,τ) and (x,y,ω) hypercubes, respectively.

The spectral resolution of FT spectroscopy is the inverse of the delay scan range and can thus be easily adjusted; conversely, to record an accurate interferogram, the delay must be controlled to within a small fraction (1/100 or better) of the optical cycle. With respect to frequency-domain spectrometers, the FT approach has the following advantages: a higher signal-to-noise ratio due to the simultaneous measurement of all spectral bands (the Fellgett advantage [118]) and a higher optical throughput due to lack of entrance and exit slits (the Jacquinot advantage [119]). These properties make FT spectroscopy the technique of choice in the IR range [120]**Errore. L'origine riferimento non è stata trovata.**, where the main noise source is readout noise of the detector. Virtually, all modern IR spectrometers employ the FT approach [121]; for this reason, IR spectroscopy is also commonly called FT-IR. Another important advantage of FT spectroscopy is that it is suited for wide-field imaging, since it works also for each pixel of an imaging system, as sketched in **Fig. 15**c,d. For this reason, FT spectroscopy is the acquisition method used in most IR hyperspectral imaging systems. For the measurement of linear absorption spectra, the interferometer can be placed at any point between the source and the detector. In IR hyperspectral microscopes, it is typically placed between the source and the sample.

Almost all FT-IR spectrometers, including all state-of-the-art systems reported in the literature and commercially available (Cary from Agilent, Spotlight 400 from Perkin Elmer, Hyperion series from Bruker), are based on a Michelson interferometer (see **Fig. 16**), that splits the input beam into two arms, introduces a time delay between the paths and then recombines the two fields. The main technical problem of the Michelson interferometer is that any fluctuation of the path-lengths difference translates into a jitter of the time delay, which spoils the FT accuracy. For this reason, in all commercial systems the precise control of the replicas delay for stable acquisition is guaranteed by a very robust mechanical setup and auxiliary devices, such as position tracking with a visible laser beam or active stabilization with feedback control.

Michelson Interferometer
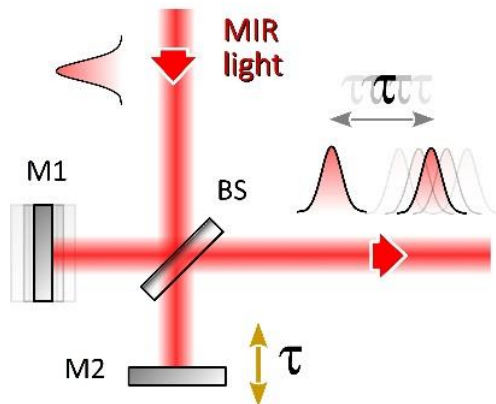
Fig. 16 general sketch of a Michelson interferometer, with the basic elements: M1, M2: end mirrors; BS: beam splitter. The delay between the field replicas is adjusted by translation of M2. The scheme also shows the effect of external perturbations. As an example, a perturbation on M1 determines a jitter of the pulse delay.

(III)- *The optical microscope*

1   The IR optical microscope scheme is similar to a visible light microscope, except that all the optics have to be
2   either reflective or transparent in the IR. In a standard optical microscope operating at wavelength λ, the spatial
3   resolution is determined by the Abbe diffraction limit and is ≈ λ/2nNA, where 0<NA<1.4 is the numerical aperture
4   of the objective and n is the refractive index of the propagation medium. In the fingerprint region (λ =5-10 μm),
5   the best spatial resolution in air is thus of the order of 2.5-5 μm. Better spatial resolution is obtained when light
6   propagates in a high refractive index substrate, as in the attenuated total reflection (ATR) modality. In this
7   technique, the sample is in contact with a high refractive index glass (e.g., diamond, germanium, or silicon); the
8   infrared beam enters the substrate at an angle of typically 45° and is totally reflected at the crystal-to-sample
9   interface. In this process a fraction of light, the evanescent wave, penetrates into the sample, at depths which
10   depend on the wavelength, the refractive indices of the ATR crystal, the sample, and the angle of the entering
11   light beam. The penetration depth is typically of the order of a few microns (ca. 0.5 - 3 μm), thus enabling to
12   measure the very surface of the sample. Thanks to the high value of n, the diffraction limit is reduced by a
13   considerable factor (up to 4 times). Despite the great improvement offered by the ATR approach, the resolution
14   is still not sufficient to resolve sub-micrometer features.

15   Microscopy images are acquired using two possible schemes: either by raster scanning the sample and
16   collecting light with a single MCT detector, or by wide field imaging, which captures the whole image at once by
17   projecting the object image on a 2D multichannel pixelated detector (Focal Plane Array, FPA) [122,123] .
18   Compared to the single-point mapping approach, the imaging approach based on FPAs dramatically reduces the
19   acquisition time from hours to minutes [124]. In the IR, each pixel unit of a FPA is a discrete MCT detector. The
20   smallest detail of the sample measured by one detector pixel defines the *pixel-size limit*, which depends on the
21   pixel size and the magnification of the microscope. FPAs became particularly attractive for IR microscopy when
22   the pixel size allowed the microscope spatial resolution to switch from "pixel-size-limited" to "diffraction-limited"
23   [125]. All the reported state-of-the-art microscopes work at the diffraction limit; the most recent improvements
24   only aimed at reducing the pixel-size limit, which currently ranges from 5.5x5.5 μm^2 to 0.63x0.63 μm^2 [107,108],
25   well below the diffraction limit. Such pixel size allows image oversampling which contributes to improving the
26   signal-to-noise ratio [107,116,126].

27   Using a combination of 4 different QCLs, each tunable over ≈300 cm^{-1}, the SPERO-QT system from Daylight
28   Solutions allows to cover the 950-1800 cm^{-1} frequency range. The FPA detector consists of an array (480×480) of
29   micro-bolometers, which do not require cryogenic cooling. Using objectives with 0.7 NA, the achieved spatial
30   resolution is ≈5 μm at a wavelength of 5.5 μm. The system was used by Kuepper and coworkers [127] for a
31   feasibility study for the rapid and label-free classification of colorectal cancer tissues. The instrument allowed to
32   obtain a spectral hypercube for a 2 × 2 mm field of view (FOV) with 2 cm^{-1} resolution in a time of the order of 1
33   minute (see **Section 3** for more details about applications in cancer detection).

34   A different QCL based system was proposed by Mittal and coworkers [128], using a single pixel confocal setup.
35   The system uses a multilaser source consisting of four QCL modules with beams combined into a single collinear
36   output covering the 770-1940 cm^{-1} frequency interval. Imaging is performed by high NA (0.85) aspheric lenses
37   and the sample is moved by high-speed linear translation stages. The transmitted beam is detected by a single,
38   large area, low-noise cryogenically cooled pre-amplified MCT photodiode. To further enhance sensitivity, the
39   QCL is modulated at high frequency (up to 100 kHz) and the MCT output is sent to a lock-in amplifier for
40   synchronous detection. The system is capable of scanning at a speed up to 300 mm/s with a high signal to noise
41   ratio. The low detector noise and the absence of speckle patterns characteristic of wide-field illumination
42   compensate for the loss of the multi-channel advantage of wide-field configurations. The microscope was applied

to a comparative study of over 100 breast tumor samples. The rich chemical information combined with the high acquisition speed allowed accurate tumour sub-typing.

The aforementioned QCL-based systems allow to improve the acquisition speed by nearly two orders of magnitude with respect to standard FT-IR microscopes and represent the current state of the art of IR microscopy. The overall speed-up of the acquisition time afforded by the QCLs is an important step towards potential clinical translation of the technique, as it allows larger scale studies in a reasonably short time.

Recently, a system overcoming the limitations imposed by the IR detectors in FT-IR microscopy has been proposed [129]. The method makes use of non-linear frequency up-conversion of the IR radiation to shift the detection to the visible spectral range, where low-cost, low-noise and sensitive detectors are available. The system starts with a picosecond Yb:fiber laser producing 15-W average power, 20-ps pulses at 1064 nm and 80 MHz repetition rate. A fraction of the laser synchronously pumps an OPO based on MgO-doped periodically poled LiNbO$_3$ (MgO:PPLN). The idler of the OPO, with a 750-900 mW average power and tunability from 2.3 to 4.1 μm, is used to illuminate the object. The transmitted beam is then sent to a 4f imaging system, in the Fourier plane of which it is combined with the residual 1064-nm beam and up-converted to the near-infrared by a lithium niobate (LN) crystal mounted on a galvoscanner, to allow angular phase matching of different MIR wavelengths. The up-converted signal is spatially back Fourier transformed by a second lens and finally detected with a standard CCD camera synchronized with the rotation of the up-converting crystal. With a 1° tilt angle of the LN crystal, the system allows to acquire in just 2.5 ms a 64 kpixel image at a single frequency with a spatial resolution of $\approx$35 μm. The system was used for a proof-of-principle label-free multi-spectral MIR imaging experiment on medical biopsies of cancerous and healthy esophageal tissue samples at 62 frequencies, achieving good agreement with standard H&E and FT-IR images and enabling unsupervised tissue clustering using the *K*-means algorithm.

1 **2.4 Photothermal Infrared microscopy**

2 In photo-thermal infrared (PT-IR) microscopy a high brightness monochromatic IR beam, typically generated by
3 a QCL laser, resonantly excites a vibrational transition of the sample. The deposited vibrational energy is rapidly
4 (tens to hundreds of picoseconds) dissipated to other vibrational degrees of freedom by intra-molecular
5 vibrational redistribution (IVR), ultimately resulting in a temperature increase of the sample, ΔT, which can be of
6 the order of a few K. Through the thermo-optical effect, the local temperature increase results in a variation of
7 the refractive index of the sample: $\Delta n \cong \frac{\partial n}{\partial T} \Delta T$, which is measured by a visible probe beam. A given molecular
8 species that has been excited in some (x,y,z) position within the sample can thus be identified in so far as the
9 probe beam senses the local index change $\Delta n(x,y,z)$ therein induced by the IR beam, also called pump beam.
10 Depending on the experimental approach, the detection of the refractive index change Δn may exploit deflection
11 or thermal lensing effects, which are related to the index gradient in the plane perpendicular to the probe
12 propagation direction, or phase-shifting effects, which are sensitive to the integrated axial index gradient, as
13 pictorially represented in **Fig. 17**.
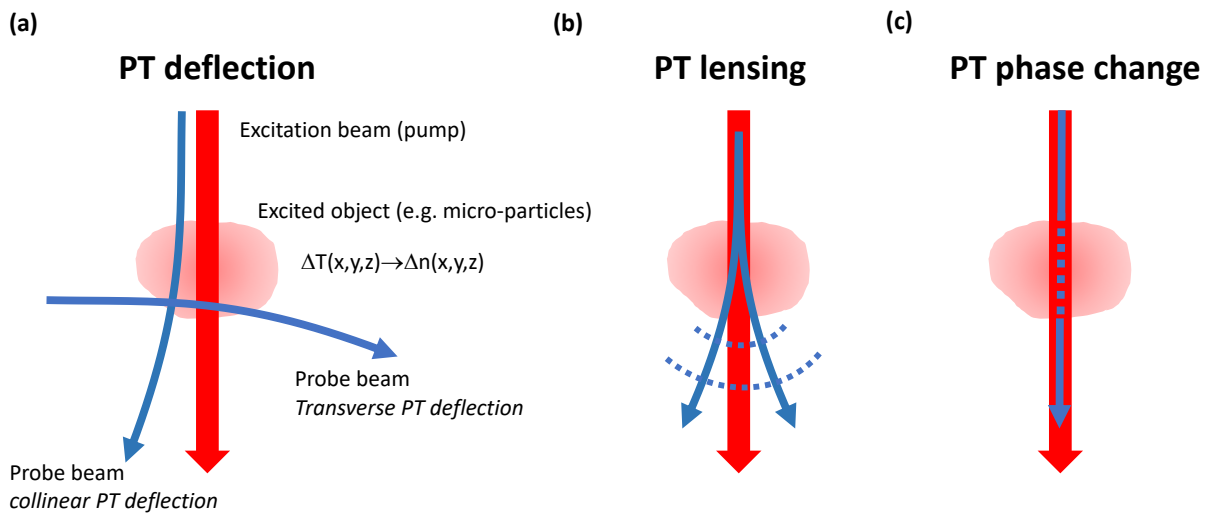
14

15 **Fig. 17** Different mechanisms can be exploited to locally probe the thermally-induced refractive index change $\Delta n(x,y,z)$ in an
16 absorbing medium: **a** the deflection of a probe beam collinearly or transversally propagating with respect to the pump; **b**
17 the phase-front distortion and the consequent change of divergence of the probe beam, i.e. a thermal lensing effect, **c** the
18 phase-shift of a probe beam that is co-propagating with the pump.

19 Until the 80s, photothermal (PT) effects were observed on gases, liquids and solids in a variety of arrangements
20 that didn't care about the spatial resolution [130,131], the smallest detected objects being 50-µm-diameter
21 micro-particles and 15-µm-diameter white blood cells [132]. A microscope objective was for the first time added
22 to a PT setup in 1993 to enhance the spatial resolution [133]. Since then, the PT technique has rapidly developed,
23 culminating with the detection of nanometer-sized metal particles in 2002 [134], much smaller than the size of
24 the illuminating spot. Differently from the majority of PT approaches adopted before, which were based on
25 deflection and thermal lensing, the tiny PT signal given by the heated nano-object was interferometrically
26 detected in a polarization-sensitive arrangement illustrated in **Fig. 18**. This achievement attested the capability
27 of PT microscopy to detect objects with diameters orders of magnitude smaller than the pump (and probe) beam
28 diameter, thus far below the diffraction limit [135]. This concept was further expanded later on by wide-field
29 nano-imaging approaches which rely on the quantitative detection of photo-thermally induced phase-shifts via
30 digital holography [136]. In this approach pump and probe beams illuminate a large portion of the sample and

1   the two-dimensional phase-shift pattern imprinted by the sample onto the probe beam is digitally recorded on
2   a camera sensor by making the probe beam to interfere with an unperturbed reference beam derived from the
3   same laser source. This mimics holography, the only difference being that the camera must be operated in a sort
4   of lock-in modality, with "pump-on" phase patterns (hot frames) subtracted to "pump-off" phase patterns (cold
5   frames), in order to extract the pump-induced differential phase.
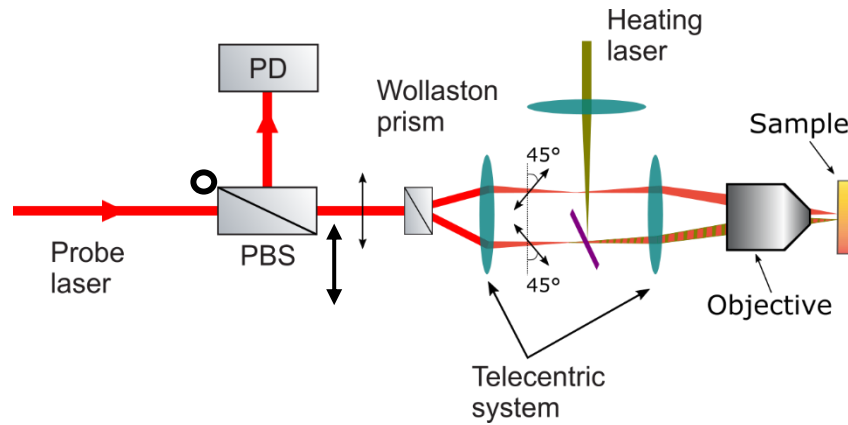
6

7   **Fig. 18** PT setup used for single-point detection of nano-objects.A Wollaston prism splits a horizontally polarized probe laser
8   (red) into two beams that are focused in different nearby spots by a microscope objective. The heating produced by a pump
9   laser (green) at just one spot location introduces a differential phase-shift between the two probe beams. This shift is
10   interferometrically detected by recombining the back-reflected probe lasers to a common vertical polarization state by the
11   help of a polarizing beam-splitter (PBS) before being sent to a photo-detector (PD). Adapted from [134].

12

13   Photo-thermally tracked metallic nanoparticles aroused interest in biology as a viable alternative to bulky labels
14   consisting of fluorescent antibodies, thanks to the absence of photo-bleaching, the chemically inert behavior and
15   the minimal perturbation to the sample given their much smaller size [137]. The use of functionalized plasmonic
16   nanostructures as a sensing platform enabled in 2012 the PT detection of single proteins, through the plasmon
17   resonance shift (and the resulting local temperature change) that occurs when the target molecule binds to the
18   probed nano-antenna [138]. In other experimental settings no PT medium was exploited, for example to visualize
19   mitochondria [139] and lysosomes [140] in living cells, or to image H&E-stained biological tissues [141]. In these
20   cases, the excitation was obtained through electronic transitions in the visible, which give rise to local
21   temperature changes of several degrees and thus to large PT signals. On the other hand, absorption in the visible
22   offers relatively poor chemical selectivity, due to the large overlap between absorption bands from different
23   molecular species in that region. PT-IR microscopy was introduced in 2009 [142]in view of removing this
24   bottleneck: in PT-IR microscopy an IR pump at a proper wavelength selectively excites a vibrational transition of
25   a given molecular species, while a visible beam probes the pump-induced local index change with high spatial
26   resolution. Vibrational excitation of the target molecule in the IR ensures chemically-selective label-free imaging,
27   similarly to FT-IR, SR and CRS imaging.

28   As compared to FT-IR, PT-IR microscopy exhibits several advantages: i) the spatial resolution is almost one order
29   of magnitude higher - ~0.5 μm against 5 μm – because of the much more favorable diffraction limit in the visible,
30   enabling intra-cellular imaging; ii) the tight focusing of the visible beam results in 3-D sectioning capabilities that
31   are out of reach in a purely mid-infrared imaging system; iii) PT-IR microscopy exhibits a flatter baseline,
32   particularly with inhomogeneous samples, since the signal is read out against a zero background and not against
33   a residual amount of transmitted light; iv) the penetration depth in living samples subjected to water absorption

is much larger than in FT-IR microscopy (100 μm rather than 10 μm scale), on the one hand because the large thermal capacity of water mitigates parasitic PT water signals, on the other hand because in a background-free approach a strong PT signal may emerge even at large depths where the IR beam is almost extinguished. As compared to SR, PT-IR microscopy offers a superior imaging speed due to the much larger cross-sections in absorption than in Raman scattering, which result in a stronger signal. As compared to a CRS approach, which produces relatively weak signals in the low-wavenumber region, PT-IR microscopy holds a higher potential for molecular fingerprinting thanks to the capability of direct excitation in the 700-1700 cm^{-1} range.

PT-IR microscopy has been mostly implemented so far with optical setups similar to those shown in **Fig. 19** with the sample raster scanned across the pump/probe focus with a piezo stage. Excitation in the IR is typically provided by external-cavity QCLs (ECQCLs) [143–145] or by tunable OPOs [146–148]. ECQCLs offer faster frequency tuning (10000 $cm^{-1}s^{-1}$), narrower linewidths (0.1 cm^{-1}) and straightforward direct intensity modulation at rates beyond 100 kHz, but they suffer from a narrower spectral coverage (<300 cm^{-1}), which requires the combination of multiple sources to cover the fingerprint region. Differently, OPOs may entirely cover this region with a 10-times higher output power (Watt level), at the price of a fixed modulation frequency (often in the tens of kHz range), a slower tuning speed (100 cm^{-1} s^{-1}) and a broader emission linewidth (>10 cm^{-1}). The pump laser source is intensity modulated, either directly or externally via an optical chopper or an AOM, to extract the tiny PT signal in a modulation transfer scheme similar to that of SRS, that offers a higher signal-to-noise ratio. The detection system typically consists of an avalanche photodetector coupled with a LIA for demodulation. The interaction of pump and probe beams with the sample may occur either in a co-propagating or in a counter-propagating geometry [149]. The former has the advantage of a straightforward alignment and of an easier implementation of both forward and epi detection schemes for the signal, with epi detection needed for non-transparent media. On the other hand, co-propagation requires the use of reflective objectives with a relatively small numerical aperture (< 0.8) to focus both IR and visible beams on the sample, which is a limitation for the spatial resolution ($\approx$0.6 μm for a 785 nm probe, [145]). In a counter-propagating geometry, instead, immersion objectives for the visible beam may optimize the resolution to about 0.3 μm (for a 532 nm probe [148], the issue being in this case the need of a substrate with high transparency in the IR (typically CaF_2 or ZnSe).
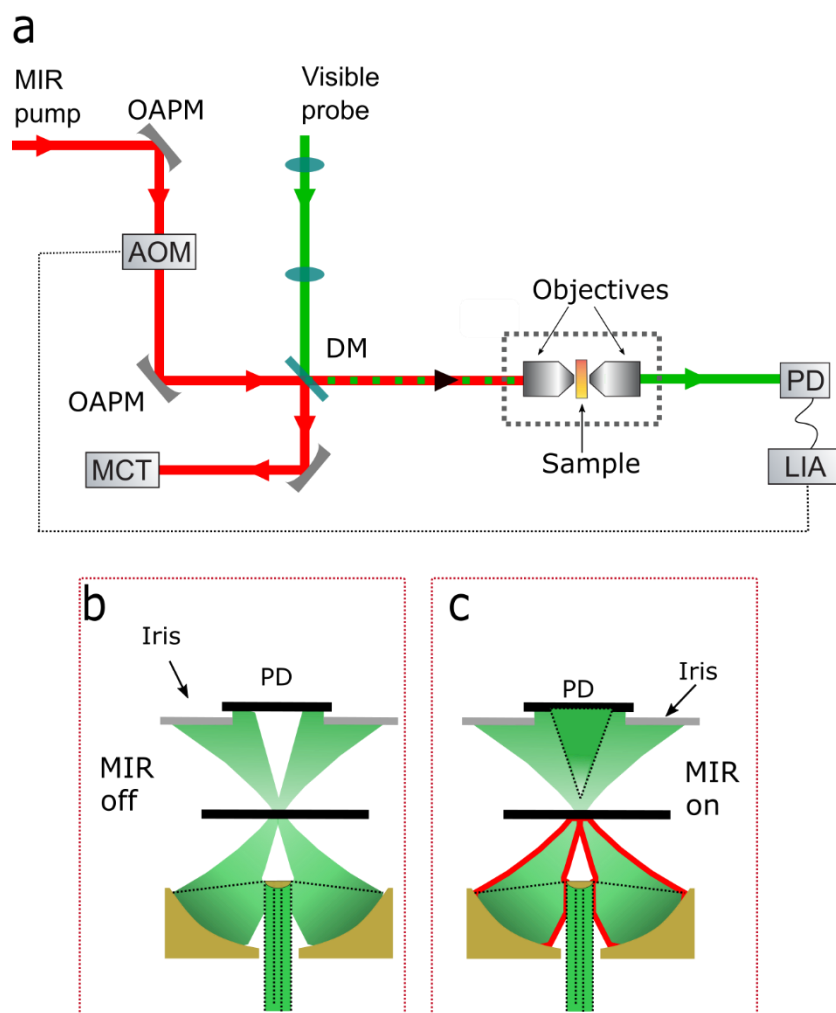
Fig. 19 Schematic lay-out of a single-point PT-IR microscope with forward detection. The IR pump beam is intensity modulated and the pump-induced molecular excitation synchronously detected through the effect that this excitation produces on a collinear visible probe beam. **b,c** A dark-field objective coupled with a diaphragm translates pump-induced local index changes into a modulation of the probe power reaching the photo-detector (PD), as it results by comparing the pump-OFF (b) with the pump-ON (c) case. OAPM: off-axis parabolic mirrors; DM: dichroic mirror. Adapted from [145].

Single-point PT-IR imaging has been successfully applied for the imaging of endogenous lipids and exogenous drugs in live cells [145], for the measurement of active pharmaceutical ingredients and excipients in drug tablets [150], for the characterization of perovskite-based solar cells [147] and for the study of cellular dynamics in oligodendrocytes and live neurons [151]. In live samples, specifically, pixel dwell times of about 1 millisecond have been obtained together with field of views of about 50x50 μm^2 [151], which implies imaging rates at the 0.1 Hz level. Faster rates, by one order of magnitude in the fingerprint region [146] and two orders of magnitude in the CH stretching region [152], have been recently demonstrated in wide-field geometries such as that shown in **Fig. 20**, which offer a much better spatial overlap between pump and probe beams and therefore a more efficient utilization of the available IR power. Moreover, thanks to the sensitivity of CMOS cameras, effective low-noise integration of the differential PT signal (between pump on and pump off states) may be obtained.

1 Three main geometries have been proposed: i) a counter-propagating epi geometry where the PT signal comes
2 from the reflectivity change of the sample at the probe wavelength because of the pump-induced thermal
3 expansion of the sample itself [146]; ii) a co-propagating forward detection geometry (shown in **Fig. 20**) that
4 efficiently exploits digital holography to convert the phase-shift pattern into an intensity pattern [152,153]; iii) a
5 co-propagating epi detection geometry where the pump-induced phase-shift is interferometrically retrieved by
6 translating the sample in the axial direction [154]. A specificity of the wide-field geometry is the need for a probe
7 beam with low spatial coherence to reduce speckle artifacts in the final image, which leads to the use of LEDs
8 [153,154], or of pulsed laser diodes [155] or of frequency doubled femtosecond oscillators [152]. For the IR light,
9 peak irradiation fluences are typically kept at the 10-50 pJ/μm^2 level, thus below the ANSI standard for IR induced
10 damage fixed at 100 pJ/μm^2.
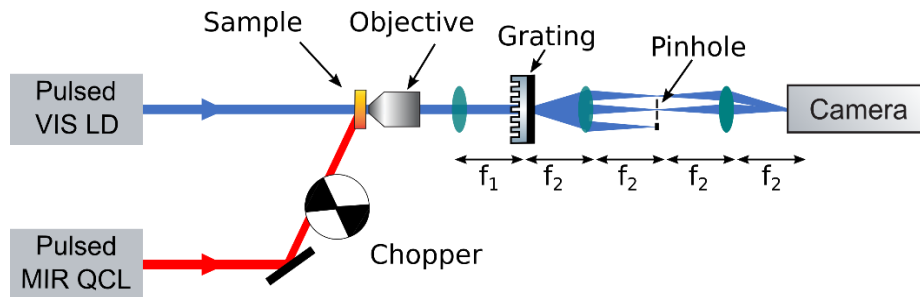
11
12

13 **Fig. 20** Digital-holography applied to PT-IR microscopy. The diffraction from a grating splits the probe beam in several
14 replicas that are made to interfere onto the camera, with one replica (upper blue beam in the figure) transferring the
15 sample-dependent phase pattern to the camera and a second replica (central beam in the figure) producing a flat phase-
16 front reference beam after spatial filtering with a pin-hole. The pump beam is intensity modulated and camera acquisitions
17 with "pump OFF" must be subtracted to camera acquisitions with "pump ON" for proper normalization and quantitative
18 phase imaging. Adapted from [155].

19

20 Influential aspects for the design and the performance of a wide-field PT-IR microscope are the duration and the
21 synchronization of excitation, probing, and framing events, which are schematically illustrated in **Fig. 21**. To
22 prevent heat diffusion and degraded spatial resolution, the pump pulse duration (τ_p) must be shorter than the
23 thermal response time (τ_{th}) of the sample, typically in the 1-100 μs range. In general, as a higher water content
24 speeds up the thermal response because of the fast thermal diffusivity, sub-microsecond pump pulses are
25 preferred for live samples. Likewise, probe pulses must be shorter than τ_{th} and sharply follow the pump pulses
26 to sense the sample at the highest temperature. The maximum repetition rate (f_{rep}) at which pulses can illuminate
27 the sample is limited by the need for the sample to cool down between excitation events, which results in f_{rep}
28 equal to the inverse of 4-to-6 times the thermal time constant τ_{th}. PTIR images are formed by subtracting the so-
29 called cold frames, i.e. the probe intensity patterns acquired by the camera in the absence of pump, from the
30 hot frames, i.e. those in the presence of the pump. An equal number N of probe events must be then integrated
31 in hot and cold conditions for the PT signal to emerge from the background, with N depending on the ratio
32 between probe pulse repetition frequency f_{rep} and camera frame rate f_{fr}. In most cases f_{rep}/f_{fr} ratios of about 10
33 have been used, one of the limitation being that cameras with large well depth, that are preferred because of
34 the lowest shot-noise limit, can't be easily operated at high rates (> 500 Hz).
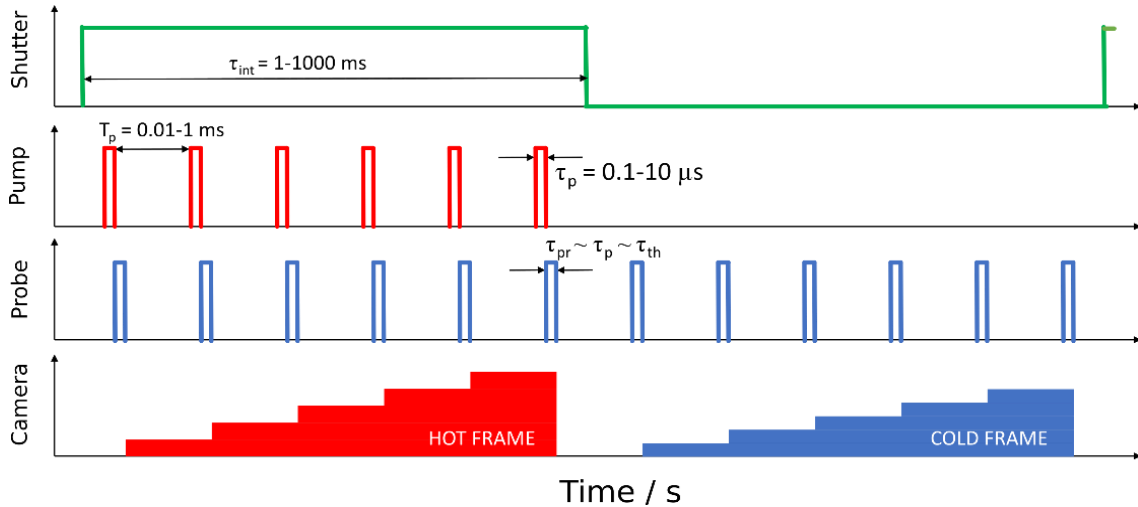
Fig. 21 Synchronization of pump and probe pulses in PT-IR microscopy. Pump (τ_p) and probe pulse durations (τ_{pr}) are chosen commensurate with the thermal time response (τ_{th}) of the medium, changing from sample to sample, in order to avoid heat diffusion and thus reduced spatial resolution. The probe pulse closely follows the excitation pulse to read out the temperature change at its maximum. The duty-cycle of the excitation, namely τ_p/T_p (with $T_p=1/f_{rep}$) is typically chosen lower than 50 % to avoid cumulative thermal effects. The camera integrates the signal over many pulses, the integration time τ_{int} being ultimately limited by the camera frame rate f_{fr}. As the photo-thermal signal comes out from the difference between pump-ON and pump-OFF images, the pump must be modulated (with a shutter, e.g) at a frequency ½ f_{fr} with a 50% duty-cycle to enable the correct normalization of hot frames with respect to cold frames.

36

3. Application of vibrational imaging to histopathology

Even if the first example of vibrational spectroscopy analysis of a biomedical tissue - using a Raman microprobe - was reported in 1979 by Abraham and Etz [156], systematic studies on cancer tissue samples have started in the early 90s, revealing the high potential of detecting pathology-related spectral features using the advantage of light-based label-free approaches. At that time, vibrational studies were mainly collecting single-point spectra on pre-selected tissue regions to identify specific biomolecular signatures associated to a particular pathological state, commonly using multivariate analysis, as extensively reported by previous review articles [157,158].

In this review we focus on "imaging" approaches for the study and diagnosis of cancer. When speaking about spectral imaging (e.g. SR imaging, FT-IR imaging, CRS imaging, PT-IR imaging etc.) we normally refer to vibrational approaches able to produce false-color images derived from the extraction of spectral data of a relevant tissue region of interest, preserving the spatial information with sufficient resolution.

Before tackling the description of the most relevant advances in the field it is worth answering a basic question: why imaging? This is not an obvious or trivial question if one considers that moving from spectra to images generally requires to greatly increase the measurement time, the system complexity, the analytical performances, and the interpretation efforts. In addition, we should also consider that, in some circumstances, pathological signatures could be extracted from body fluids or tissue lysates, thus analyzing the overall biomolecular composition of homogenous samples without the need for imaging techniques [159,160].

The first good reason for imaging is "morphology". The reason why medical doctors still rely on histological sections in the 21st century - the era of omics approaches, system biology and liquid biopsies - is that the appearance, the morphology and the spatial organization of cells and tissue is still of vital importance for the recognition of many tumors. The organization and distribution of cells and biomolecules into a specific tissue can be strongly associated to a given disease. This explains why, for most tumors, the very first diagnostic step is the visual evaluation of tissue samples. A second good reason for imaging is "biomolecular complexity". Ideal diagnostic tools should rely on the detection of a single, or a few, biomarkers, identified in readily available biological fluids (e.g. blood, urine, saliva etc). Even if hundreds of candidate cancer biomarkers have been reported and proposed, few of them are used in cancer care and, nowadays, there is not any single biomarker able alone to provide a definitive diagnosis. This intrinsically depends on the complexity of cancer biology and mechanisms. As a matter of fact, in most cases, the diagnosis of cancer made by pathologists counts on multiple complex criteria including the presence of specific morphological structures, the presence and percentage of specific cell subpopulations, the size and shape of cells, the alteration of surrounding healthy regions and the local response of immune cells (microenvironment). Only an overall and detailed description and observation of all these features in 2D (and ideally 3D) generally guarantees a correct cancer assessment and diagnosis. The third reason is "translational medicine", which is strictly related to the first answer. If new technologies want to enter the clinical practice, they should be accepted, understood, and assimilated by the clinical environment and medical doctors. In other words, vibrational images can be easily read by pathologists due to their similarity with standard H&E images and can be potentially introduced in the standard diagnostic pipeline without major changes.

These three reasons may help to understand why so many efforts and investments have been made, and are still pursued, to develop and optimize vibrational imaging tools for cancer diagnosis. Vibrational spectroscopy coupled to microscopy can simultaneously provide morphological and biomolecular details with objectivity and reproducibility. At the same time, referring to translational compatibility, vibrational imaging approaches are based on the use of the same samples employed by the pathologist; usually they correspond to thin tissue slices

contiguous to those used for the standard diagnosis. In addition, data emerging from vibrational imaging can be easily (computationally) colored thus providing images which very closely resemble standard stained histology slices.

In this section we overview the applications of the four vibrational imaging approaches (i.e. SR, CRS, FT-IR and PT-IR) to histopathology for cancer diagnosis and classification. We have chosen to describe the evolution of the technologies, accompanied by improved performances and results, following a quasi-historical criterion, by reporting the most relevant steps in the field.
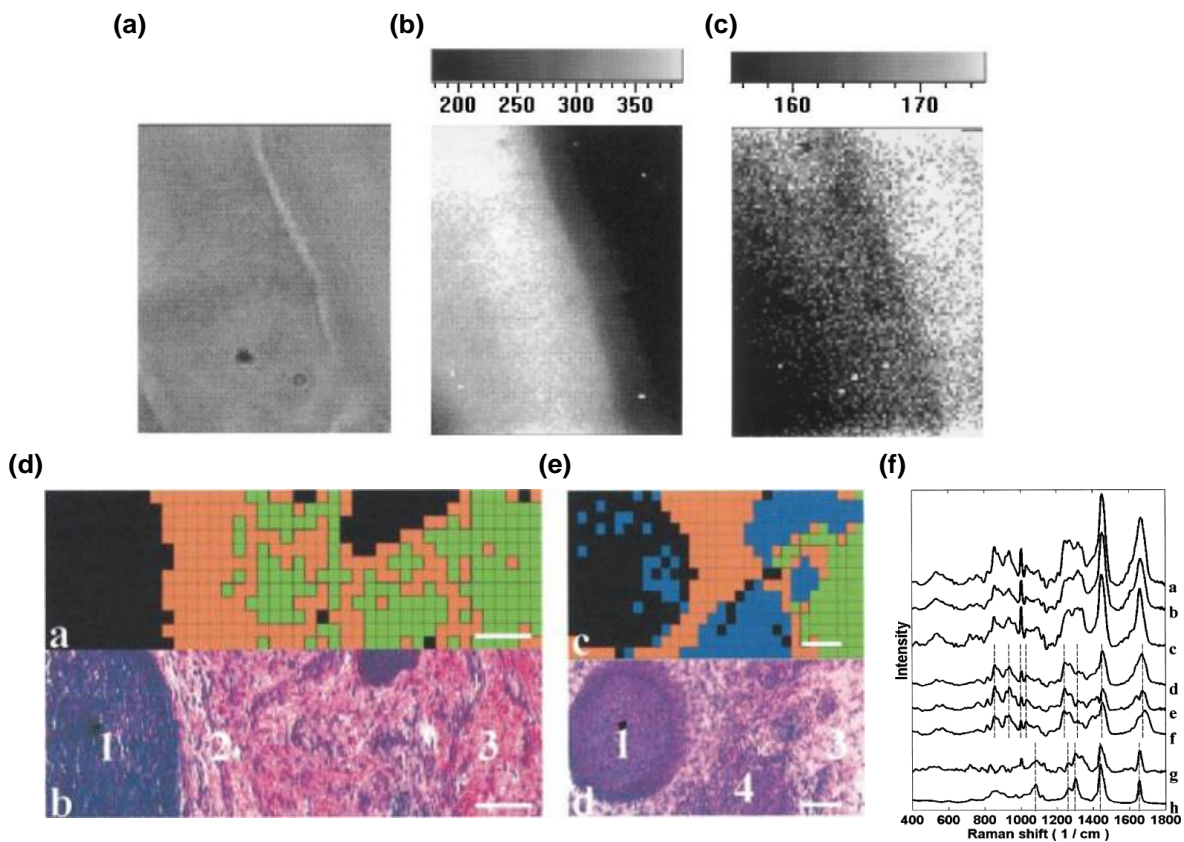
3.1 Spontaneous Raman Imaging

C. Otto *et al.* were the first to report SR images of tissue samples (1997) by recording the boundary between healthy eye lens and cataract regions [161] (**Fig. 22**a-c), while the first SR maps on cancer tissue were reported by Puppels and collaborators in 2002 [162] (**Fig. 22**d-f).


Fig. 22 Early Raman imaging experiments on human tissues. **a** bright field image of a cataractous human eye lens. **b** univariate Raman image at 1586 cm^{-1} related to filipine stain for cholesterol. **c** Raman image at 1004 cm^{-1}, related to phenylalanine (endogenous) and showing two different eye regions, with or without cataractous opacity. Scales on the top are related to signal intensity. Adapted with permission from [161]. **d,e** Raman maps of skin cancer (basal cell carcinoma, BCC) (black) surrounded by healthy dermis (orange and green), with H&E stained adjacent sections (bottom). In **e** a different clustering approach also shows inflammatory infiltration (blue). Scale bar: 100 μm **f** shows Raman spectra of clusters reported in panels d,e, including difference spectra and reference spectra. Adapted with permission from [162].

This pioneering approach aimed to determine the tumour margins by SR spectroscopy by extracting the local tissue composition and heterogeneity in skin cancer (basal cell carcinoma, BCC) biopsies. This clinical need was used as a driver to design one of the first SR imaging approaches. The study by Nijssen *et al.* reported an experimental and data-processing workflow which is not too far from protocols employed nowadays and can be used here to summarize a general approach to SR imaging studies. In detail, the complex workflow included: (a) the use of adjacent cryosections (25 μm thickness) from biopsies (b) placed onto Raman-transparent optical

1 substrates (CaF$_2$ slides) or (c) placed onto a standard microscope slide for H&E staining, to be used as diagnostic
2 reference. Moreover, (d) for each sample a selected area was scanned (using a motorized stage) in two
3 dimensions with a step size of 10 μm using a Raman microspectrometer coupled with a near infrared (850nm)
4 laser light (100 mW) focused on the sample by an 80x objective. (e) After a proper calibration and pre-processing
5 step the data were first analysed by principal component analysis (PCA) [163] to reduce the number of variables
6 in the dataset. Then, (f) principal components were used as input for K-means clustering analysis (KCA) [164]
7 which, in turn, is able to find groups of spectra with similar features. (g) For each cluster an average spectrum
8 was automatically calculated and (h) a colour was assigned to it to produce false-colours images to be compared
9 with H&E-stained tissue sections. After having defined different clusters, the challenge is to use these data to
10 classify healthy and cancer regions of the tissue. To this aim (i) all clusters detected in 15 tissue samples (each of
11 them also containing cancer regions) were assigned to different tissue areas (BCC (cancer)), dermis (healthy
12 tissue), and epidermis (healthy tissue)). (j) All classified clusters were then again analysed by PCA to reduce the
13 number of parameters representing the spectral variability of the entire dataset. (k) The scores of the first
14 principal components were then used as input for a multivariate model, together with the above-mentioned
15 histopathological classes. In details, a logistic regression was used to distinguish cancer *vs* healthy clusters. Finally
16 (l) the sensitivity and the specificity of the classification model were obtained by the so called "leave-one-out
17 cross-validation" approach [165]. In this approach, the spectra of all but one cluster mean were used to generate
18 the classification model and the excluded cluster mean was used as a test sample. This procedure was repeated
19 for each cluster of the dataset to define the method accuracy, finally scoring as 100% sensitivity and 93%
20 specificity for the recognition of cancer clusters. In parallel, the same group also reported the capability of Raman
21 imaging to discriminate tumour from necrotic tissue in unfixed human brain tissue slices [166] (**Fig. 23**). This
22 study sets the basis for real-time intraoperative biopsy or surgery guidance by vibrational-based approaches.
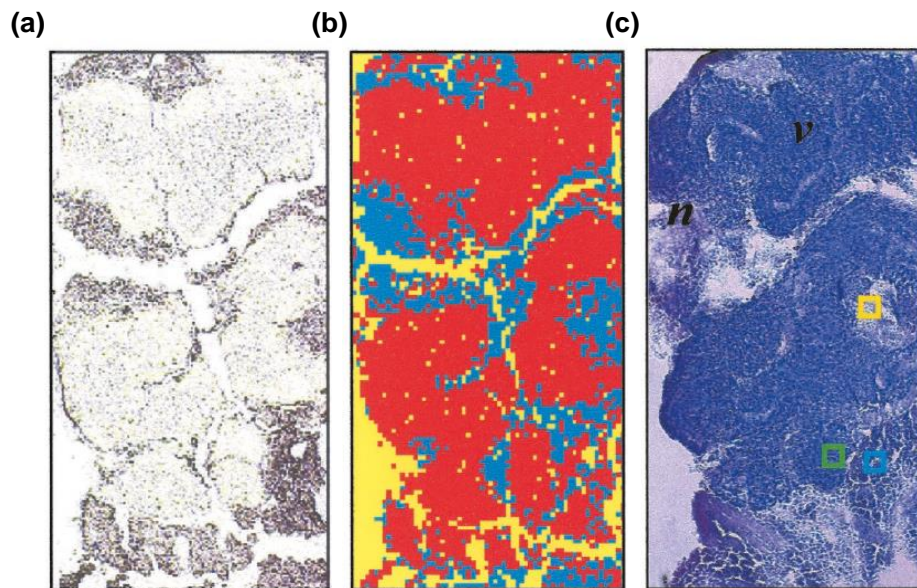

23

24 **Fig. 23** Raman imaging of glioblastoma (brain tumor) on human frozen cryosections. **a** bright field image of the unstained
25 tissue section recorded before Raman measurements (size: 1280 x 2420 μm). **b** Raman map obtained after linear
26 discriminant analysis (LDA) used to classify and predict vital (red) or necrotic (blu) regions in human glioblastoma. **c** the same
27 tissue section after H&E staining reporting vital (*v*) or necrotic (*n*) regions defined after histologic evaluation. Adapted with
28 permission from [166].

1

In the same period the group of Michael Feld from the Harrison Spectroscopy Laboratory (MIT, Boston) started to approach breast cancer diagnosis by Raman imaging, introducing the use of linear combination models to fit tissue spectra with reference spectra derived from various pre-selected tissue morphological structures or components (i.e. epithelial cell cytoplasm, cell nucleus, fat, beta-carotene, collagen, calcium, hydroxyapatite, calcium oxalate dehydrate, cholesterol-like lipid deposits, and water) [167,168]. As an example, **Fig. 24** reports, on the top, Raman images of breast ducts representing the contribution of specific tumour elements in the region being studied (i.e. collagen, cell cytoplasm, cell nucleus) well representing the possibility to automatically distinguish different morphological and biomolecular features. In parallel, the image shows (**Fig. 24** , at the bottom) how a linear combination model can be used to distinguish normal and carcinoma samples starting from the identification (fitting) of representative tissue components. These studies revealed that fit coefficients for fat and collagen are the key parameters in the resulting diagnostic algorithm, for distinguishing cancerous tissues from normal and benign tissues.
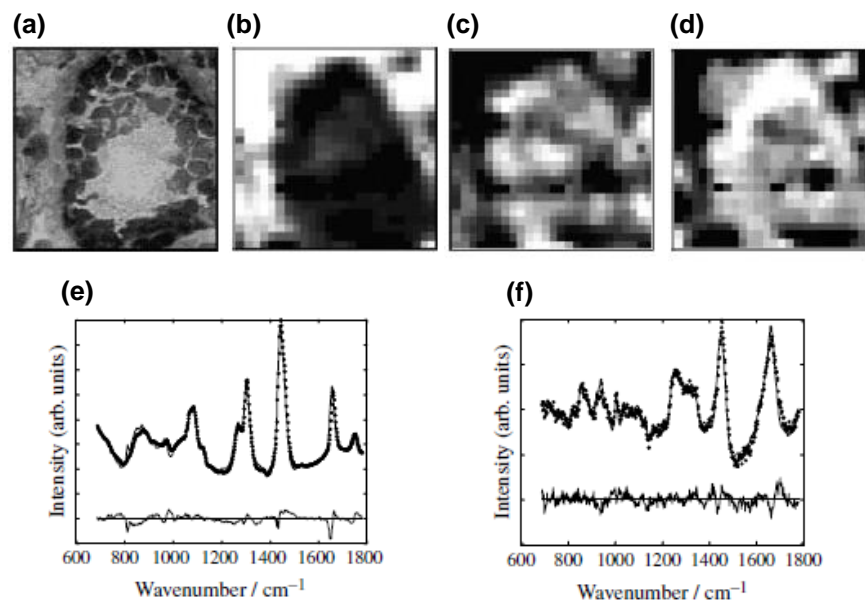
**Fig. 24** Raman imaging of human breast tissue. **a** H&E stained section. **b,c,d** Raman images reporting the contribution (brighter pixels are associated with higher signal) of collagen, cell cytoplasm and cell nucleus, respectively. (size : approx. 70 x 70 μm). **e,f** example of normal tissue and tumour (infiltrating ductal carcinoma) spectra, respectively. Bold dots represent data, the lines are the model spectra. Residual plotted below. Adapted from [167] (CC-BY-NC-SA 3.0).

With similar approaches, Stone and collaborators used Raman mapping approaches to elucidate biochemical changes in carcinogenesis of oesophagus [169]. In details, 20 μm thick fresh frozen tissue slices were mapped by a 830nm laser at 100μm step size across the whole sections (n=29) from 22 patients. Thereafter, a partial least square (PLS)-based algorithm was implemented in the data analysis pipeline in order to perform a fitting process using selected biochemical constituents (i.e. collagen, choline, actin, triolene, glycogen, DNA, oleic acid) after having identified the main biochemical changes by PCA. An example of mapping results is reported in **Fig. 25**. In particular, the score map resulting from PCA (scores of the third principal component) enables distinguishing

1 different regions with representative mean spectra (box in the middle). In addition, for each selected
2 representative region, the relative concentration of specific biochemical constituents is depicted (**Fig. 25c**).

3

(a)   **(b)**   **(c)**
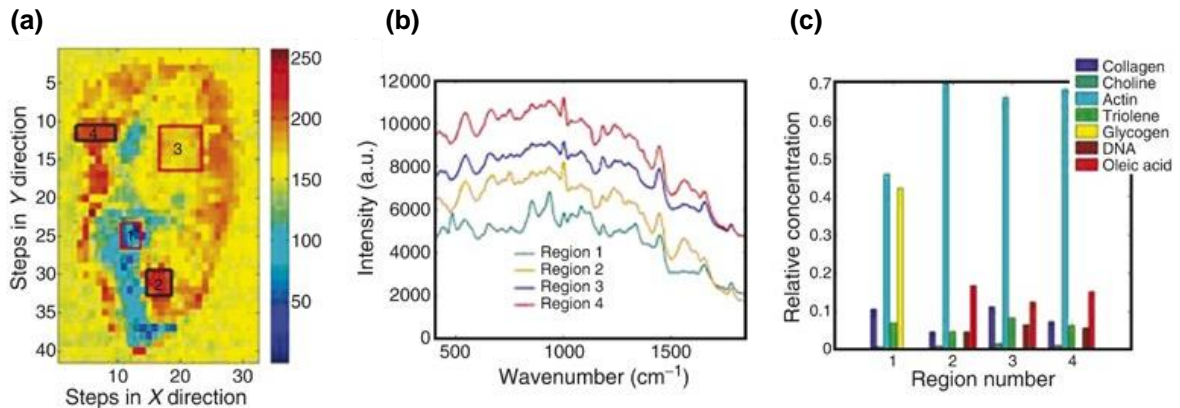
4 **Fig. 25** Raman imaging of human oesophagus cancer (adeno carcinoma). **a** Raman image reporting the score of principal
5 component (PC3), with selected regions marked. **b** mean Raman spectra from selected regions (panel **a**). **c** relative
6 concentration of selected biochemical constituents from selected regions. Adapted with permission from [169].

7 In 2007, Manfait and collaborators reported Raman mapping data of relatively large tissue regions (with average
8 size of 4x7mm) by collecting Raman spectra with 50µm step size [170] (**Fig. 26**). The clustering analysis of healthy
9 and brain tumour tissue correctly described their peculiar features. Furthermore, false-colour images showed
10 that Raman clusters provide more information than standard H&E staining. In details, the cortex regions (those
11 containing most neurons in brain tissue), when studied by Raman imaging, revealed the presence of four
12 different cortex layers with small but significant biomolecular differences, whereas H&E staining reveals a single
13 uniform layer. This is a good example to understand how much the morphological features extracted from
14 hyperspectral imaging data are strictly related to the specific biochemical and biomolecular composition of the
15 investigated region. In other words, Raman imaging can, in some cases, distinguish different biomolecular – and
16 therefore disease-specific – features, even if their morphology is very similar or identical and, consequently, very
17 difficult to be used for diagnosis by pathologists using standard H&E approaches.
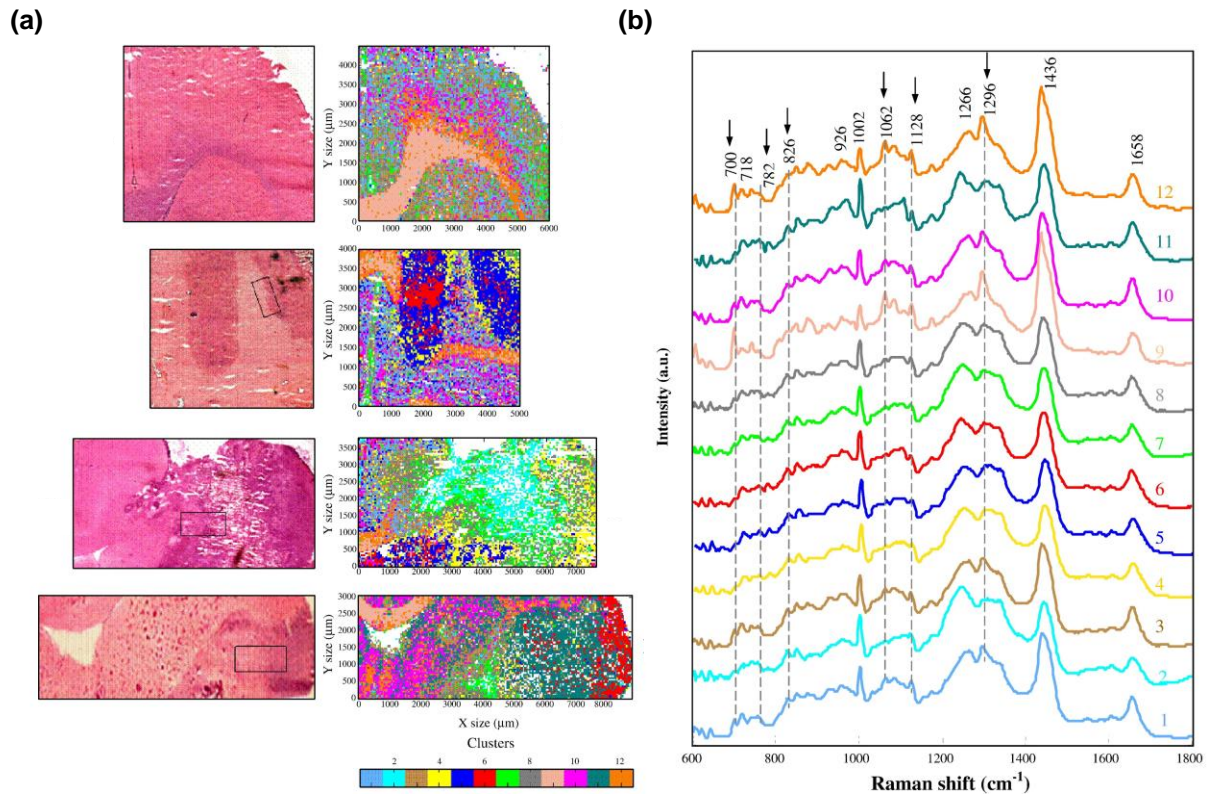
Fig. 26 Raman imaging of human brain tissue sections, including healthy and cancer (glioma) regions. **a** Raman images based on 12-means cluster analysis on sections (right) accompanied by H&E-stained contiguous tissue slices (left). **b** mean Raman spectra of each cluster, with the same colours. Adapted with permission from [170].

In parallel with the application of Raman imaging to different tumour types, a challenging frontier emerging in the field was related to data processing and statistical analysis of intrinsically complex imaging data, as a prerequisite to bring Raman imaging closer to the clinical application. For example, most literature reported the use of "unsupervised methods", such as KCA and PCA, which are limited by the fact that only the information contained in a specific sample can be used for classification, thus inhibiting the use of the same information to automatically classify new samples. At this concern, Nothingher and collaborators started proposing supervised automatic methods for the classification and detection of skin tumour (BCC) in normal skin tissue (i.e. dermis and epidermis) using Raman imaging data [171]. In details, supervised methods are based on the extraction of a relatively large amount of information, from numerous samples, that can be used to both classify this first dataset (so called "training dataset") but also to provide a classification of new samples (so called "testing dataset") not previously included. For this purpose, 329 tissue regions (50x50 μm), including both tumour and healthy regions from 20 randomly selected patients, were first studied to extract the corresponding average spectra and to build a spectral database. Then, the authors performed a linear discriminant analysis (LDA) for data classification and validation. LDA is a statistical tool able to provide the maximum separation between diagnostic classes that lead to different decision values and can be easily used to automatically assign every spectrum (including spectra never used to build the classification model) to a specific class (e.g. cancer vs healthy tissue). The input variables required to perform LDA must be numerically smaller than the smallest class contained in the dataset to be classified. A common practice is to use PCA of the entire original dataset to reduce the number of spectral

43

1   variables (usually between 200 and 1000 depending on the spectral resolution) to an acceptable number (< 20),
2   and this approach, usually called "PCA-LDA", is now commonly used in the field [172].

3   In a different approach, Nothingher and collaborators used as input variables the area of six selected Raman
4   bands, associated to DNA and proteins, previously identified as significantly different between BCC, dermis and
5   epidermis. According to the authors, this approach was optimal considering that the variability extracted by PCA
6   is not always distributed between different diagnostic classes. In addition, a preliminary qualitative analysis of
7   the dataset may sometimes reveal significant spectral features already associated to different diagnostic classes.
8   After having tested and validated the classification model using the 329 spectra emerging from small tissues, the
9   authors applied LDA-approaches to identify cancer (BBC) on a set of 6 large images (around 500 x 500 μm^2). To
10   this aim, they used two different approaches (**Fig. 27**). For the first method (k-means method) the entire dataset
11   was processed by k-means clustering to reduce its complexity while still preserving the spectral separation for
12   the detection of cancer features. Then, for each cluster (n=11), the ratios of the six above-mentioned Raman
13   bands calculated on the cluster centroid spectrum, were used as input for the LDA model. As a result, each cluster
14   was automatically assigned to one diagnostic class in the false-colour images. The second method applied the
15   LDA model using the same six Raman bands ratios used before as an input, but directly to the individual spectra
16   constituting the Raman images. In this second method, each spectrum, and not each single cluster, was classified
17   according to the possible diagnostic classes.

18   Even if the k-means-LDA approach showed better performances, both approaches were able to accurately
19   recognize BCC in unknown skin tissue samples that were not used to build and train the classification model. This
20   evidence has been a good demonstration of the possibility to use SR imaging for the automatic recognition of
21   cancer in new samples after a good model training.
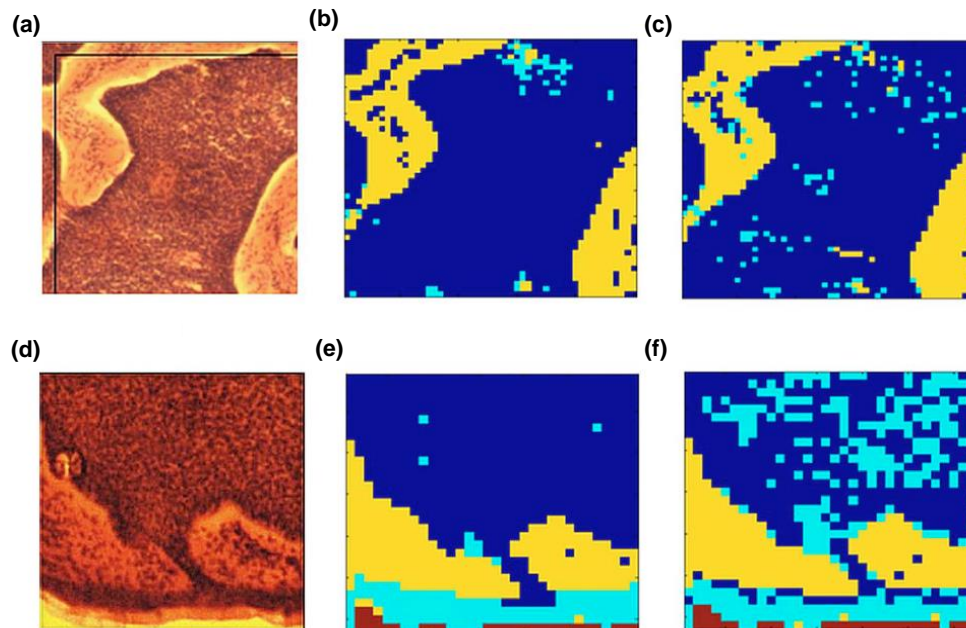
22

23   **Fig. 27** Comparison between H&E images (**a,d**) and Raman imaging of human skin cancer (basal cell carcinoma) produced
24   with two different supervised methods. **b, e** Images produced by the *k*-means method. **c, f** Images produced by the direct
25   LDA method. Tissue size: 500 x 500 μm^2. Adapted with permission from [171].

26

1   After the first evidence about the efficacy of SR imaging-based tools for the recognition of tumour features and
2   after the application of Raman imaging on different tumour types, many efforts have been made to move to the
3   clinics. A very important limitation of SR imaging has always been its intrinsically low acquisition speed. The
4   collection of SR images with lateral resolution between 10 and 20 μm (i.e. from 2500 to 10000 spectra per mm^2)
5   usually takes between 40min to >20 h/mm^2 (considering at least 1 second per spectrum) due to the intrinsically
6   weak signal generated by SR. If we consider that histological samples are typically between 30 and 100 mm^2 in
7   size (reaching millions of spectra), diagnosis of entire tissue specimens, with a spatial resolution almost two
8   orders of magnitude worse than that achievable with H&E, would require many hours to several days. This is
9   surely not compatible with intra-operatory diagnosis (total time from 30 to 120 min depending of type of tumour)
10   and still far from standard diagnostic procedures considering that the current protocols to obtain H&E-stained
11   slices from the excised sample usually takes 12 to 72h. This is also the reason why several reported studies
12   collected Raman images from small tissue regions (usually of max 1 mm^2) that were previously selected as regions
13   of interest from samples with full size ranging between 25 and 100 mm^2 [171,173,174]. This approach cannot be
14   feasible if Raman is to be used as unique diagnostic approach without the intervention of pathologists.

15   Some strategies have been suggested to circumvent the low speed of imaging procedures without necessarily
16   increasing the acquisition speed or changing the acquisition modality (see "line-scanning" or "wide-field"
17   modalities in section 2.1). For example, Kong *et al* from the Notingher's group, proposed the so called "multi-
18   modal spectral histopathology" (MSH) by applying automated segmentation and pre-selection of diagnostically
19   relevant tissue sections by using autofluorescence to prioritize sample points for SR spectroscopy [175–177].
20   After recording wide-field autofluorescence images for the detection of tryptophan and collagen signals, an
21   unsupervised image segmentation algorithm was used to determine and exclude dermis segments (characterized
22   by strong collagen-related autofluorescence) thus automatically selecting segments more relevant for the
23   detection of cancer (BBC)[175]. As an example, on tissue samples of around 1-cm^2 size, a number of spectra
24   ranging between 500 and 1500 were used to reach 95% sensitivity, thus reducing the total acquisition time to
25   20-60 min (including 4 min for the autofluorescence collection) (**Fig. 28**).
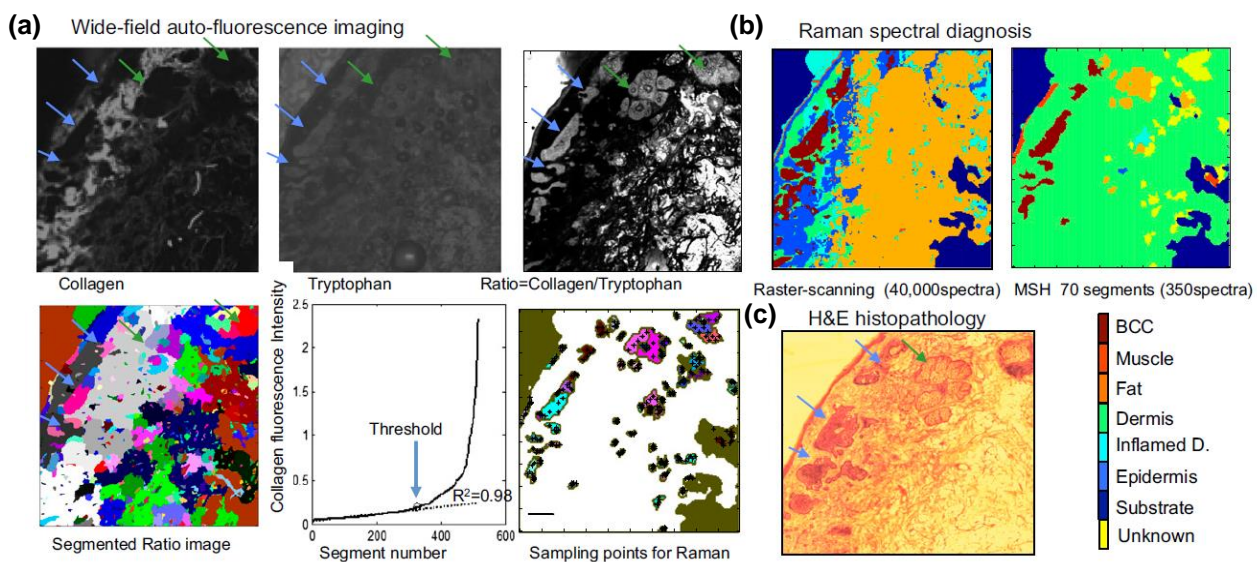
26

27   **Fig. 28** Example of MSH based on the use of auto-fluorescence to pre-select regions of interest to be further mapped by SR.
28   **a** (top) Wide-field auto-fluorescence images of collagen, tryptophan and collagen/tryptophan ratio (from left to right), used
29   to identify and exclude dermis regions (with high collagen). **a** (bottom) Segmented image (left) after defining collagen
30   fluorescence intensity (middle) and segments selected for Raman measurements. **a** Standard Raman imaging approach

obtained by 200 x 200 raster scanning (left) and MSH obtained after Raman measurements on pre-selected segments. **c** H&E image of adjacent tissue section. Scale bar: 0.5 mm. Adapted with permission from [175]

A further key advance was the intra-operative Raman-based assessment of surgical margins during breast surgery [177]. In the case of breast surgery, large or very large tissues samples (up to 8x8 cm^2 area) need to be evaluated during the intra-operative assessment within 30 min, in order to permit the surgeon to evaluate the eventual resection of additional tissue (also called cavity shaves) and reduce the need for re-excision. At the same time, breast cancer, especially the infiltrating variant, may present small and dispersed tumour regions that can be assessed by discrete spatial resolution (10-20 μm). Nothingher and collaborators attempted to answer this need by applying MSH (i.e. the use of autofluorescence to guide Raman spectroscopy) on 51 fresh breast tissue samples (up to 4 x 6.5 cm^2) directly obtained from mastectomy from the operating theatre after optimizing and validating the diagnostic algorithm on 71 smaller frozen samples (up to 3.2 x 3.2 cm^2). Also, in this case Raman measurement points were identified automatically by autofluorescence-based segmentation and a minimum of two points per segment were selected for Raman measurements using 0.3s as acquisition time. A second Raman acquisition round with doubled acquisition time per spectrum (0.6s) was performed when tumour-related spectra were associated to tissue segments. This approach allowed to analyse the entire surface of large tissue specimens by fewer than 2000 Raman measurements, therefore reducing the acquisition time by up to 200 compared with the typical raster scanning approaches, while still providing good and comparable accuracy performances. The authors introduced a scoring method (i.e. "tumour score") with optimized thresholds defining moderate or high risk of tumour score to improve the interpretation of emerging results and to easily guide the surgeon about excision strategies (**Fig. 29**). The moderate-risk threshold, used to reduce false negative, made it possible to obtain 91% sensitivity and 83% specificity in the independent validation test on small frozen samples. Finally, fresh, whole breast samples collected and measured immediately after surgery permitted to demonstrate the feasibility of the intra-operative use of the proposed Raman-imaging method, considering an average time of 12-24 min for the whole procedure. This study can be considered one of the current frontiers of SR-based approaches for cancer diagnosis by spectral histopathology, especially considering the unique short acquisition time, compatible with clinical workflow. It is important to note that this has been permitted only by coupling the high chemical specificity and selectivity of Raman spectroscopy (affected by slow acquisition speed) with a complementary approach (i.e. autofluorescence microscopy) to guide the Raman acquisition on selected tissue regions.

On the other hand, not all tissues give the chance to clearly pre-select healthy regions as has been done here for skin and breast. The autofluorescence-based approach to pre-select regions of interest is not always accurate and some tumours can be found in regions smaller than 50μm^2, thus making their recognition by this approach very difficult. In summary, the possibility to obtain spectral information from whole – or relatively large - histological samples with high accuracy and relatively high spatial resolution is still the main challenge for SR microscopy.
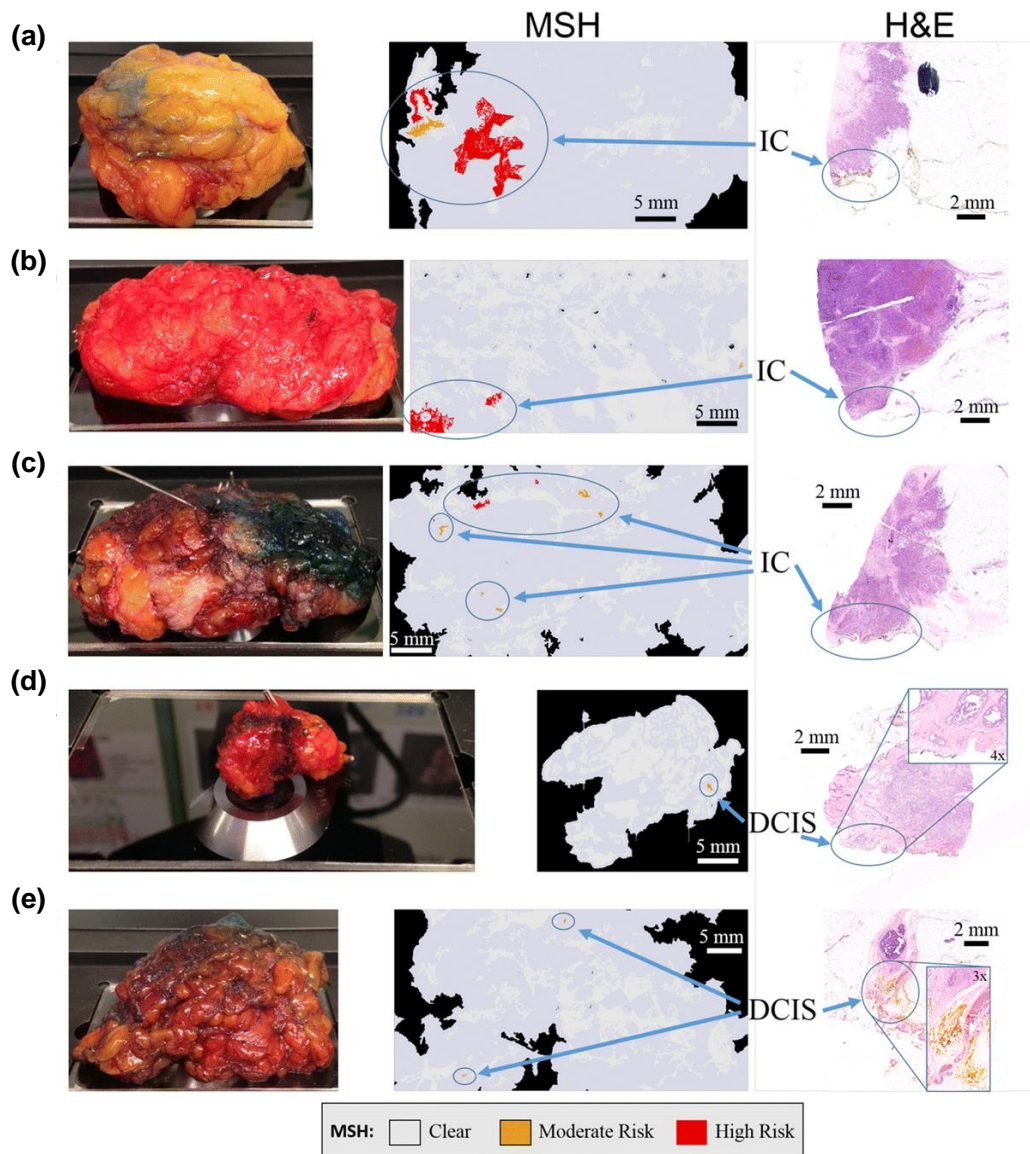
Fig. 29 Example of MSH on whole breast cancer samples after conservative surgery. **a-c** invasive carcinoma (IC). **d-e** ductal carcinoma in situ (DCIS). Adapted from [177] (CC-BY 4.0).

3.2 Coherent Raman scattering (CRS) imaging

As described in detail in **Section 2.2**, CRS imaging, including both CARS and SRS approaches, provides much higher signals if compared with SR imaging, thus permitting much faster scanning of large samples and imaging speed up to the video rate. In addition, CRS approaches are intrinsically confocal and allow deep tissue penetration, without being significantly affected by autofluorescence background. This paved the road to many biomedical imaging applications that were hardly reachable by other vibrational techniques, including the monitoring of cellular processes in living cells and living organisms with sub-cellular spatial resolution. At the same time, and especially when CRS systems were at an early development stage, the fast image acquisition came at the price of reduced chemical contrast if compared with SR and FT-IR techniques. Several technological and computational solutions, described in detail in **Section 2.2**, helped to increase the imaging performances and bring them closer

1   and closer to currently unmet clinical needs. In the next paragraphs, we will describe this improvement path and
2   the latest remarkable results obtained in the field of cancer histopathology.

3

4   The first demonstration of CRS imaging for biomedical applications was reported in 1999 by Zumbusch, Holtom
5   and Xie [39], using CARS microscopy to resolve components of living cells. Thanks to nonlinear excitation,
6   enabling intrinsic 3D sectioning, and thanks to high imaging speed, enabling time-lapse imaging on living samples,
7   the first CARS imaging systems could be extensively applied and tested on living cells [178], living animals [179]
8   and ex-vivo thick tissues [180]. These applications are only marginally related to histopathology and have been
9   widely discussed in previous reviews [14,181–183]. Considering that the technical aspects and differences
10 between several proposed CRS imaging systems have been described in detail in **Section 2.2**, we will summarize
11 here only the major results of CRS imaging applied to histopathology, following a chronological criterion, without
12 a precise separation between SRS and CARS approaches.

13 Two CARS studies carried out on fresh tissue samples (skin and spinal cord) by the groups of Xie and Cheng in
14 2005 [180,184], respectively, demonstrated the ability to image tissues of relevant size (squares between 100 to
15 500 µm) at very high speed (< 1s per image) and spatial resolution (<0.5 µm), and with satisfactorily high focal
16 depth (>100 µm) and axial resolution (<2 µm) (**Fig. 30**a,b). In addition, both studies demonstrated the capability
17 of CARS to collect strong signals in the *epi*-direction – more compatible for some tissue-based studies - without
18 losing much signal if compared with the standard forward-detection configuration. A few years later, in 2007, Le
19 et al. started cancer studies by CARS microscopy focusing on the mechanisms that link obesity to tumorigenesis
20 [185].
21 Most CARS studies, especially those at the early stage, were focused on lipids detection and therefore applied to
22 the investigation of lipid-rich tissues (e.g. brain, breast or skin) and of diseases where lipids dysregulation is
23 implicated (obesity and tumorigenesis). This is due to the abundancy of CH stretching bonds in lipid molecules
24 associated with strong resonant peaks (i.e. CH_2 stretching band, at 2845 cm^{-1}), where the non-resonant
25 background (NRB) is less affecting the spectral features, as compared to the fingerprint spectral region (see more
26 details in Section 2.2). At the same time, lipids detection might not be sufficient to discriminate relevant
27 biological features and pathological morphologies. For this reason, before the technical evolution of CRS
28 methods – in particular SRS and broadband CRS – some groups coupled CARS with other nonlinear microcopy
29 techniques such as second harmonic generation (SHG) and two-photon excitation fluorescence (TPEF)
30 microscopy, exploiting their high optical and technological compatibility (one of the two pulses used for CRS can
31 be employed for SHG and TPEF). **Fig. 30**c shows one of the first CARS images on histologic tissue sections (5 µm
32 thick), reported by Le et al. [185] for the study of adipocytes in mammary gland tumor tissue. In this case,
33 mammary gland sections were studied by CARS to detect lipids (red), monitoring the symmetric CH_2 stretch
34 vibration (2840 cm^{-1}), and by SHG to detect Type I collagen fibrils (green). A few years later, also Meyer et al.
35 studied brain tumor tissue sections (20 to 50 µm thick) by coupling CARS, TPEF and SHG [186] (**Fig. 30**d). CARS
36 was used to detect white matter lipids; TPEF was used to detect the autofluorescence of nicotinamide adenine
37 dinucleotide (NAD), elastin, keratin and other molecules relatively abundant in the grey matter; SHG was used
38 to selectively display the collagen contained in the arachnoid membrane, which envelops brain structures.

(a)   **(b)**   **(c)**   **(d)**
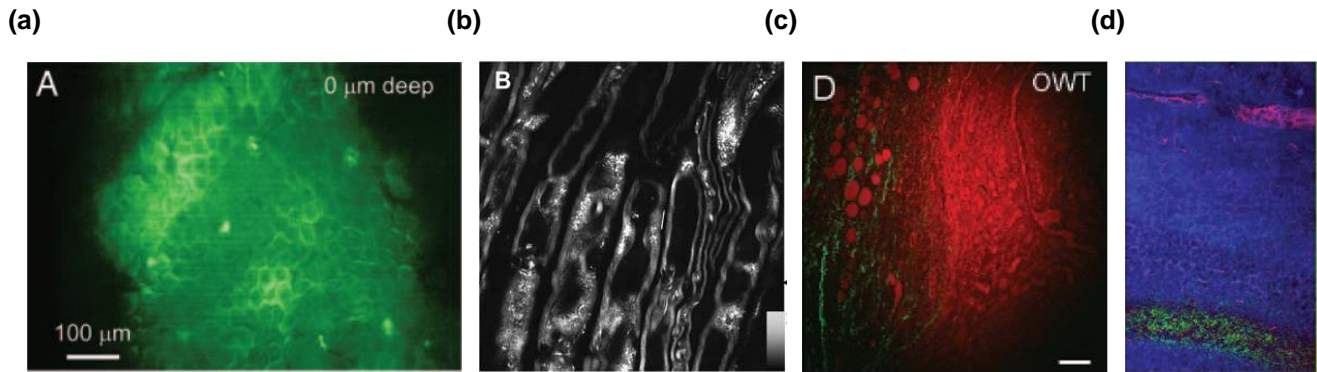
Fig. 30 Early examples of CARS images. **a** CARS image of living mice acquired by selecting the band at 2845 cm^{-1} (lipids). Adapted from [180]. Copyright (2005) National Academy of Sciences. **b** CARS image of axons in a guinea pig spinal cord sample by selecting the band at 2840 cm^{-1}. Adapted with permission from [184]. **c** multimodal image of histologic section from rat tumour. Lipid band in *red* and SHG of collagen fibrils in *green*. Adapted with permission from [185]. **d** brain tumour tissue section studied by a multimodal approach including CARS, TPEF and SGH. Adapted with permission from [186].

In parallel, between 2007 and 2009, SRS imaging systems were developed [40,41,187,188] permitting to obtain better vibrational contrast and to overcome some limitations of CARS, first of all the spectral distortion originating from the NRB, as better detailed in **Section 2.2**. Following these technical innovations, Saar *et al.*, in 2010, imaged skin of living mice in video-rate frames by showing signal coming from vibrations of lipids (CH$_2$ stretching, 2845 cm^{-1}), water (OH stretching, 3250 cm^{-1}) and proteins (CH$_3$ stretching, 2950 cm^{-1}) [44].

In 2012, Freudiger *et al.* reported multicolour SRS imaging, selecting vibrations from lipids, proteins, water combined with two-photon absorption from haemoglobin of red blood cells, aiming at reproducing H&E staining patterns on fresh 1-mm-thick slices [189]. In this case, the selected molecular features are imaged in different scans, by tuning the system to the corresponding frequencies and by further overlapping the different images using image processing tools. This is a common approach for single-frequency CRS systems that do not provide complete spectra for each imaged pixel, as is the case for SR and broadband CRS imaging systems (described later). The authors were able to obtain images with good contrast from fresh mouse brain tissues, as shown in **Fig. 31**. For a better comparison, the merged images were coloured using pink, blue-purple and red tones, producing images resembling H&E-stained sections, with satisfactory results. After proving the image quality, four common brain pathologies including glioblastoma, metastases, demyelination, and stroke, were investigated, and successfully compared with H&E images.
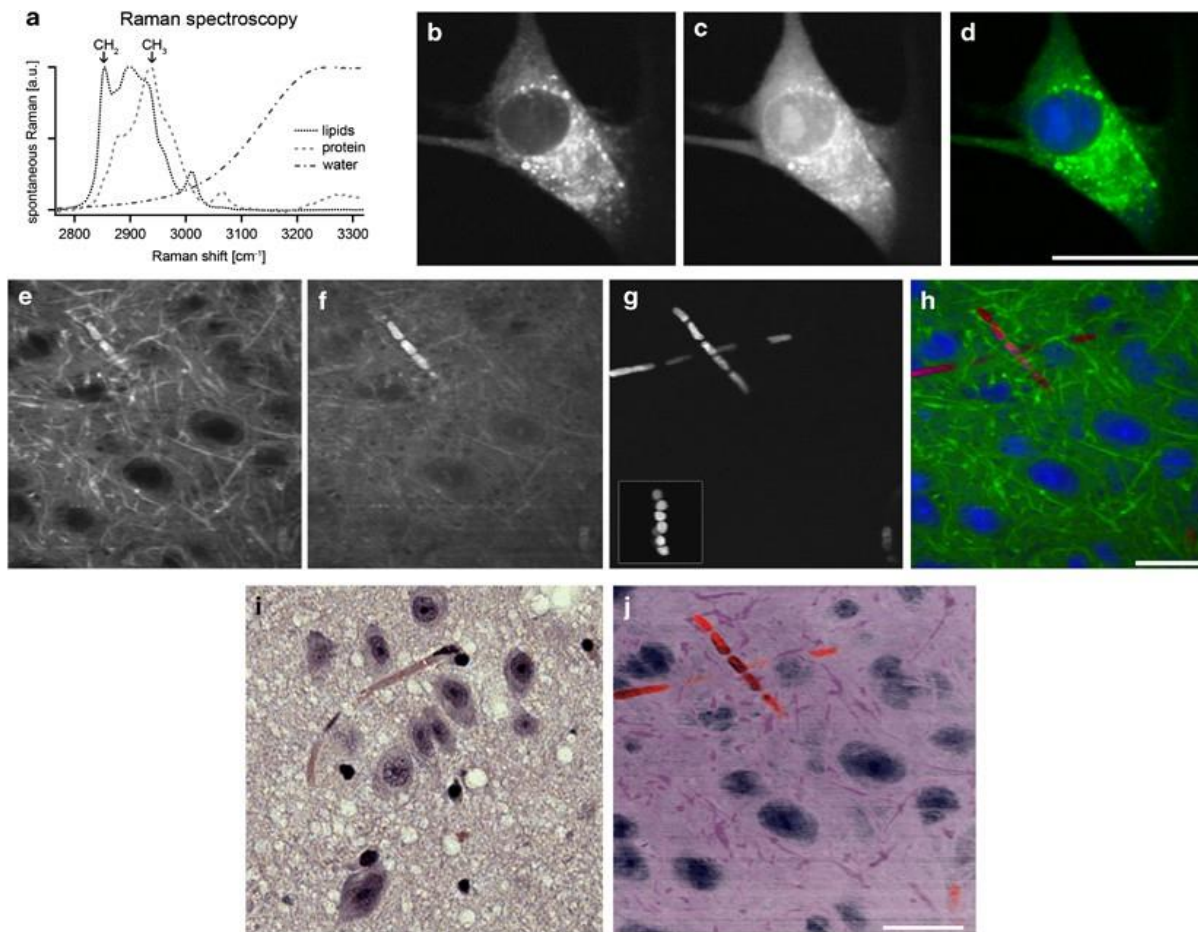
Fig. 31 Early examples of SRS images of cells and fresh 1 mm tick mouse brain tissue slices. **a** vibrational spectra of lipid, proteins and water. **b, c** SRS image of live neuronal cells by using the Raman shifts at 2845 cm^{-1} (lipids) and at 2940 cm^{-1} (proteins), respectively. **d** false colour image produced by merging the lipid signals (green, image **b**) with difference between proteins and lipids (blue, image **c** minus image **b**). **e,f,g** SRS image of fresh *ex-vivo* brain tissue acquired selecting the band of lipids at 2845 cm^{-1} (**e**), the band of proteins at 2940 cm^{-1} (**f**), and using two-photon adsorption of haemoglobin (**g**). **h** false colour image generating by merging images **e-g**. **i** H&E stained adjacent tissue slice. **j** same multicolor image as (**h**) but using a H&E pseudo-color scheme. Scale bar: 25 µm. Adapted with permission from [189].

In the meantime, Chowdary *et al.* [190] reported an interesting hybrid solution derived by coupling CARS and spectral interferometry (called spectral reconstructed nonlinear interferometric vibrational imaging (SR-NIVI)). This system can be considered as a broadband CARS apparatus because it provides spectra from 2800 to 3100 cm^{-1} that can be used to extrapolate band intensities of specific molecular vibrations. The authors demonstrated the ability to distinguish carcinoma from healthy tissue in rat mammary tumour model, used as a proof of concept, even if at relatively low scan rate (1 ms per pixel, followed by averaging over ten images) and lower spatial resolution (5 µm), if compared to other CRS approaches tested at that time. Another broadband multiplex CARS approach, reported by Pohling et al, was tested on fresh mouse brain tissues showing the exceptional possibility – at that time - to record a full (biologically relevant) spectrum, ranging from 500 to 3400 cm^{-1}, thus covering both the fingerprint and CH regions [59]. Sample areas of 100x100 µm were raster scanned with step size of 1 µm and acquisition time per pixel between 20 and 200 ms. This configuration, coupled with PCA, permitted to distinguish grey and white matter as well as different brain tissue layers. On the other hand, the

spectral information in the fingerprint region was highly affected by background noise and the imaging speed reached up to 5h/mm^2, still far from being compatible with clinically relevant applications such as intraoperative tissue assessment.

Following the demonstration of SRS microscopy, Xie and collaborators started in 2013 to put much effort towards label-free, fast, and accurate cancer assessment at a clinical level. Ji *et al.* reported the use of an SRS microscope in epi-detection mode to perform two-color imaging at 2845 cm^{-1}, which is a suitable region for lipids and therefore for white matter observation, and at 2930 cm^{-1}, which is generally related to proteins and offers good contrast in cellulated parts of brain cortex and tumor [191] (**Fig. 32**). The linear combination of these two frequencies permitted to extract lipid and proteins contributions and to produce two-colors (blue and green) images with good structural and chemical contrast. From the translational point of view, it is important to note that two-color brain images were collected from the study of thin (10 µm), unstained, snap-frozen sections, which were further stained by H&E for comparison. This experimental configuration is basically identical to the protocols used for the intraoperative tumor margin assessment using snap-frozen sections, with the important difference that SRS images do not require any type of staining. As a next step, the authors tested the possibility to detect glioma (brain tumor) by SRS, approaching for the first time a rigorous and relatively extended validation step. In details, seventy-five 350×350 µm^2 fields of views (and corresponding seventy-five H&E fields of views), collected from 6 mouse brains with glioma, were visualized and blindly classified by three pathologists, yielding to 450 observations. By the observation of SRS two-colors images, the pathologists were asked to distinguish three different tissue categories: 1) normal hypercellular tissue; 2) infiltrating glioma; and 3) high-density glioma (**Fig. 32**). Only very few images were misclassified, and the overall accuracy was 99.5%. Furthermore, also *ex-vivo* human brain tumor samples were studied after surgical excision revealing similar image contrast as observed in mice. This was the first evidence that SRS microscopy can be used for diagnostic purposes for the intraoperative detection of cancer. In this context, Uckermann *et al.* reported CARS images of mouse brain tumor (glioblastoma) by only selecting the CH$_2$ stretching vibration band (2850 cm^{-1}) showing that this band inversely correlates with tumor features, i.e. producing darker regions in sick areas due to a lower CARS signal [192]. In addition, they also showed that highly cellulated regions, like normal hippocampus, produce a significantly higher CARS signal, thus suggesting that the observed decline of CARS signal is a common and intrinsic tumor feature, compared to both (healthy) grey matter and white matter, mostly associated with tumor-induced changes like nuclear size and nuclear density.
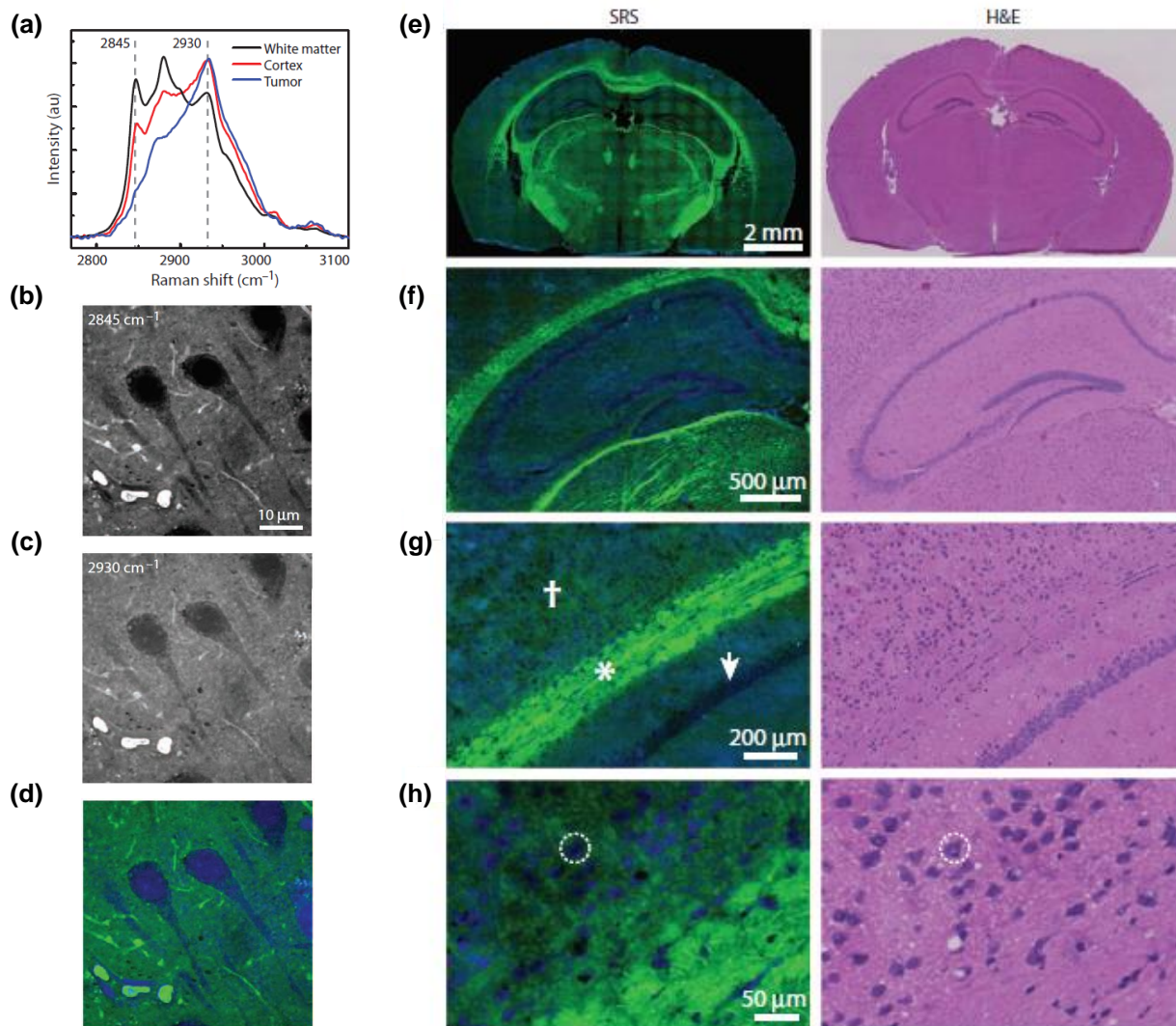
Fig. 32 SRS images of mouse brain frozen sections. **a** vibrational spectra of white matter, cortex and tumour. The marked frequencies are those used for two-colour SRS imaging. **b, c** SRS images using lipid signals (2845 cm^{-1}) and protein signals (2930 cm^{-1}), respectively. **d** multicolour image produced by a linear combination of images **b** and **c**. **e-h** SRS multicolour images (left) accompanied by images of tissue slides stained with H&E after SRS measurements. From **e** to **h**, different imaging size was used, from full coronal section to single neurons. imaging scale was reduced till visualizing single neurons. Adapted with permission from [191].

The aforementioned SRS imaging studies mostly exploited the vibrational band of lipids (~2850 cm^{-1}) or, in some cases, those of proteins (~2930 cm^{-1}) and/or water (~3250 cm^{-1}), to produce pseudo-color tissue images and to study or discriminate cancer. On the other hand, nucleic acids, and in particular DNA, were rarely included among the selected "colors", mostly due to the intrinsically low scattering properties of nucleic acid bonds in both the fingerprint and CH stretching regions. This has been a limitation considering the functional and structural importance of DNA (and of cellular nuclei) in tumors and, more generally, in all biological systems. At that time, only one study attempted to visualize the DNA phosphate peak in cultured cells detected in the fingerprint region but with scarce contrast [193]. In 2015, Lu *et al.*, from the Xie group, extracted pure Raman spectra of DNA from cellular extractions and pure molecules, thus proving that SRS is able to detect DNA, in particular the CH

1 vibrational signal from deoxyribose (around 2956 cm^{-1}), which differs from the CH response of proteins and lipids
2 [194]. Then, three Raman shifts (2850, 2926 and 2967 cm^{-1}) were selected to optimize the detection of the three
3 biological species (i.e. lipids, proteins and DNA), and linear decomposition approaches were applied after using
4 premeasured calibration matrixes (**Fig. 33**). This study resulted in the first DNA detection in live cells undergoing
5 division, in living mouse skin to follow cell division and, finally, in human skin with diagnostic purposes.
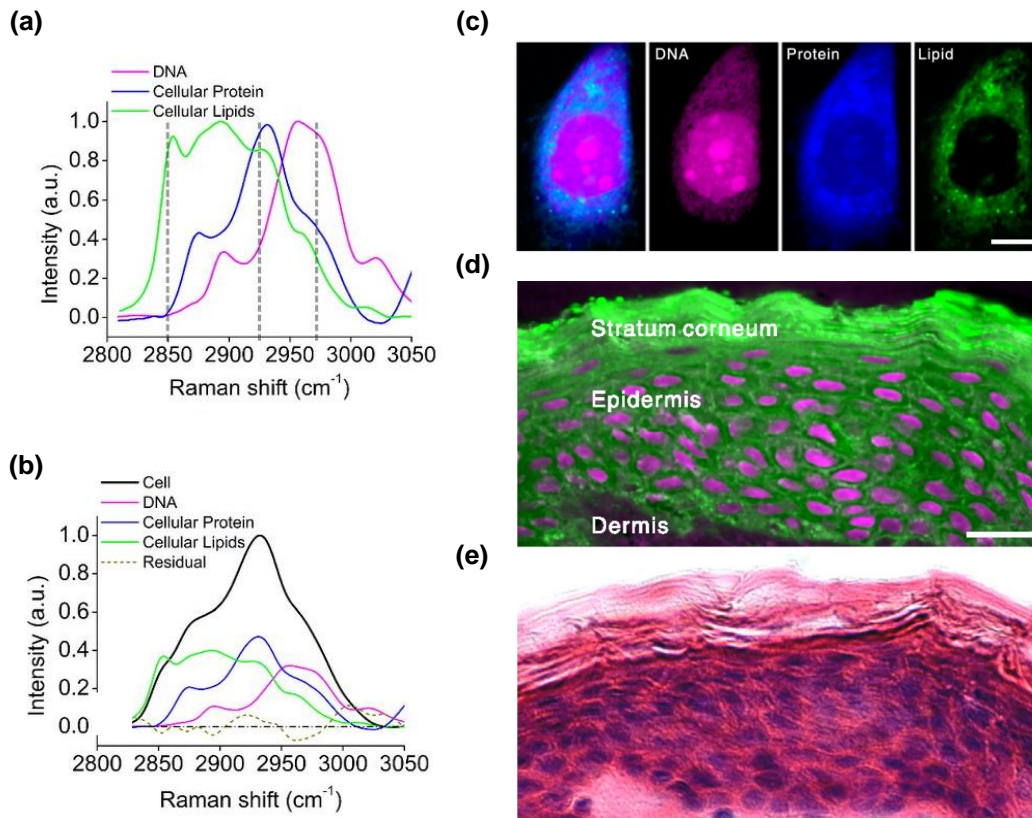

6

7 **Fig. 33** SRS images of DNA (magenta), proteins (blue) and lipids (green). **a** vibrational spectra of DNA, proteins and lipids
8 extracted from HeLa cells. **b** Raman spectrum of cell homogenate (black) and linear fitting of DNA, proteins and lipids
9 signals demonstrating that 90% of these components accounts for around 90% of the total CH stretching vibration of the
10 cell. **c** SRS images of live cells using the colour scheme mentioned in **a**, including an image presenting the merge of the
11 DNA, Protein, and lipid channels (left). Scale bar 10 μm. **c** SRS images of human skin (20 μm tick), accompanied by H&E-
12 stained section (**e**), showing typical cytologic features. Scale bar 20 μm. Adapted with permission from [194].

13

14 In 2016, the SRS-based assessment of 41 brain tumors specimens from 12 patients represented the first clinically
15 relevant study in the field of CRS-based diagnostics [195]. Both 12-μm thick (snap-frozen) and 1-mm thick (fresh)
16 brain slices were studied by an SRS microscope able to image 350x350 μm fields of view in approximately 1s with
17 ≈ 0.68-μm transverse resolution. Here, the SRS signals from proteins (2940 cm^{-1}) was obtained after subtraction
18 of half the signal from lipids (2850 cm^{-1}) and these two channels were imaged as blue and green, respectively. In
19 parallel, a third channel (magenta), was obtained by selecting the Raman-silent region around 2800 cm^{-1} and
20 assigned to hemoglobin. Typical morphological features were visible in the SRS image when compared with H&E-
21 stained sections, including cell density (hypercellularity), necrosis, collagen, and vascular proliferation.
22 Noteworthy, some histological features, like the boundary between the gray and the white matter, were better
23 visible in the SRS images than in H&E stained tissue images due to the removal of lipids during sample preparation

1   (i.e. including solvents) before standard staining protocols. Another important observation is that nuclei from
2   individual cells were clearly visible in both SRS and H&E images, even without selecting the specific wavenumber
3   associated with DNA, as optimized by the same authors in a previous study [194].

4   Simultaneously, also CARS imaging was successfully evolved and applied to histopathology, mostly thanks to the
5   integration of CARS, TPFE and SHG, for the reasons mentioned above. The Popp group, in a strong collaboration
6   with clinicians, applied CARS and other nonlinear microscopy approaches for the diagnosis of brain cancer, skin
7   cancer and laryngeal cancer [196–198]. In particular, in 2016, Heuke *et al.* reported the multimodal study of 30
8   frozen tissue sections (20-μm-thick) from head and neck cancer patients aiming to validate the potential use of
9   nonlinear microscopies – including CARS – as diagnostic tools [197]. Tissue specimens as large as 1.5x1.5 cm were
10   imaged using the three modalities in around 1.5 hours with a lateral step size of 220nm (**Fig. 34**). Multimodal
11   images revealed that cancer regions were mainly associated to an increase of TPEF – most likely from increased
12   cellular NADH – while other regions generally showed higher intensity of CARS and SHG, respectively associated
13   to lipids and collagen. The authors attempted to use TPEF to SHG or TPEF to CARS signal ratios from the whole
14   tissue sample to distinguish malignant features and verified that the TPEF to CARS ratio significantly differs
15   between healthy and cancer specimens. At the same time, this approach was not accurate enough for an
16   automated prediction and for the spatially defined assignment of malignant regions. For this reason, statistical
17   properties of the intensity histogram of the multimodal images (mean, standard deviation, smoothness,
18   uniformity, entropy, etc) were calculated for each imaging modality. A total of 18 image features were then used
19   to classify all 30 multimodal images by LDA. As a reference, a trained pathologist assigned a distinct tissue type
20   (i.e. 8 different classes including benign and cancer tissue) to each region. Overall, the pixel-weighted average
21   accuracy for the identification of cancer vs healthy epithelium vs other tissue types vs background was found to
22   be 74%.
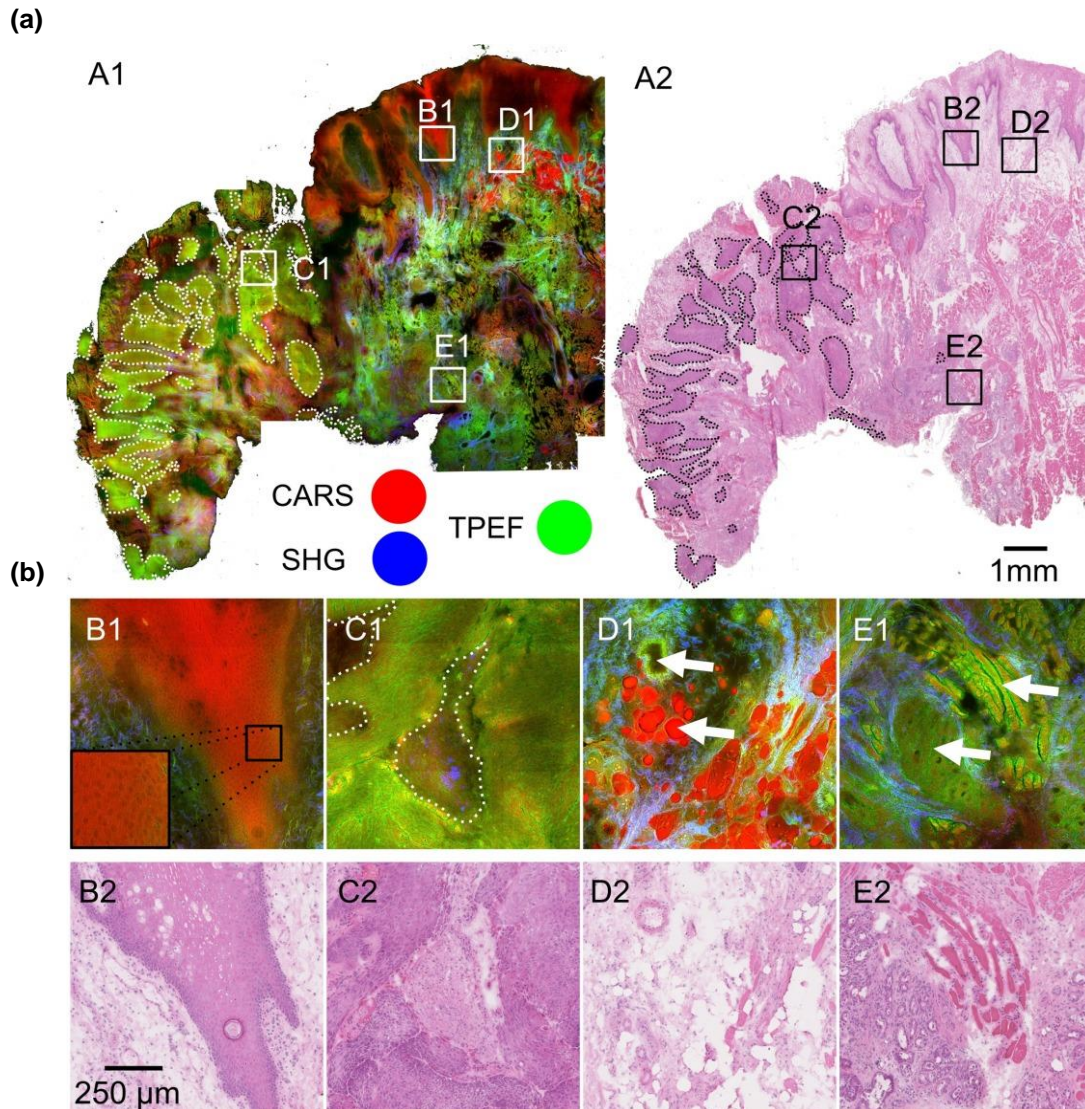
Fig 34 Multimodal image of a large (1.5 x 1.5 cm) laryngeal cancer specimen. **a** Coherent anti-Stokes Raman scattering (CARS), second-harmonic generation (SHG), and two-photon excited fluorescence (TPEF) are displayed in false colours as red, blue, and green, respectively (left). The contiguous H&E-stained slice is also reported (right). Cancer regions are framed by with dotted lines. **b** different regions, characterized by different histological features and indicated also in **a**, are reported. Adapted with permission from [197].

Even if the accuracy reported by Heuke *et al.* was not comparable with the diagnostic performances currently obtained by pathologists on H&E-stained slices, this was one of the first studies attempting to use the spatial information and the identification of specific regions to automatically classify each sample. A few years later, in 2019, the same research group presented a new semantic segmentation approach based on fully convolutional neural networks to perform a pixel-wise classification enabling faster and more reliable classification of cancer specimens [199]. In details, 114 images from frozen tissue slices collected from 12 patients were studied ([197]) and the overall recognition of four different diagnostic classes was of 86.7%.

1

2 In 2017, a collaboration between Harvard University, University of Michigan medical school and Invenio Imaging
3 Inc. reported the first demonstration of SRS microscopy in clinical setting using unprocessed specimens from 101
4 neurosurgical patients [200]. The consortium focused its effort on improving intraoperative assessment of brain
5 lesions by use of SRS microscopy to provide rapid, reproducible and accurate diagnostic images to support
6 surgical decision making. A portable fiber-based microscope was designed avoiding any optical hardware
7 incompatible with the clinical setting. The two synchronized narrow-band laser pulses (pump and Stokes) were
8 generated by a broad-band supercontinuum derived from a single fiber-oscillator. The SRS microscope enabled
9 an acquisition time of 2 sec for 400x400um frames with step size of 390 nm and axial resolution of 1.8 μm (**Fig.**
10 **35**). The two Raman shifts associated to CH_2 bonds, mainly related to lipids (2845 cm^{-1}), and to CH_3 bonds, mainly
11 related to proteins (2930 cm^{-1}), were selected; the images were then reconstructed using the signal from CH_2
12 bonds as a first channel and the signal from CH_3 bonds minus that from CH_2 bonds as a second channel, similar
13 to what was already reported [195]. In addition, instead of using standard and previously used green and blue
14 colors to represent the chemical contrast given by proteins and DNA, respectively, here the authors used the
15 eosin-like reddish-pink and the hematoxylin-like dark-blue-violet colors to generate virtual H&E staining. The
16 overall time for the acquisition, stitching and recoloring was $\approx$5 min per millimeter square.
17 A total of 12870 frames were collected from 101 patients, corresponding, on average, to around 20 mm^2 and
18 around 100 frames per patients. For each patient, fresh tissue samples (approx. 3 mm thick) were collected and
19 analyzed after standard squash preparation reducing the thickness to 120 μm. When available, part of the tissue
20 was fresh frozen and examined using standard diagnostic approaches as a reference. It is important to note that
21 the squash preparation, used here for SRS imaging, is not commonly used in standard diagnosis, not even when
22 performing SR and other vibrational-based imaging approaches. This approach seems to be promising because
23 it does not require sample fixation/freezing and cutting, thus saving time, and avoiding any type of fixation or
24 any procedure that may alter the original tissue composition. On the other hand, when using this approach, the
25 exact comparison with adjacent frozen slices routinely stained with H&E is not feasible and, as claimed by
26 authors, some architectural features (e.g. microvascular structures) may not be well represented.
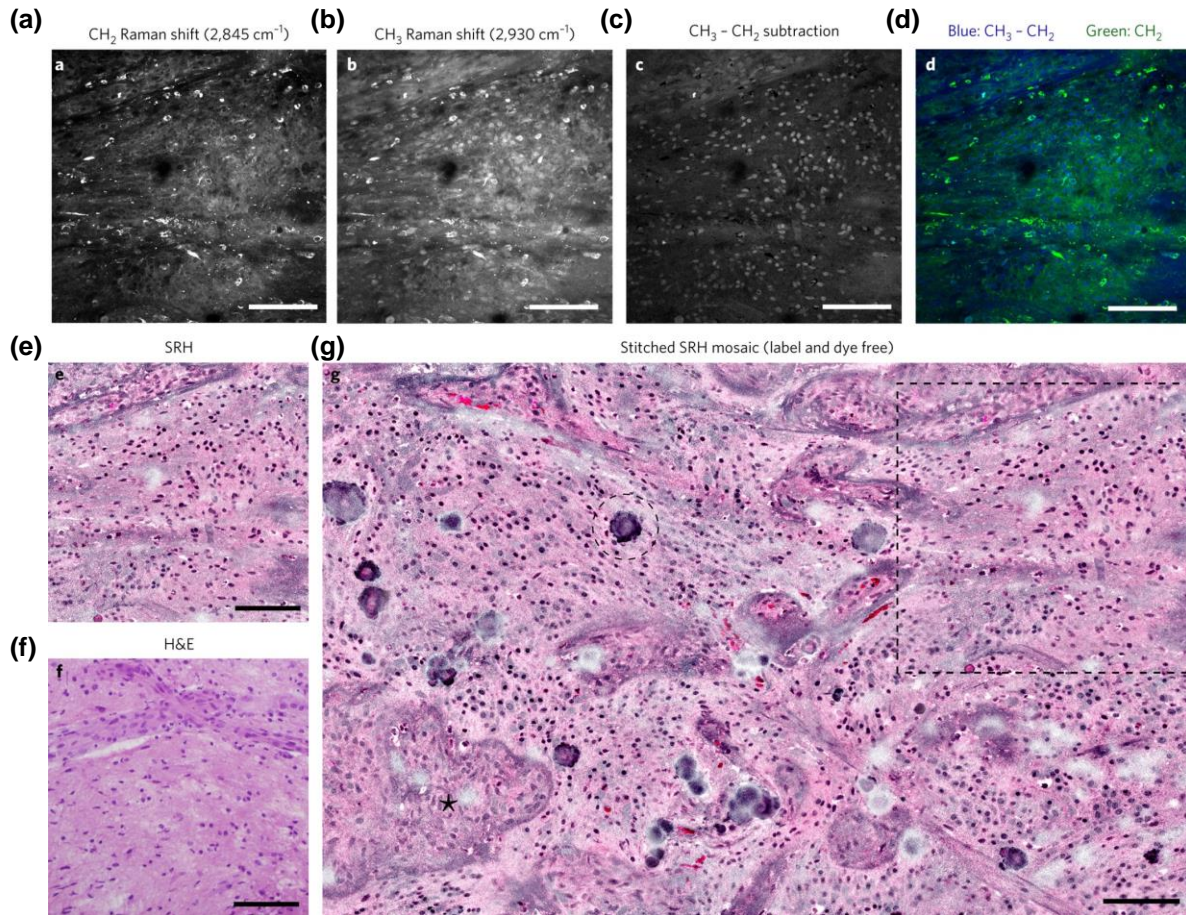
Fig. 35 SRS-based virtual staining of fresh human brain sections obtained intraoperatively. **a-c** SRS images produced by the integration of Raman bands of lipids and proteins, respectively, or by the subtraction of **b** from **a**, thus mainly showing cell nuclei (**c**). **d** multicolour image derived by the combination of **b** and **c**. **e** virtual staining applied to image **d**, to be compared to a similar section of brain tumour stained by H&E procedure (**f**). **g** mosaic image of several field of view of imaged tissue, including the field of view reported in panel **e** (dotted square). SRH: SRS-based histology. Scale bar: 100 μm. Adapted with permission from [200].

After confirming the detection of relevant diagnostic-histological features and of typical intratumoral heterogeneity, quantitative SRS-based diagnosis was evaluated. SRS images from 30 neurosurgical patients were collected and compared with routine diagnosis performed on adjacent fresh frozen sections. Then, three certified neuropathologists were asked to provide intraoperative diagnosis based on both SRS and conventional H&E (frozen) images. The concordance (Cohen's kappa (k)) of diagnostic performances when utilizing SRS versus standard H&E was very high for the identification of brain tumor lesions ($k = 0.84$ and 1.00, respectively) and for the definition of the final diagnosis (i.e. cancer subtype) ($k = 0.89$ and 0.92, respectively). Overall, the accuracy of SRS-based diagnosis was 98% in distinguishing pathological lesions and 92.2% in making the correct diagnosis. Finally, the task of interpreting histopathologic SRS images has been also entrusted to machine-learning approaches, to verify the possibility of a rapid, objective and automated tool for diagnosis and brain-tumor surgery. More than 12000 frames (400x400μm each) from 101 patients were analyzed by a multi-purpose image classification (called WND-CHARM) [201] that utilized 2919 image features to automatically classify each frame

into four diagnostic classes by a machine learning (multilayer perceptron (MLP)) approach. The frames (~3000) from 30 patients that were evaluated by neuropathologist for SRS and H&E comparison were used as a test set using leave-one-out validation. The remaining frames (~7000) were the training set. The result was that cancer vs benign lesions were detected with 100% accuracy by the machine learning approach when considering frames from the same patient sample. In addition, the accuracy for classifying individual frames (cancer vs benign) was close to 95% (94.1% specificity, 94.5 sensitivity). The final diagnosis (i.e. including cancer subtype) at sample level was 90% accurate if compared with the diagnosis provided by pathologists. The same SRS-based approach was further used for the intraoperative diagnosis of pediatric brain tumors with similar results [202].

Fu ad collaborators also performed SRS-based intraoperative assessment of tumours by applying similar approaches, including pseudo-H&E recolouring strategy and the use of fresh tissue samples pressed between two glass slides, on brain (skull base) tumours [203]. In addition to what was previously reported by Hollon and Orringer [200,202], here authors emphasized the comparison between standard and SRS-based histopathology by validating every step of the typical diagnostic workflow (histological features, differential diagnosis and final diagnosis) . As an additional added value, for each of 16 patients included in the study, three types of samples (and corresponding images) were obtained and examined by three pathologists with no training on SRS-based images: 1) virtually-H&E-stained SRS images from fresh tissue; 2) H&E images of the same specimen used for SRS images, after adequate fixation by FFPE protocols and standard staining; 3) H&E-stained images from frozen sections obtained during surgery, following the standard protocol used for intraoperative assessment in clinics (**Fig. 36**). The reason and advantage of using two reference samples is that H&E images from fixed tissue (sample n.2) represent the best diagnostic preparation considering image quality, used for routine diagnosis but not compatible with intraoperative assessment, due to the long preparation time; on the other hand, H&E images from frozen sections (sample n.3) represent the real SRS-image competitor, because they are the ones currently used for intraoperative assessment even if they are of lower quality due to scarce fixation and fast staining. Neuropathologists were able to detect histopathological features with almost perfect concordance (95%, average relative accuracy) when compared with conventional modalities. Differential and final diagnosis were performed with average accuracy of 94 and 86%, respectively. Noteworthy, this study also underlined the additional diagnostic chemical information intrinsically generated by SRS, especially about lipid and protein content, that cannot be extracted by the sole H&E images if not supported by additional labelling procedures (immunostaining). Finally, this study also suggests that virtually stained H&E images, although very useful to promote acceptance of SRS by the pathologists, are not always able to represent the chemical contrast, especially the lipid content, revealed by SRS but not perfectly represented by H&E-based approaches, which are intrinsically not optimized for the detection of lipids.
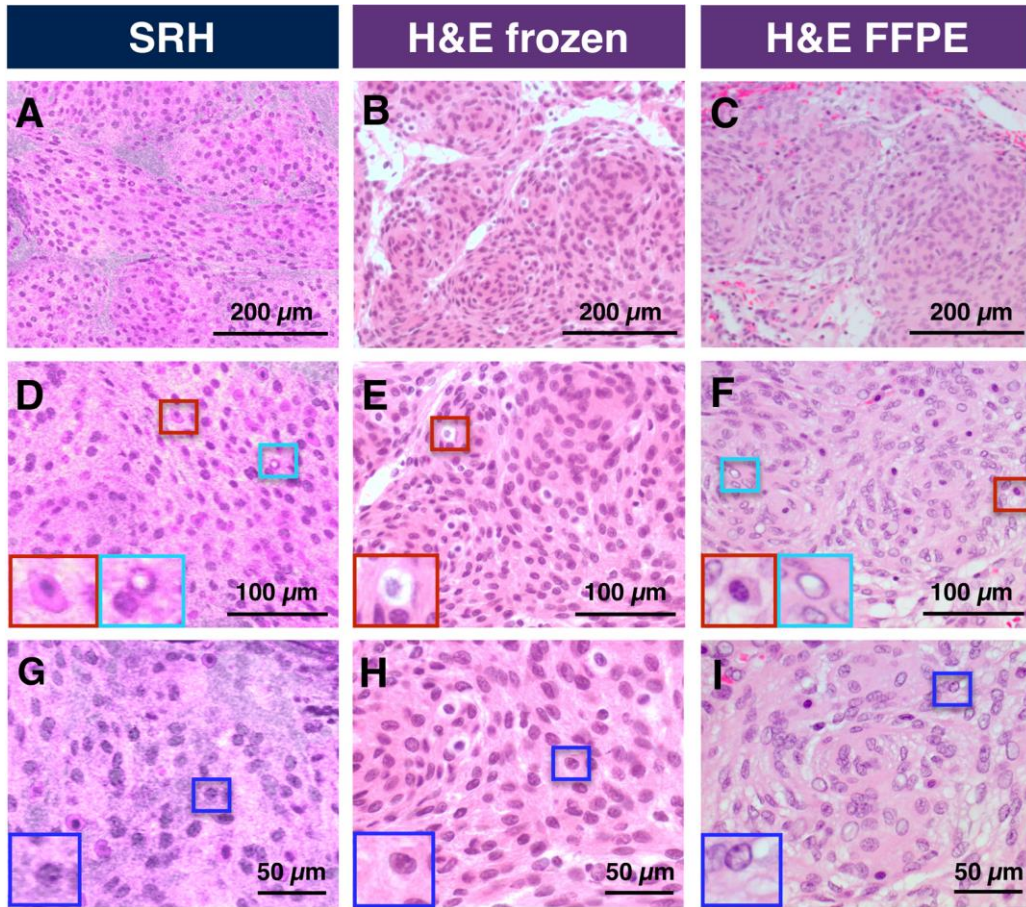
Fig. 36 Comparison of SRS-based histology (SRH) and H&E-stained slides prepared from frozen or formalin fixed paraffine embedded (FFPE) brain tissue samples. **a-c** SRS images produced by the integration of Raman bands of lipids and proteins, respectively, or by the subtraction of **b** from **a**, thus mainly showing cell nuclei (**c**). **d** multicolour image derived by the combination of **b** and **c**. **e** virtual staining applied to image **d**, to be compared to a similar section of brain tumour stained by H&E procedure (**f**). **g** mosaic image of several field of view of imaged tissue, including the field of view reported in panel **e** (dotted square). Scale bar: 100 μm. Adapted from [203] (CC-BY 4.0).

SRS-based spectral histopathology was also used by Ji and collaborators for the diagnosis of laryngeal squamous cell carcinoma, also thanks to the implementation of CNN approaches [204]. The system combined two-color SRS with SHG to mainly represent lipids (2845 cm^{-1}), proteins (2930 cm^{-1}) and collagen fibers (SHG). A total of 78 patients were involved in the study and two types of samples were selected: a) 80 frozen sections (20 μm thick, between two coverslips) accompanied by an equal number of adjacent H&E stained slices, were obtained from 15 patients and b) 78 fresh tissue samples (0.5mm thick, between two coverslips) were obtained from all 78 patients. Frozen sections were used to assess the concordance between SRS and H&E images (k = 0.90 and 94, repsectively) as reported by three independent pathologists, and the diagnostic accuracy when using SRS-images only (>90%). Fresh surgical specimens were used to evaluate the performance of SRS imaging on tissue samples free from freezing and sectioning, thus avoiding possible artifacts and/or alterations, and to mimic label-free and real-time intraoperative histology virtually excluding any tissue sample preparation. In this case, SRS images from fresh tissues were not directly compared with adjacent H&E images, as done for the frozen sections, but they were simply assigned as "normal" and "cancerous" according to the standard diagnosis (performed on separated and non-adjacent H&E tissue samples) and used to train and test the deep-learning-based (CCN) model. Then, 45 out of 78 samples (both normal and cancerous) were used as model training and the remaining 33 were used

as test set. A total of 18750 small tiles from the first 45 samples were randomly divided in five groups. Four groups were used for the training (15000) and the remaining one was used for validation (3750). A 5-fold cross-validation was performed by repeating 5 times the classification/validation process selecting each time different groups of data. The results showed an overall accuracy of 95.9%. Then, the remaining 33 untrained samples (test set) were differentiated by the previously trained model with 100% accuracy.

With the goal to make SRS-based imaging faster and more compatible with clinical and diagnostic setting, Rigneault and collaborators combined SRS, SHG and, eventually, CARS and TPEF, for the detection of colon and pancreas tumors in patients samples [205]. The multimodal non-linear optical microscope was applied to both fresh frozen thin (15μm) tissue slices and fresh tissue pieces (~1mm size) squeezed between two glass coverslips, thus reaching a thickness of around 100nm. Authors used two imaging modalities. The first, named λ-switch, was used to sequentially detect SRS signals related to lipids (2845 cm^{-1}, CH_2) and proteins (2930 cm^{-1}, CH_3), respectively, and SHG signals. This configuration permitted to scan a 1mm x 1mm tissue region in around 50 min (40 μs pixel dwell time x 3 accumulations) with 0.4μm step size (**Fig. 37**). The second modality, named frequency modulated-SRS (FM-SRS), permitted to detect, simultaneously, the signal corresponding to the nuclei (i.e. the ratio between 2845 and 2930 cm^{-1} signal) combined with the signal from collagen, by SHG, and the signal related to cell bodies (by TPEF or CARS), allowing to generate 1mm x 1mm tissue region in around 25 minutes. Also here efforts have been spent to produce false color images to simulate histology staining, similar to what has been proposed by Orringer and colleagues [200]. In this case, also collagen signals obtained by SHG were virtually added as orange color thus mimicking hematoxylin, eosin and saffron (HES) staining, like standard H&E but also able to distinguish collagen. In summary, this study reports the first application of stimulated Raman histology on gastro-intestinal tissues and demonstrates the possibility to obtain virtual HES staining with timing almost compatible with operatory room workflow.
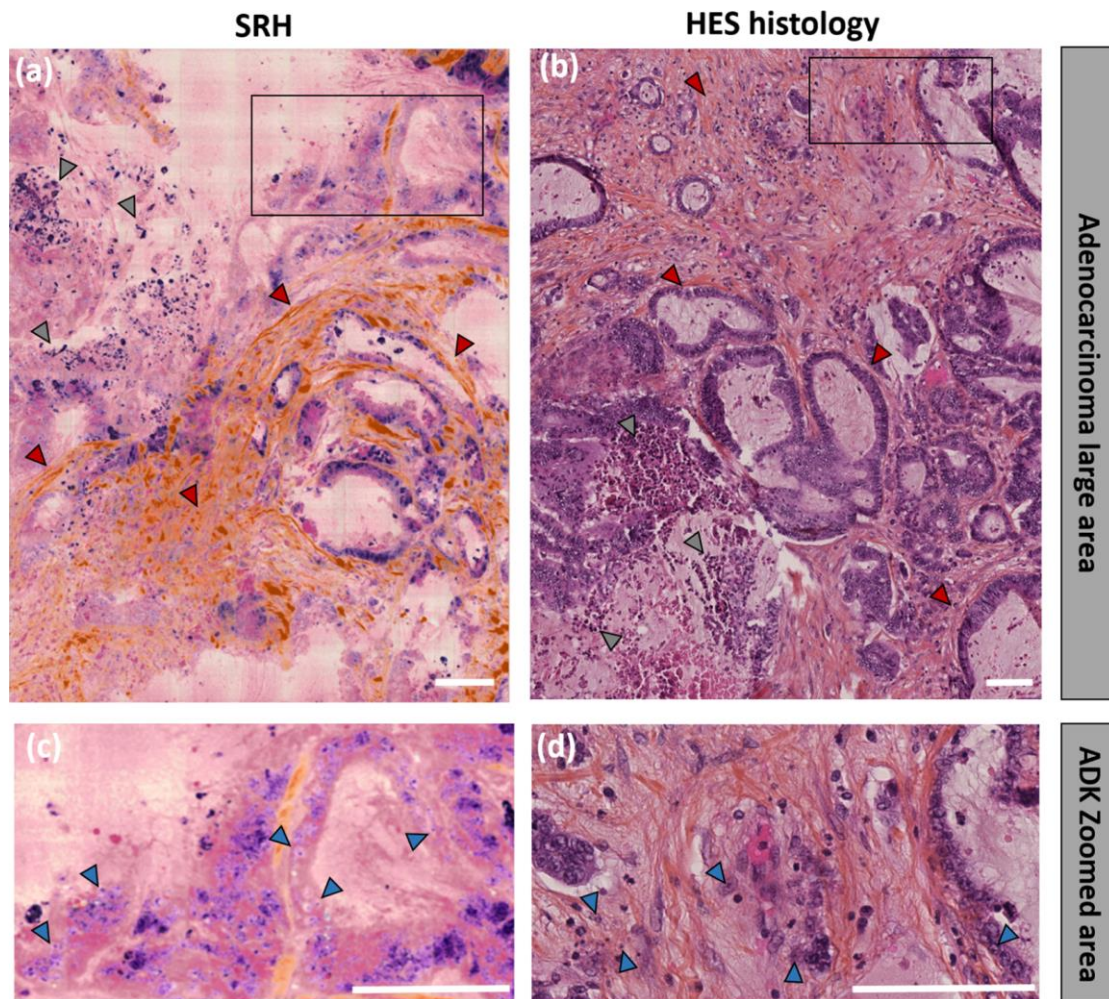
Fig. 37 SRS-based histology (SRH) compared with haematoxylin, eosin and saffron (HES) histopathology. **a** SRH image of human colon adenocarcinoma compared to HES image from the same region (**b**). **c,d** regions zoomed on the ROIs defined in (**a,b**). Scale bar: 100 μm. Adapted from [205] (CC-BY 4.0).

As a final example we report here the current frontier of the clinical application of CRS imaging – and, more in general, of vibrational microscopy – represented by the study by Hollon et al, in collaboration with Invenio Imaging Inc., published in Nature Medicine in 2020 [206] (**Fig. 38**). Starting from an already described SRS-based FDA-registered technology able to be used in the operating room, making histological data available during surgery [200], here the authors moved a step forward to clinics. This was done by coupling SRS-imaging to deep CCN to automatically provide diagnosis at the bedside and in near-real time (<2.5 min), thus being an order of magnitude faster than standard procedures based on fresh frozen preparation and on the interpretation by pathologists (20-30 min). A total of 278 patients were included in a prospective, multicenter (4 US centers using 4 different systems) and two-arms clinical trial, including a CNN training on >2.5 million SRS images. In details, for each patient, a fresh tumor specimen was collected, immediately split into sister samples, and randomly assigned to the control or experimental arm. The diagnostic accuracy of pathologists examining conventional H&E images from frozen sections (control arm) and SRS-based images directly obtained in the operating room on fresh and untreated sample and automatically classified by CNN, were compared. Overall diagnostic accuracy

1 was 93.9% for the standard H&E histology arm and 94.6% for the SRS+CNN arm, confirming the efficacy of the
2 approach considering both accuracy and timing criteria.

3 This study strikingly demonstrates how the information obtained by vibrational microscopy not only makes it
4 possible to reach the same (or even higher) diagnostic accuracy of standard human-based approaches, but also
5 drastically reduces time and practical pitfalls typically associated to sample preparation and visual examination.
6 This study also shows that moving to the clinics almost mandatorily requires the robust implementation of
7 artificial intelligence tools, the use of systems in compliance with the clinical workflow and rules, and rigorous
8 tests on large cohorts of patients.

9
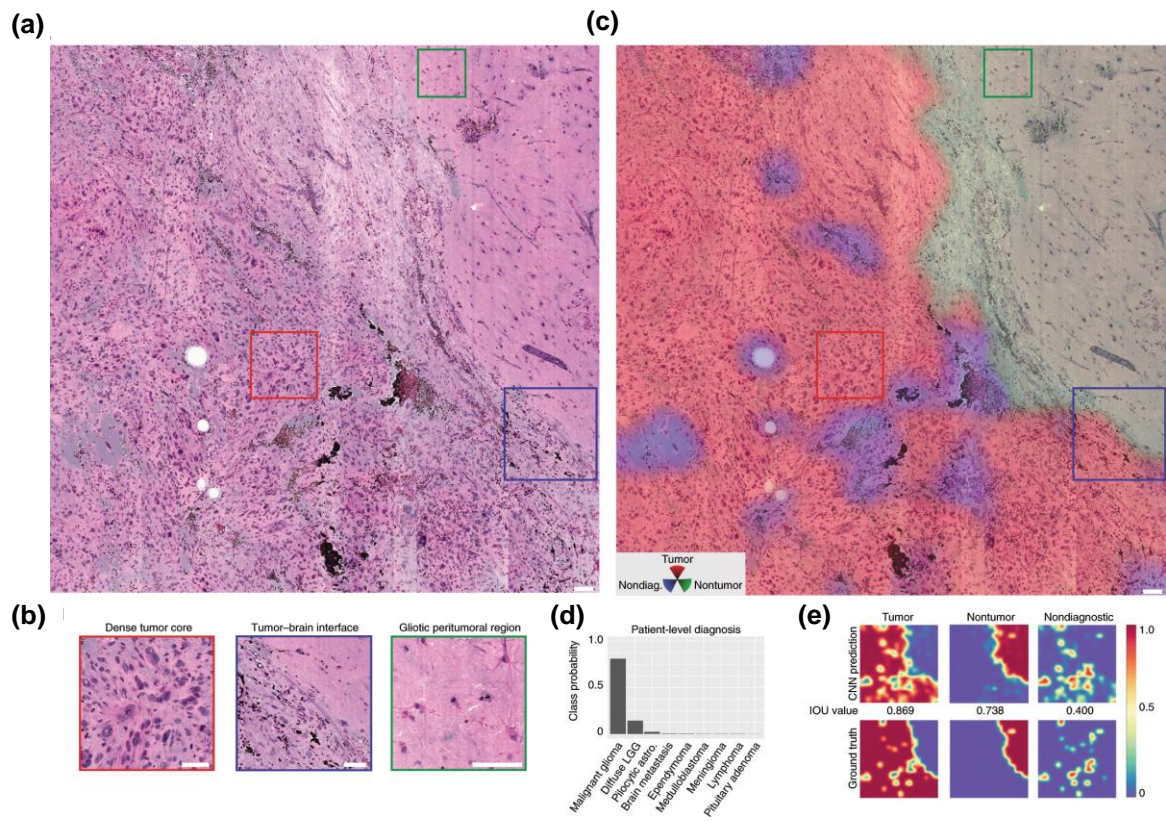
10

11

12 **Fig 38** SRS-based histology (SRH) for the identification of tumour-infiltrated and diagnostic regions. **a** Full SRH mosaic of a
13 specimen collected at the brain–tumor interface of a patient diagnosed with glioblastoma. **b** zoomed regions on the ROIs
14 defined in (**a**). **b** zoomed regions on the ROIs defined in (**a**). **c** Three-channel CNN-based diagnostic prediction overlaid on
15 SRH image (Tumour (red), nontumour (green), nondiagnostic (blu)). **d** patient-level diagnostic class probabilities. **e** class
16 probability heatmaps for tumor, nontumor and nondiagnostic regions within the SRH image are shown with ground truth
17 segmentation. Scale bar: 50 μm. Adapted with permission from [206].

18

19 Before to conclude this part related to CRS-based imaging approaches for cancer diagnosis, we would briefly
20 summarize the current early results and potentialities related to broadband SRS and CARS microscopy
21 approaches. As described in Section 2, and as reviewed in details in or recent review article [52], in the past 15

years several technological solutions have been proposed to extend the detection range from single frequencies to large spectral ranges, still maintaining high imaging speed. In this context, to the best of our knowledge, no broadband CRS studies have been yet applied to cancer assessment on human samples, but a few studies applied these new approaches for testing imaging performances on animal model tissues or for the study of neurodegeneration in human brain [61,77,207]. In particular, Cicerone and collaborators demonstrated the potentialities of a broadband CARS approach by studying fresh or frozen murine tissue samples to probe the entire biologically relevant spectral window (500-3000 cm^{-1}) with 10 cm^{-1} spectral resolution and 3.5 ms pixel dwell time (i.e. a few minutes per mm^2) [61] (**Fig. 39**). We believe that these preliminary results, and a relevant number of emerging technologies aiming to improve broadband CRS approaches for tissue imagine, will soon demonstrate significant advantages in the applied field of vibrational histopathology.
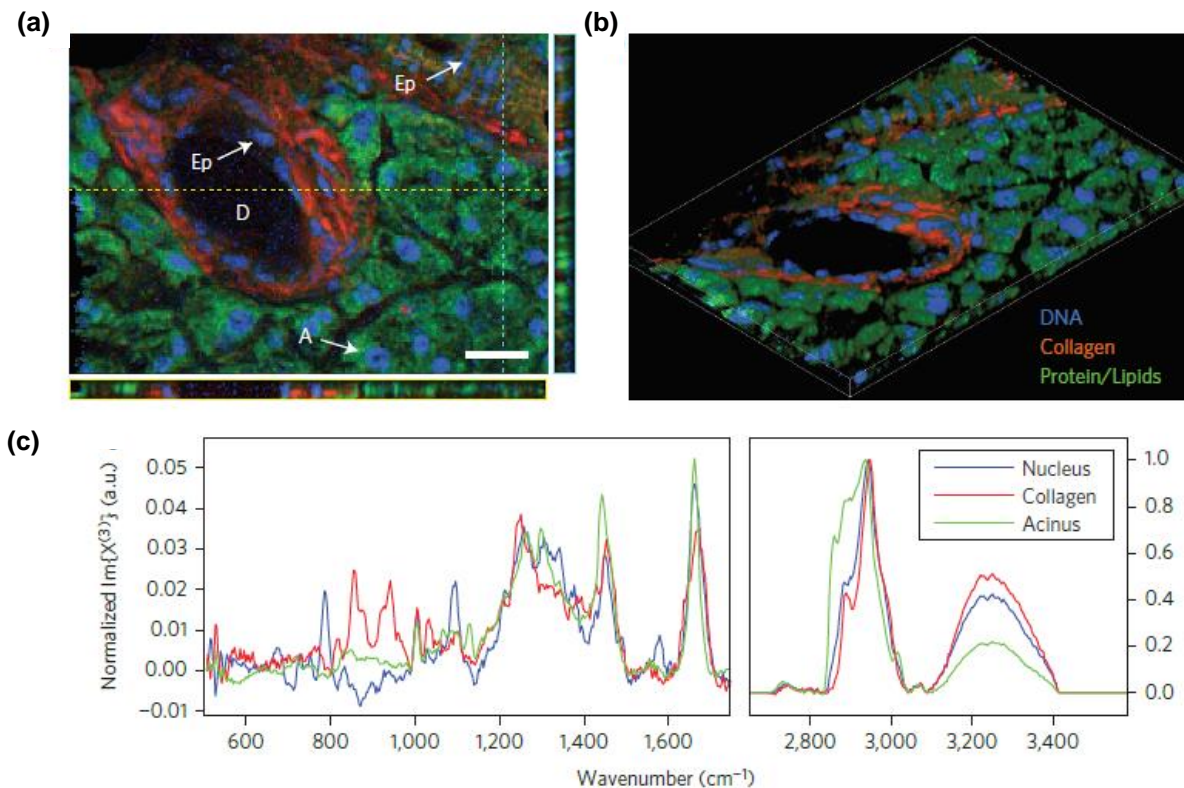
Fig. 39 Coherent Raman fingerprint imaging on biological tissues. **a** false colour map of murine pancreatic ducts showing nuclei (785 cm^{-1}, blue), collagen (855 cm^{-1}, red) and organic matrix (mainly proteins and lipids, 1666 cm^{-1}, green). D, exocrine duct; A, acinar cell; Ep, epithelial cell. **b** 3D reconstruction from the same tissue region, obtained by Z-stack images. **c** spectra obtained from single pixel obtained within specific tissue regions. Scale bar: 20 µm. Adapted with permission from [61].
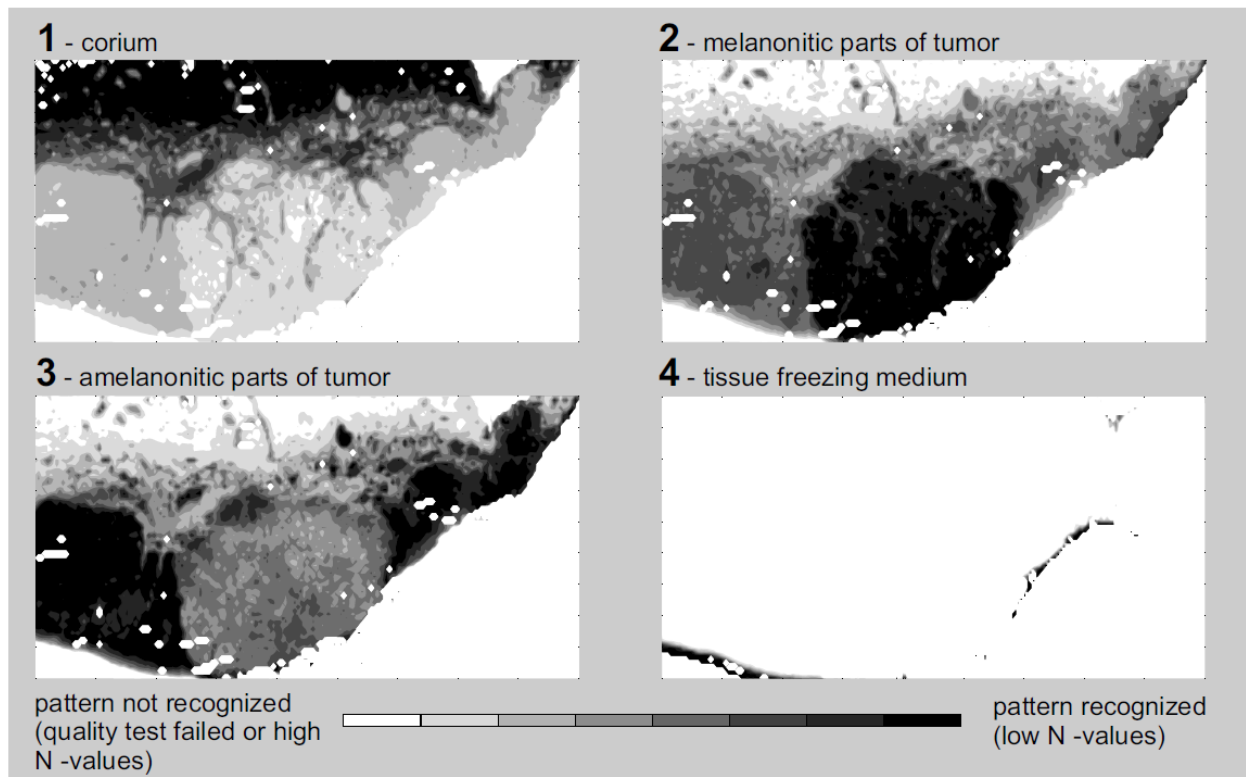
3.3 Infrared imaging

The relatively simple configuration and accessibility of commercial FT-IR spectrometers, and a significantly higher signal to noise ratio if compared with SR spectrometers, combined with the numerous practical advantages of vibrational spectroscopy (label-free and non-destructive), made IR spectroscopy a very powerful tool for the biochemical characterization of biomolecules in the 20th century. The use of IR spectroscopy for the study of cancer tissue samples was first attempted in 1949 [208,209] and was then followed by thousands of papers between the 50's and the 90's aiming to explore the vibrational features of biomolecules, as extensively summarized by several review papers and books [210–213].

Even considering the huge amount of knowledge about the biochemical characteristics of various samples and molecules obtained with IR spectroscopy, the identification and classification of cancerous disease has been made more reliable with the introduction of the imaging modality, as also occurred for Raman-based approaches. As mentioned in the introduction to this section, this is due to the intrinsic spatial heterogeneity of tumor lesions and to the fact that diagnostic decisions, especially related to cancer, are to this day based on the examination of tissue morphology at microscopic level.

A step forward in the field of hyperspectral IR imaging for cancer assessment has been triggered by the introduction in the 1980s of FT-IR spectrometers, which allow the collection of high quality spectra in a relatively short time, and further supported by technological advances, such as sensitive detectors, chemometric approaches and faster computers. For a review, see e.g. [214]. In parallel, P. Lasch and D. Naumann reported in 1998 the first high-resolution FT-IR images of tumor tissue [215] using a commercial FT-IR microscope coupled with a software-controlled xy stage for point-mapping raster-scanning experiments with 80 µm step-size and a nominal spectral resolution of 6 cm^{-1}. Melanoma and colon cancer frozen samples were used for these preliminary FT-IR imaging experiments and, in addition to standard "chemical maps" produced by simply integrating a single wavelength (related to a specific chemical component), the authors introduced for the first time the use of cluster analysis, PCA and artificial neural networks (ANN) to produce false-colour IR-images (**Fig. 40**).

1 - corium

2 - melanonitic parts of tumor

3 - amelanonitic parts of tumor

4 - tissue freezing medium

pattern not recognized (quality test failed or high N -values)

pattern recognized (low N -values)

1

Fig. 40 Early FT-IR images on human melanoma thin sections. Four different images were obtained by the scaled spatial distribution of four different spectral patterns (1-4), previously identified as reference spectra. Adapted with permission from [215].

A further revolution in the field of FT-IR imaging was made in the same period by the introduction of FPA detectors by I.W. Levin and collaborators (Bethesda, USA), [123,216], accompanied by early FT-IR imaging applications for the detection of silicon inclusions in breast samples [217]. FPAs coupled with an interferometer for FT detection enabled highly spatially resolved images (up to the diffraction limit) of large field of views (hundreds of μm^2) with acquisition times comparable to those required for the acquisition of a spectrum at a single point using single-element detectors. For example, Fabian and colleagues performed FT-IR images of breast cancer tissue slices showing that FPA-based instruments provide 4096 single pixel spectra in 5 min versus 256 point spectra in around 4 hours when using a single-element detector [218].

To move FT-IR imaging closer to clinical diagnostics, validation on a relevant number of samples associated with rigorous clinical evaluations was a priority. In this context, the first efforts consisted in the study of 26 colorectal cancer samples resulting in promising accuracy performances (i.e., 95%) but still using single point spectral acquisitions [219]. In this modality, high-quality false colour images were produced and shown as proof-of-concept but not utilized to validate FT-IR imaging on relevant patient cohorts.

In 2005, R. Bhargava, I.W. Levin and collaborators applied FT-IR imaging to histopathology by analysing tissue microarrays (TMAs), i.e. samples containing up to 96 tissue cores of around 0.6 mm in diameter, examining, overall, 262 prostatic samples (i.e. tissue cores of around 0.6 mm diameter) from 40 patients (**Fig. 41**) [122]. All samples were archival, FFPE samples collected during years and just treated for paraffin removal, demonstrating the compatibility with standard routine diagnostic samples. This high-throughput FT-IR imaging strategy produced ~3 million spectra with spatial resolution of 6.25μm and an acquisition time for each tissue core of approximatively 40 min. An initial univariate analysis (**Fig. 41**a) showed tissue differences but was not enough to distinguish all histologic features; as a next step, ten typical histologic classes (normal epithelium, fibrous stroma, mixed stroma, muscle, nerve, lymphocytes, stone, ganglion, endothelium and blood) (**Fig. 41**b) were defined and further used for pattern recognition and subsequent automatic histopathologic characterization. After training the classification model using 86 samples from 16 patients, probability maps were created for each histologic class for all samples, achieving an accuracy between 90 and 99% for each class. A global validation was then applied to individual samples and patients, aiming to distinguish benign versus cancer features obtaining very good diagnostic performances, with an area under the curve (AUC) for the receiver operating characteristics (ROC) curves greater than ≈0.99.
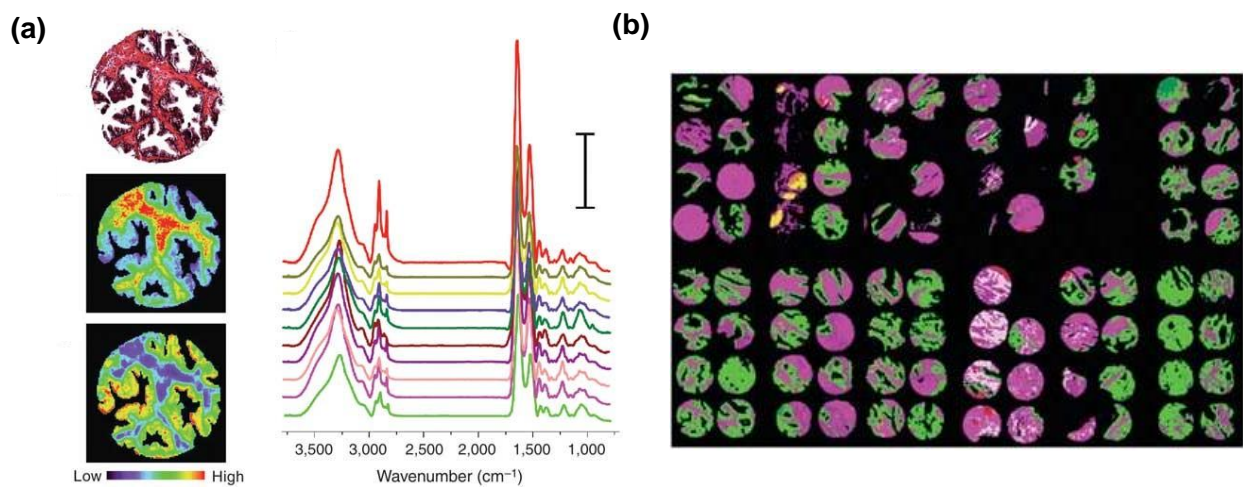
Fig. 41 FT-IR imaging and spectral features of prostate tissue. **a** H&E-stained biopsy section of human prostate tissue (top left) accompanied by FT-IR images reporting protein (middl) and phosphodiester (bottom) concentrations from infrared spectral absorbance at 1,545 cm^{-1} and 1,080 cm^{-1}, respectively. Characteristic infrared absorbance spectra of ten histologic classes comprising prostate tissue are (from bottom to top) from normal epithelium, fibrous stroma, mixed stroma, muscle, nerve, lymphocytes, stone, ganglion, endothelium and blood, are reported in the right panel. The bar indicates an absorbance of 0.2 absorbance units. **b** Example of high-throughput label-free FT-IR based automated and objective tissue classification. The image shows a section of microarray containing different samples (i.e. tissue cores of around 0.6 mm diameter) from different patients. Different colours represent different histological classes (showed in **a**). Adapted with permission from [122].

Leveraging the great improvements associated to FPA-based detectors, also other groups in Europe started to apply FT-IR imaging to cancer studies. Krafft and collaborators (Jena, Germany) used FT-IR to distinguish cervical carcinoma margins exploring the advantages and complementarities of different clustering approaches, namely, fuzzy C-means clustering and hierarchical cluster analysis [220]. A single tissue sample from a patient with squamous cell carcinoma was examined by collecting around 500000 spectra covering an overall area of 8.7 mm^2.

1   While a real diagnostic approach (i.e. by comparing normal vs. tumour samples) was not proposed, this study
2   reported the use of clustering approaches to describe in detail the spectral features of the complex histological
3   architecture that might be found in cancer samples.

4   In parallel to the increase of applications of FT-IR in the field of cancer diagnostics, new technological
5   improvements were introduced, including the use of attenuated total reflection (ATR)-based sampling modes
6   [221], as better detailed in **Section 2.3**. Briefly, compared to the more common transmission modality, the ATR
7   mode differs in that the IR beam does not pass through the sample, but undergoes total internal reflection within
8   an optical element with high refractive index (e.g., diamond, germanium, or silicon), thus allowing higher spatial
9   resolution (below 2 μm) if compared with a resolution limited to ≈5 μm for standard transmission-mode
10   instruments. Bhargava and collaborators compared the ATR and transmission modalities by studying breast
11   tissue samples, including malignant tumours [222]. As a result, the increased spatial resolution allowed by the
12   ATR sampling modality enabled the identification of specific cancer-related structures and cell subtypes relevant
13   for breast cancer diagnosis. Even if this approach has some drawbacks, including that the ATR element needs to
14   make contact with the sample and a limited sample area, it is a promising solution to complement standard FT-
15   IR systems when higher spatial resolution is required.

16   With similar aims, Stone and collaborators have taken advantage of the optical improvements of bench top FPA-
17   based instruments allowing an effective pixel size of 1.1x1.1 μm^2 instead of the typical 5.5 x 5.5 μm^2
18   configuration, thus passing from a "pixel-limited " to a "diffraction-limited" configuration [126]. This, coupled
19   with oversampling and with multi-wavelength image analysis, permitted to identify typical cellular features of
20   colon tissue that were not previously detected by conventional FT-IR configurations [102,126]. To demonstrate
21   this improvement, **Fig. 42** compares three images of a sample of colon tissue, acquired by an optical microscope
22   and two FT-IR microscopes with conventional and high-resolution imaging modalities.

23

24
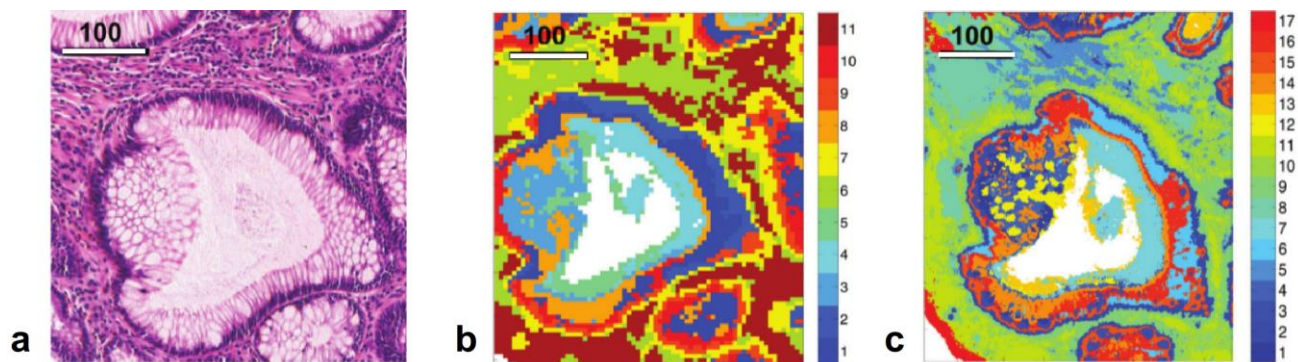
25   **Fig. 42** microscope images of the same colon tissue (with tubular adenoma), acquired with different techniques. (a) Optical
26   transmission image in the visible spectral range of the tissue, after H&E sample staining; (b-c) hyperspectral IR absorption
27   images; false colours are the clusters identified by cluster analysis on the measured hypercubes. (b) conventional imaging
28   set up with 5.5 × 5.5 μm^2 pixel-size, grouped into 11 spectral clusters; (c) high-resolution image by the optical high-
29   magnification scheme, corresponding to 1.1 × 1.1 μm^2 pixel size, and segmented into 17 spectral clusters. Adapted with
30   permission from [126].

31

32   In 2014, Goormaghtigh and collaborators used FT-IR imaging to investigate breast cancer features [223]. The
33   added value of this study is the detailed characterization of tissue components of breast tumour samples, also

thanks to the comparison of spectral data originating from independent samples, not associated with breast and tumours, aiming to determine cancer-related features of cellular or extracellular components contained in or surrounding tumour samples. In details, authors reported that lymphocytes infiltrations observed in invasive breast cancer are (spectroscopically) different from lymphocytes isolated from other organs (such as lymph nodes and tonsils). Similarly, tumour associated stroma (i.e. the extracellular component of tumour, mainly composed by collagen) showed spectral features different from collagen-containing tissue characterizing new and old healed scar tissue (typically rich in collagen). This information is far from being obvious and suggests that vibrational features of some components observed in tumour specimens (e.g. cancer-related immune cells infiltration and cancer-related stroma) differ from the same components observed outside the tumour (i.e. in healthy or non-tumour tissues). In other words, this suggests that the vibrational features observed in tumour tissue may show tumour-specific rather than organ-specific signatures.

The most recent frontier in the field of IR imaging has been approached with the introduction of IR QCLs [224]. As detailed in **Section 2.3**, QCLs are broadly tuneable and bright light sources enabling the use of large size uncooled FPA detectors. Among the first studies introducing QCL imaging of tissue samples for biomedical purposes, P. Gardner and collaborators used a commercial QCL-based microscope measuring absorption at discrete relevant frequencies (i.e. "multispectral imaging"), demonstrating the possibility to image a TMA of around 2 x 2 cm^2 size in less than 10 minutes at a single frequency [225]. In this multispectral modality, QCL systems showed to be much faster (>100 times) than standard FT-IR systems, which measure a continuous spectrum in the fingerprint region in around 19 hours. Clearly, accurate description and diagnosis cannot be performed using a single wavelength. In 2017, the Gardner group aimed to verify whether QCL imaging with continuous spectra acquired in the fingerprint region was competitive for high throughput imaging [226] and compatible with diagnostic accuracy, especially considering the impact of coherent sources on spectral quality. A TMA consisting of 207 breast tissue samples, each from a different patient, was imaged by the same commercial microscope mentioned above in the 1000-1800 cm^{-1} region (pixel size of 4.2 μm) by collecting >33 million pixels in around 13 hours. As a result, malignant and non-malignant stroma were discriminated with 93.6% sensitivity and 85.7% specificity considering all spectra. On a patient basis, all malignant samples were correctly identified (100% sensitivity) and non-malignant samples were classified as malignant in 13.3% of patients (86.7% specificity). In terms of acquisition time, these results were obtained in around 13 hours (i.e. ≈4 min per patient sample), which is promising for translation into clinics but still not too far from the acquisition time associated to conventional FT-IR systems (requiring around 19 hours for the same TMA [225]).

As also detailed in **Section 2.3**, Bhargava and collaborators reported improvements in the field of QCL-based IR imaging by developing a home-built discrete frequency confocal IR microscope providing high-definition and rapid spatial scanning, by sequentially acquiring 12 selected frequencies [128] (**Fig. 43**). In parallel to these technological improvements, the authors also exploited the potential of IR-based chemical imaging by characterizing the features of tumour microenvironment (i.e., cellular and extracellular components surrounding tumour cells) and exploiting them for diagnostic purposes. This is remarkable if we consider that the tumour microenvironment can hardly be described and used as diagnostic criterion by the sole H&E examination. First, authors used conventional FT-IR imaging (i.e., with full continuous spectral information) to define 12 histological classes (including 6 classes related to tumour microenvironment) able to describe the complexity of breast tissue. After having optimized and tested the new confocal IR instrument, an entire TMA (1 cm^2) containing 101 tissue cores from 47 patients was then analysed in 8 hours (≈1 working day). According to the authors, this was around 50-fold faster than FT-IR imaging, that would need ≈50 days to obtain similar signal-to-noise ratio and a similar number of spectra. Considering that the standard clinical practice in breast tumour diagnosis (and in several other diseases) is the evaluation of needle biopsy sections (a few millimetres in size), authors tested the new

1 technology by imaging and classifying a full needle biopsy section (around 4x12mm^2) in 3h, reporting the
2 identification of malignant regions previously detected by pathologists on H&E contiguous slides. This study
3 showed that, with the dramatic speed improvement afforded by QCLs, IR imaging has the possibility to come
4 close to diagnostic workflow in clinics.

5
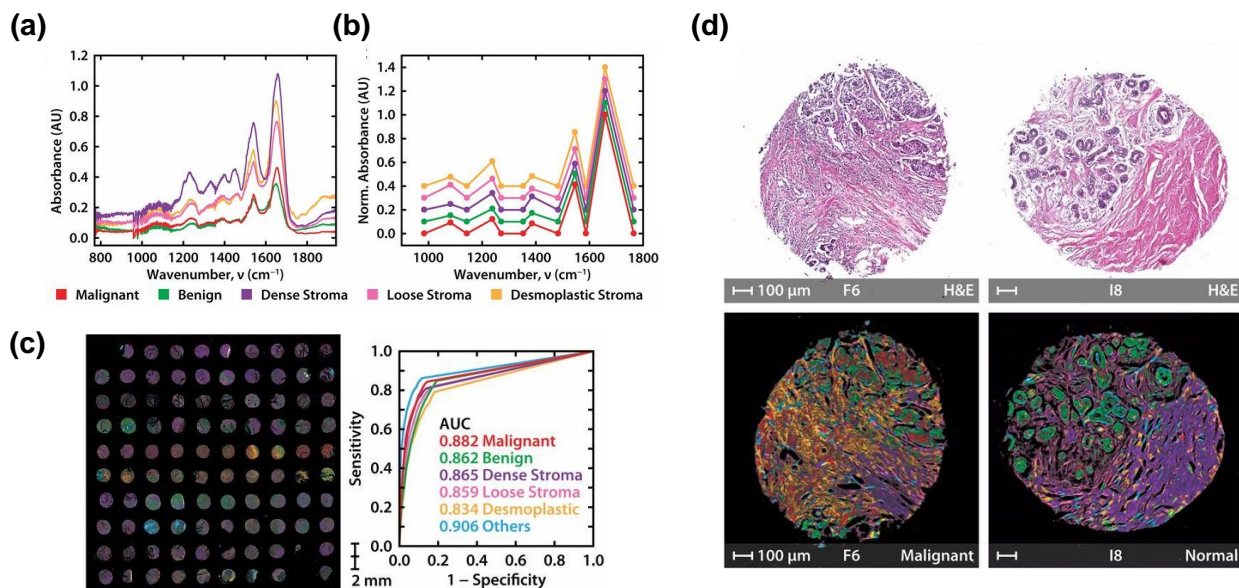
7 **Fig 43** QCL-based confocal infrared microscopy for molecular histopathology on breast tissue samples at discrete
8 frequencies. **a** standard FT-IR spectra from five tissue types (see colour legend) at 1 cm^{-1} spectral resolution. **b** data collected
9 from the same tissue types by the new QCL-based confocal IR approach, at defined discrete frequencies. **c** tissue
10 classification for cancer diagnosis on tissue microarray (left) with ROC curves reporting the accuracy for the identification of
11 six relevant tissue types, including benign and malignant regions. **d** representative examples of malignant (left) and normal
12 (right) tissue samples classified by the IR-based model (bottom), along with H&E stained images (top). Adapted from [128]
13 (CC BY-NC-ND 4.0).

14

15 Simultaneously to Bhargava et al., Gerwert and collaborators reported the use of a commercial QCL-based IR
16 microscope (the same used by Gardner and collaborators and previously mentioned, [225,226], but optimized
17 to reduce coherence effects) to study whole thin sections (between 1-2 cm^2) commonly used for clinical
18 diagnosis [127]. In the configuration used for the study, the microscope collected 2x2mm^2 fields of view in 47s
19 with 4.2-µm step size and 2 cm^{-1} spectral resolution from 950 to 1800 cm^{-1}, for a total of 850 wavenumbers (**Fig.**
20 **44**). A single FFPE thin slice was measured in between 30 and 60 minutes, depending on size, thus permitting to
21 analyse 120 clinical samples in 100 hours. This study showed that QCL-based microscopes can be >160 times
22 faster than state-of-the-art FT-IR approaches with comparable spatial and spectral resolution. In addition, these
23 were the first results reporting the use of IR-based microscopy to image a relevant amount of tissue samples
24 (>100) in their standard format (i.e., whole microscope slides of a few cm^2), thus overcoming the current
25 limitation of most of vibrational based approaches for cancer diagnosis.
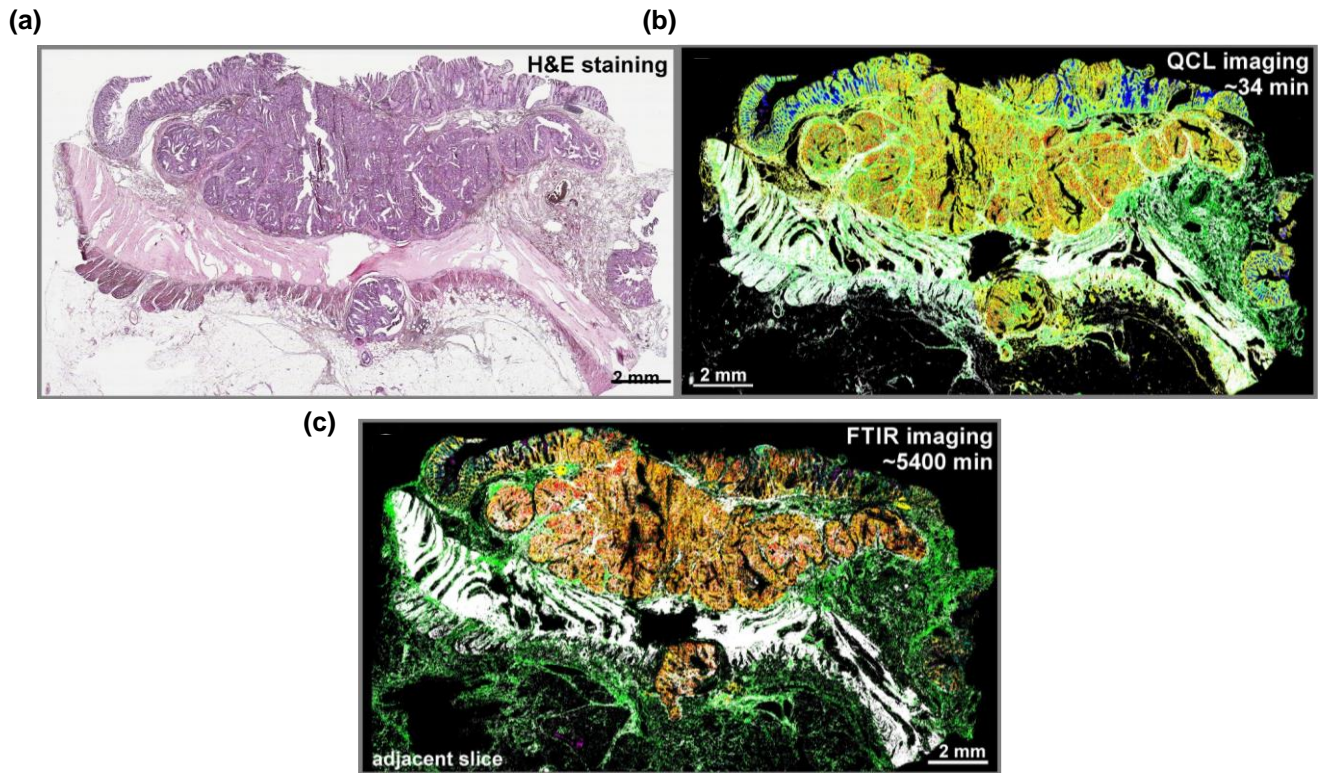
Fig. 44 QCL-based IR histopathology compared with standard FT-IR imaging. **a** H&E-stained slice of colorectal cancer tissue used as reference. **b** QCL-based imaging. **c** FT-IR based imaging. The listed times illustrate the duration of the measurements. Red, pathological region comprising of tumorous regions and infiltrating inflammatory cells; white, muscles; green, connective tissue; cyan, crypts and blue, lumen. Adapted from [127] (CC-BY 4.0).
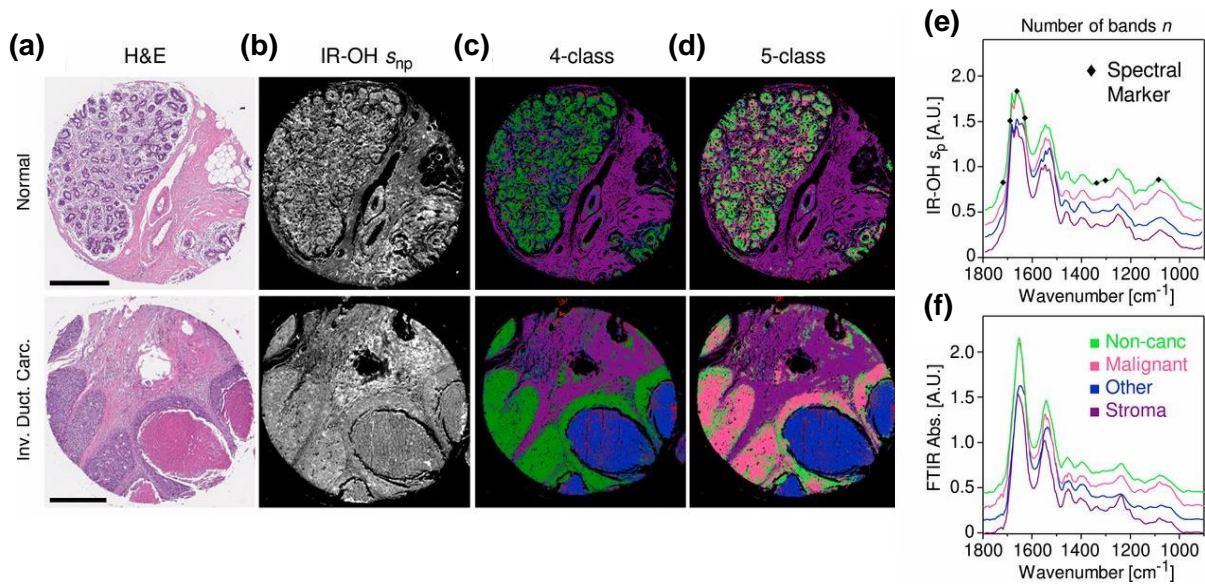
1 **3.4 Photothermal imaging**

2 As described in the previous section, PT-IR is a very recent addition to the portfolio of vibrational techniques for
3 biomedical imaging and it has great potential for applications, considering both the study of cells and tissue,
4 including cancer diagnosis. The use of visible probes to record IR absorption spectra, which is at the basis of
5 modern PT-IR approaches, competes with both Raman and IR imaging tools, complementing the limitations of
6 both. In detail, PT-IR combines the high spatial resolution, usually guaranteed by Raman approaches based on
7 visible excitation sources, with the vibrational sensitivity (and associated acquisition speed) afforded by IR
8 approaches. Moreover, if compared with most CRS tools that are optimized for the imaging speed, PT-IR can
9 easily detect a broader range of vibrational features (i.e., at least the fingerprint region) which nowadays can be
10 reached only by recently proposed broadband CRS approaches, still associated with technological challenges
11 [52]. Furthermore, while water absorption in the IR significantly hampers the use of IR-based tools for the study
12 of living or fresh biological samples (due to the aqueous environment), its large thermal capacity reduces water-
13 induced index changes (and spectral interferences) that may overwhelm the photothermal signal of interest.

14 All mentioned advantages stand at the basis of recent proposed applications and proof of concept studies in the
15 biomedical field. High resolution photothermal imaging of living cells was first demonstrated in 2007, but this
16 was based on the detection of electronic transitions of specific components (mitochondria) thus reducing its
17 applicability for the detection of the biological complexity of disease, including cancer [139]. In parallel, first
18 proof-of-concepts experiments on tissue samples were reported by Mërtiri *et al.* in frozen brain slices but these
19 were based on the use of a mid-infrared pump – near-infrared probe photothermal microscope with intrinsically
20 low spatial resolution [227].
21 A relevant advance in the field has been reported in 2016 by Cheng and collaborators, who applied a home-made
22 PT-IR microscope for the study of living cells and nematodes, combining the rich chemical information afforded
23 by vibrational excitation in the IR with the diffraction-limited spatial resolution of the visible range [145]. After
24 proving the possibility to study single living cells and showing the detection of single lipid droplets and drug
25 molecules in cultured cancer cells, with sub-micrometer resolution, the authors applied the new microscope to
26 *C. elegans*, a millimeter size nematode. The possibility to detect distinct biochemical features (i.e. lipid and
27 proteins, at 1750 and 1655 cm^{-1}, respectively) over a relative large area with high spatial resolution and in a
28 reasonable time (i.e., 500 µs pixel dwell time) indicated compatibility of the method with the study of tissue
29 samples for diagnostic purposes. Following that pioneering result, some recent works reported the application
30 of PT-IR microscopy to the study of fixed and living cells [146,151,153,155,228], most likely because cell studies
31 are those for which the improved spatial resolution and water compatibility better emphasizes the added value
32 of this new imaging technique, especially if compared with standard FT-IR imaging approaches.
33 Up to now, very few PT-IR microscopy studies have been focused on tissue samples. With the exception of a few
34 proof-of-concept studies [227,229,230], only the group of Bhargava reported results in this direction, but with
35 very encouraging perspectives. Bhargava and collaborators proposed the so-called "IR-optical hybrid (IR-OH)
36 approach", detecting IR absorption-induced thermo-mechanical expansion of the sample by a wide-field
37 interferometric photothermal configuration [154]. This configuration permits to combine high spatial resolution
38 and good signal-to-noise ratio with large fields of view (i.e. higher acquisition speed), thus being compatible with
39 histopathologic imaging. In details, the new microscope allows a 10-fold larger area if compared with standard
40 FT-IR imaging (460 x 460 µm^2 *vs* 140 x 140 µm^2) and smaller pixel size (0.32 µm^2 *vs* 1.1 µm^2). The new microscope
41 was applied to the study of breast tissues, with histologic cellular identification and cancer diagnosis using a TMA
42 of around 4 cm^2 consisting of a total of 101 cores (i.e. samples) from 47 patients (**Fig. 45**). Then, 22 discrete IR
43 frequencies were selected and used for the classification of malignant and non-cancerous subtypes. Considering
44 10 seconds per field of view (tile) for each frequency, a single tissue core of around 1mm^2 was imaged in 1.7h

1 and the entire TMA in 168h (7 days), equal to 24min/mm^2. Authors also showed that 7 discrete frequencies
2 saturate the diagnostic performances at around 90% accuracy. In this configuration the acquisition time was
3 reduced to less than 1h per sample and around 2.5 days for the entire array (9 min/mm^2).
4 These results represent the current state of the art in PT-IR microscopy for cancer assessment. Currently, the
5 acquisition speed is significantly lower than in IR microscopy which, using QCL-based microscopes, is able to
6 scan more than 1 cm^2 in around 30 minutes, even if at a significantly lower spatial resolution [127]. Therefore, a
7 clear trade-off emerges between spatial resolution and acquisition speed, which may lead to the choice of PT-IR
8 or IR as imaging technique. Further investigations will be required to determine whether the increased spatial
9 resolution afforded by PT-IR justifies the increase in acquisition time for the application to histopathology.

10

11 **Fig. 45** Photothermal-based IR-optical imaging of breast tissue for the assessment of cancer. **a** H&E-stained slice of
12 normal and cancer (invasive ductal carcinoma). **b** IR-OH adsorption of adjacent sections at 1550 cm^{-1}. **c** four-class model
13 (blood, epithelium, stroma, and other) classification based on five IR bands. **d** Epithelial classification (five-class model) for
14 histologic cellular identification and recognition of cancer based on seven IR bands. **e,g** Representative class spectra
15 obtained with IR-OH (with spectral marker reported on specific bands) and FT-IR, respectively. **g.** Adapted with permission
16 from [154].

17

18

19

20

21

22

4. Conclusion and perspectives

As emerging from the literature presented in the previous sections, in the last forty years exceptional efforts have been invested to make possible the assessment of cancer on tissue samples using the intrinsic chemical information revealed by label-free vibrational microscopies. Starting from pioneering Raman-based to IR-based methods and going through the introduction of more recent technological evolutions of such approaches, including coherent Raman microscopies, QCL-based infrared imaging and photothermal imaging, we have seen a constant improvement of imaging and diagnostic performances.

As illustrated in **Figure 46**, three parameters are fundamental to evaluate vibrational imaging performances in the biomedical context: spectral information, imaging speed, and spatial resolution of the image. An ideal label-free imaging tool for histopathology should provide highly specific and highly informative data, at diffraction limited resolution, and requiring less than the time taken today in the clinical practice for the preparation, staining and observation of tissue samples with up to a few cm^2 area (i.e. between 20 to 40 minutes for intraoperative assessment, between 24 to 48h for biopsy routine diagnosis assessment, considering tissue fixation and embedding). The methods reported in literature to date commonly show good or exceptional performances for only one or two of the above-mentioned requirements and, most of the time, one parameter might need to be sacrificed to promote the others. For example, SR is the approach that currently better combines high spectral information and high spatial resolution, but it is intrinsically limited by low imaging speed, and the acquisition of images of tissue samples of some mm^2 may require days. This is the reason why the best exploitation of SR approaches for image-based cancer diagnosis is the detailed characterization of relatively small (pre-selected) tissue portions or the discovery of disease-related spectral features to be further detected with faster approaches. Similarly, FT-IR microscopy is also highly informative and generally faster than SR but the spatial resolution is intrinsically limited by the long IR wavelengths. Nevertheless, also FT-IR-based approaches take many hours to produce false-colors images of tissue samples and are still far from the above-mentioned ideal performances. In this context, QCL-based IR microscopy greatly improved imaging speed, up to 30 min/cm^2 thus beginning to become competitive with standard histological protocols. At the same time, current QCL-IR approaches, still based on IR sources, are limited by a few µm lateral resolution and by the interference of water bands, preventing intraoperative cancer assessment of fresh frozen samples. For what concerns spectral information, the studies reported so far reach a coverage of $\approx$900 cm^{-1}, but recent development of QCL sources is going to permit wider spectral windows for histological applications.

Coming back to Raman approaches, SRS and CARS imaging microscopes, employing narrowband (i.e. single frequency) detection, perform very well in combining high imaging speed and imaging resolution. Such approaches, especially SRS-based ones, can go below 1µs pixel dwell time (i.e., a few minutes per mm^2), close to diffraction limited resolution (i.e., 0.5 to 1.5 µm), while still being fully compatible with fresh (or frozen) samples without any sample preparation (or fixation) treatment (**Fig. 46**). On the other hand, narrowband SRS/CARS methods are intrinsically limited to the detection of single wavenumbers (usually two bands, and usually in the CH region) thus greatly restricting the biomolecular specificity of vibrational-based approaches. Consequently, as reported in the previous section, recent successful approaches reaching clinical studies have used the spectral information "only" to produce very accurate false color "virtual histopathology" images to be further processed as images, and not as hyperspectral data, using AI approaches like those used for digital pathology. Even if this methodology is very intriguing and the obtained images are well accepted by clinicians, the potential of using the entire (or large part) of spectral and biomolecular information (i.e. "spectral histopathology") can be even more promising considering the amount of objective information that can be collected and used for tissue classification. In this direction broadband CARS/SRS imaging tools may be a favorable approach to combine

1 imaging speed, spectral information, and high spatial resolution. The price here, at least in this early stage of
2 development, is the technological complexity and the need of demanding data processing steps to retrieve
3 accurate spectral features. Finally, in the previous section we also introduced PT-IR microscopy, which represents
4 the most recent tool potentially able to answer current needs, by coupling IR-based excitation sources with
5 visible detection, thus guaranteeing advantages of both Raman and IR approaches, still being compatible with
6 water-containing samples. Application results are still to be evaluated, especially in the field of histopathology,
7 but potentialities are clear and will probably be soon demonstrated in upcoming studies.

8
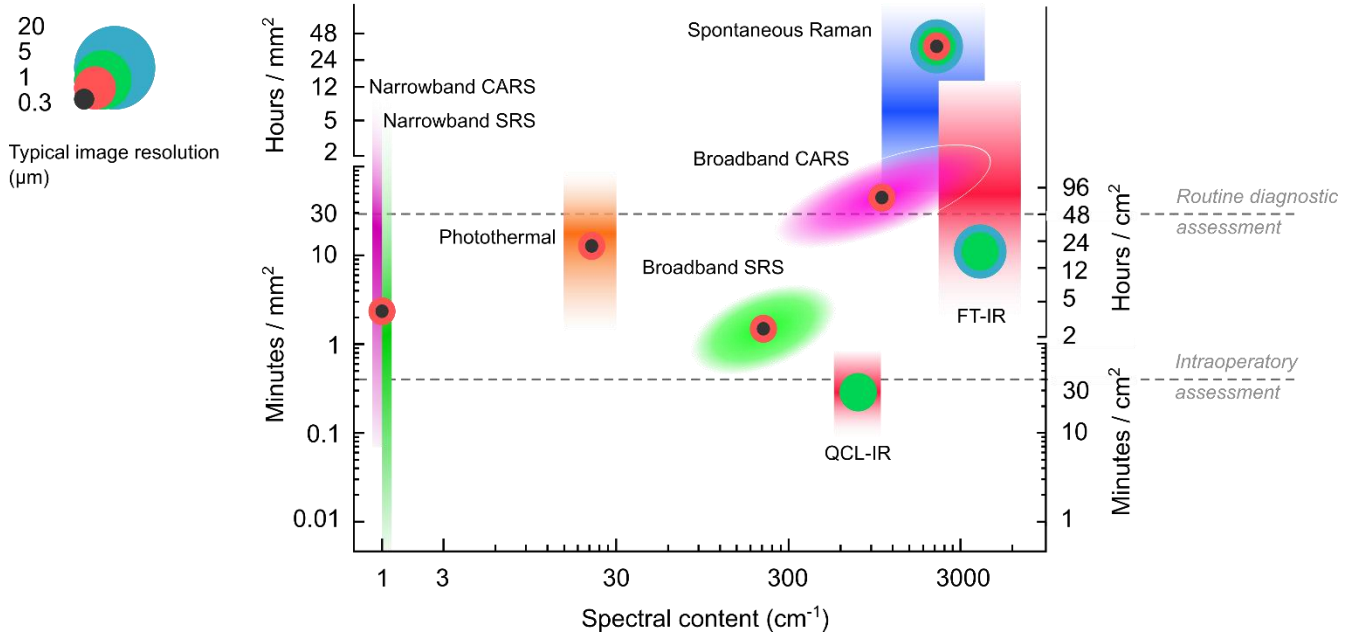
10 **Fig 46** Vibrational imaging performances of different approaches applied to cancer detection. Vertical axes indicate the time
11 (minutes and hours, lower and upper sections, respectively) required to image area units (cm^2 and mm^2, left and right,
12 respectively) considering for each approach its common range of image resolution and confined between 0.5 to 20 μm
13 between each pixel. The horizontal axis represents the average spectral window (and not the spectral resolution) covered
14 by each vibrational approach, in standard setting for cancer imaging experiments, reported until now. Two horizontal broken
15 lines approximately indicate the time commonly required to obtain intraoperative assessment of fresh-frozen samples
16 (bottom line) and the time commonly required to obtain a routine diagnostic assessment from FFPE tissue samples (upper
17 line). The coloured circles represent the allowed and most used pixel step-size for each approach. The coloured squares and
18 ovals are representative and averaged performance ranges of imaging approaches used for cancer studies, mainly extracted
19 from following selected studies: spontaneous Raman imaging [162,174,175]; FT-IR imaging [122,126,231]; QCL-IR imaging
20 [127]; Photothermal imaging [154]; narrowband SRS [200,206]; narrowband CARS [197]; broadband SRS [207]; broadband
21 CARS, from our preliminary data and from the available data on cancer tissue (non-human) [61].

22

23 For simplicity, and considering the scope of this review, here we mentioned three main criteria (i.e. imaging
24 speed, spectral information and spatial resolution) to evaluate vibrational imaging approaches, but these
25 aspects, strictly associated to technologies performances, are obviously not enough to understand what is
26 missing to go from optical bench to clinical bedside. For instance, despite the enormous number of publications
27 and patents in this field, the clinical translation of such approaches is still lacking, and this is one of the most

important aims and challenges for the scientific and industrial communities in these days. An increasing interest has emerged on these aspects in the past two decades underlining causes, problems and needs concerning clinical translation, as better detailed in recent documents and focal reviews [232–235]. Among the most urgent needs we want to emphasize the importance of 1) establishing strong engagement between technology providers and clinicians (final users), starting from the early maturation stage of technologies; 2) clearly understand real needs and real constraints, also including those which apparently seem not strictly associated to technological and scientific innovations (and high impact publications), including standard clinical and laboratory procedures, routine workflow, regulatory aspects; 3) prioritize quality control of data, reproducibility and large-scale validation.

At this concern the emerging of multimodal networks, such as "The International Society for Clinical Spectroscopy" (CLIRSPEC) [236] and of "Raman4Clinics" (COST action) [237], permitted to establish the above mentioned interactions between multiple stakeholders and also to organize large-scale cross-laboratory studies [238,239] enabling to improve standardization and to define comparability parameters.

In conclusion, the continuous and dramatic technological progress in label-free vibrational microscopies, coupled to an interdisciplinary effort to overcome barriers between technologists and clinicians and speak a common language, promises to usher a new era in tumor diagnostics and in personalized, precision medicine.

References

1. F. Bray, J. Ferlay, I. Soerjomataram, R. L. Siegel, L. A. Torre, and A. Jemal, CA. Cancer J. Clin. **68**, 394 (2018).

2. S. Srivastava, E. J. Koay, A. D. Borowsky, A. M. De Marzo, S. Ghosh, P. D. Wagner, and B. S. Kramer, Nat. Rev. Cancer **19**, 349 (2019).

3. A. Trinh, K. Trumpi, F. D. S. E. Melo, X. Wang, J. H. de Jong, E. Fessler, P. J. K. Kuppen, M. S. Reimers, M. Swets, M. Koopman, I. D. Nagtegaal, M. Jansen, G. K. J. Hooijer, G. J. A. Offerhaus, O. Kranenburg, C. J. Punt, J. P. Medema, F. Markowetz, and L. Vermeulen, Clin. Cancer Res. **23**, 387 (2017).

4. A. K. Füzéry, J. Levin, M. M. Chan, and D. W. Chan, Clin. Proteomics **10**, 13 (2013).

5. A. El-Naggar, J. Chan, T. Takata, J. Grandis, and P. Blootweg, *WHO Classification of Tumours. Pathology and Genetics of Head and Neck Tumours* (International Agency for Research on Cancer, Lyon, 2017).

6. S. R. Lakhani, *WHO Classification of Tumours of the Breast* (International Agency for Research on Cancer, Lyon, 2012).

7. H. Steven, E. C. Swerdlow, N. L. Harris, E. S. Jaffe, S. A. Pireli, H. Stein, J. Thiele, and J. W. Vardiman, *WHO Classification of Tumours of Haematopoietic and Lymphoid Tissues* (International Agency for Research on Cancer, Lyon, 2008).

8. M. Titford, J. Histotechnol. **32**, 9 (2009).

9. A. Heindl, S. Nawaz, and Y. Yuan, Lab. Invest. **95**, 377 (2015).

10. S. Mukhopadhyay, M. D. Feldman, E. Abels, R. Ashfaq, S. Beltaifa, N. G. Cacciabeve, H. P. Cathro, L. Cheng, K. Cooper, G. E. Dickey, R. M. Gill, R. P. Heaton, R. Kerstens, G. M. Lindberg, R. K. Malhotra, J. W. Mandell, E. D. Manlucu, A. M. Mills, S. E. Mills, C. A. Moskaluk, M. Nelis, D. T. Patil, C. G. Przybycin, J. P. Reynolds, B. P. Rubin, M. H. Saboorian, M. Salicru, M. A. Samols, C. D. Sturgis, K. O. Turner, M. R. Wick, J. Y. Yoon, P. Zhao, and C. R. Taylor, Am. J. Surg. Pathol. **42**, 39 (2018).

11. K. Bera, K. A. Schalper, D. L. Rimm, V. Velcheti, and A. Madabhushi, Nat. Rev. Clin. Oncol. **16**, 703 (2019).

12. H. J. Butler, L. Ashton, B. Bird, G. Cinque, K. Curtis, J. Dorney, K. Esmonde-White, N. J. Fullwood, B. Gardner, P. L. Martin-Hirsch, M. J. Walsh, M. R. McAinsh, N. Stone, and F. L. Martin, Nat. Protoc. **11**, 664 (2016).

13. M. J. Baker, J. Trevisan, P. Bassan, R. Bhargava, H. J. Butler, K. M. Dorling, P. R. Fielden, S. W. Fogarty, N. J. Fullwood, K. A. Heys, C. Hughes, P. Lasch, P. L. Martin-Hirsch, B. Obinaju, G. D. Sockalingum, J. Sulé-Suso, R. J. Strong, M. J. Walsh, B. R. Wood, P. Gardner, and F. L. Martin, Nat. Protoc. **9**, 1771 (2014).

14. C. H. Camp Jr. and M. T. Cicerone, Nat. Photonics **9**, 295 (2015).

15. R. Vanna, P. Ronchi, A. T. M. Lenferink, C. Tresoldi, C. Morasso, D. Mehn, M. Bedoni, S. Picciolini, L. W. M. M. Terstappen, F. Ciceri, C. Otto, and F. Gramatica, The Analyst **140**, 1054 (2015).

16. J. D. Jackson, *Classical Electrodynamics*, Third (Wiley, 1998).

17. C. Krafft, B. Dietzek, J. Popp, and M. Schmitt, J. Biomed. Opt. **17**, 040801 (2012).

18. D. C. Harris and M. D. Bertolucci, *Symmetry and Spectroscopy: An Introduction to Vibrational and Electronic Spectroscopy* (Courier Corporation, 1989).

19. L. Brillouin, Ann. Phys. **9**, 88 (1922).

20. A. Smekal, Naturwissenschaften **11**, 873 (1923).

21. C. V. Raman and K. S. Krishnan, Nature **121**, 501 (1928).

22. T. H. Maiman, Nature **187**, 493 (1960).

23. M. Delhaye and P. Dhamelincourt, J. Raman Spectrosc. **3**, 33 (1975).

24. P. Dhamelincourt, in *Conf Ser Phys* (Philadelphia; Institute of Physics; 1999, 2000), pp. 9–10.

25. C. Krafft, I. W. Schie, T. Meyer, M. Schmitt, and J. Popp, Chem. Soc. Rev. **45**, 1819 (2016).

26. E. Lee, in *Raman Imaging*, edited by A. Zoubir and V. D'Ascq (Springer, 2012), pp. 1–37.

27. G. J. Puppels, F. F. de Mul, C. Otto, J. Greve, M. Robert-Nicoud, D. J. Arndt-Jovin, and T. M. Jovin, Nature **347**, 301 (1990).

28. G. Turrell and J. Corset, *Raman Microscopy: Developments and Applications* (Academic Press, 1996).

29. Y.-S. Huang, T. Karashima, M. Yamamoto, and H. Hamaguchi, J. Raman Spectrosc. **34**, 1 (2003).

30. J. Hutchings, C. Kendall, B. Smith, N. Shepherd, H. Barr, and N. Stone, J. Biophotonics **2**, 91 (2009).

31. M. Okada, N. I. Smith, A. F. Palonpon, H. Endo, S. Kawata, M. Sodeoka, and K. Fujita, Proc. Natl. Acad. Sci. **109**, 28 (2012).

32. K. Watanabe, A. F. Palonpon, N. I. Smith, L. Chiu, A. Kasai, H. Hashimoto, S. Kawata, and K. Fujita, Nat. Commun. **6**, 10095 (2015).

33. S. Stewart, R. J. Priore, M. P. Nelson, and P. J. Treado, Annu Rev Anal Chem **5**, 337 (2012).

34. H. R. Morris, C. C. Hoyt, P. Miller, and P. J. Treado, Appl. Spectrosc. **50**, 805 (1996).

35. P. J. Treado, I. W. Levin, and E. N. Lewis, Appl. Spectrosc. **46**, 1211 (1992).

36. S. Schlücker, M. D. Schaeberle, S. W. Huffman, and I. W. Levin, Anal Chem **75**, 4312 (2003).

37. A. Papour, J. H. Kwak, Z. Taylor, B. Wu, O. Stafsudd, and W. Grundfest, Biomed. Opt. Express **6**, 3892 (2015).

38. S. Yang, B. Li, A. Akkus, O. Akkus, and L. Lang, Analyst **139**, 3107 (2014).

39. A. Zumbusch, G. R. Holtom, and X. S. Xie, Phys. Rev. Lett. **82**, 4142 (1999).

40. C. W. Freudiger, W. Min, B. G. Saar, S. Lu, G. R. Holtom, C. He, J. C. Tsai, J. X. Kang, and X. S. Xie, Science **322**, 1857 (2008).

41. P. Nandakumar, A. Kovalev, and A. Volkmer, New J. Phys. **11**, 033026 (2009).

42. H. Rigneault and P. Berto, APL Photonics **3**, 091101 (2018).

43. J. Cheng, A. Volkmer, L. D. Book, and X. S. Xie, J. Phys. Chem. B **105**, 1277 (2001).

44. B. G. Saar, C. W. Freudiger, J. Reichman, C. M. Stanley, G. R. Holtom, and X. S. Xie, Science **330**, 1368 (2010).

45. E. O. Potma, D. J. Jones, J.-X. Cheng, X. S. Xie, and J. Ye, Opt. Lett. **27**, 1168 (2002).

46. F. Ganikhanov, S. Carrasco, X. S. Xie, M. Katz, W. Seitz, and D. Kopf, Opt. Lett. **31**, 1292 (2006).

47. A. Gambetta, V. Kumar, G. Grancini, D. Polli, R. Ramponi, G. Cerullo, and M. Marangoni, Opt. Lett. **35**, 226 (2010).

48. G. Krauss, T. Hanke, A. Sell, D. Träutlein, A. Leitenstorfer, R. Selm, M. Winterhalder, and A. Zumbusch, Opt. Lett. **34**, 2847 (2009).

49. E. S. Lamb, S. Lefrancois, M. Ji, W. J. Wadsworth, X. S. Xie, and F. W. Wise, Opt. Lett. **38**, 4154 (2013).

50. R. He, Y. Xu, L. Zhang, S. Ma, X. Wang, D. Ye, and M. Ji, Optica **4**, 44 (2017).

51. Y. Suzuki, K. Kobayashi, Y. Wakisaka, D. Deng, S. Tanaka, C.-J. Huang, C. Lei, C.-W. Sun, H. Liu, Y. Fujiwaki, S. Lee, A. Isozaki, Y. Kasai, T. Hayakawa, S. Sakuma, F. Arai, K. Koizumi, H. Tezuka, M. Inaba, K. Hiraki, T. Ito, M. Hase, S. Matsusaka, K. Shiba, K. Suga, M. Nishikawa, M. Jona, Y. Yatomi, Y. Yalikun, Y. Tanaka, T. Sugimura, N. Nitta, K. Goda, and Y. Ozeki, Proc. Natl. Acad. Sci. **116**, 15842 (2019).

52. D. Polli, V. Kumar, C. M. Valensise, M. Marangoni, and G. Cerullo, Laser Photonics Rev. **12**, 1800020 (2018).

53. M. Mohseni, C. Polzer, and T. Hellerer, Opt. Express **26**, 10230 (2018).

54. L. Brückner, T. Buckup, and M. Motzkus, JOSA B **33**, 1482 (2016).

55. J. Cheng, A. Volkmer, L. D. Book, and X. S. Xie, J. Phys. Chem. B **106**, 8493 (2002).

56. H. Kano and H. Hamaguchi, Appl. Phys. Lett. **86**, 121113 (2005).

57. T. W. Kee and M. T. Cicerone, Opt. Lett. **29**, 2701 (2004).

58. M. Müller and J. M. Schins, J. Phys. Chem. B **106**, 3715 (2002).

59. C. Pohling, T. Buckup, A. Pagenstecher, and M. Motzkus, Biomed. Opt. Express **2**, 2110 (2011).

60. B. von Vacano, L. Meyer, and M. Motzkus, J. Raman Spectrosc. **38**, 916 (2007).

61. C. H. Camp, Y. J. Lee, J. M. Heddleston, C. M. Hartshorn, A. R. Hight Walker, J. N. Rich, J. D. Lathia, and M. T. Cicerone, Nat. Photonics **8**, 627 (2014).

62. M. T. Cicerone, K. A. Aamer, Y. J. Lee, and E. Vartiainen, J. Raman Spectrosc. **43**, 637 (2012).

63. S. Ruhman, A. G. Joly, and K. A. Nelson, IEEE J. Quantum Electron. **24**, 460 (1988).

64. B.-C. Chen, J. Sung, X. Wu, and S.-H. Lim, J. Biomed. Opt. **16**, 021112 (2011).

65. E. M. Vartiainen, H. A. Rinia, M. Müller, and M. Bonn, Opt. Express **14**, 3622 (2006).

66. Y. Liu, Y. J. Lee, and M. T. Cicerone, Opt. Lett. **34**, 1363 (2009).

67. R. Houhou, R. Houhou, P. Barman, M. Schmitt, T. Meyer, T. Meyer, J. Popp, J. Popp, T. Bocklitz, and T. Bocklitz, Opt. Express **28**, 21002 (2020).

68. C. M. Valensise, A. Giuseppi, F. Vernuccio, A. De la Cadena, G. Cerullo, and D. Polli, APL Photonics **5**, 061305 (2020).

69. D. Pestov, R. K. Murawski, G. O. Ariunbold, X. Wang, M. Zhi, A. V. Sokolov, V. A. Sautenkov, Y. V. Rostovtsev, A. Dogariu, Y. Huang, and M. O. Scully, Science **316**, 265 (2007).

70. R. Selm, M. Winterhalder, A. Zumbusch, G. Krauss, T. Hanke, A. Sell, and A. Leitenstorfer, Opt. Lett. **35**, 3282 (2010).

71. A. Volkmer, L. D. Book, and X. S. Xie, Appl. Phys. Lett. **80**, 1505 (2002).

72. T. Ideguchi, S. Holzner, B. Bernhardt, G. Guelachvili, N. Picqué, and T. W. Hänsch, Nature **502**, 355 (2013).

73. J. P. Ogilvie, E. Beaurepaire, A. Alexandrou, and M. Joffre, Opt. Lett. **31**, 480 (2006).

74. M. Tamamitsu, Y. Sakaki, T. Nakamura, G. K. Podagatlapalli, T. Ideguchi, and K. Goda, Vib. Spectrosc. **91**, 163 (2017).

75. E. R. Andresen, P. Berto, and H. Rigneault, Opt. Lett. **36**, 2387 (2011).

76. H. T. Beier, G. D. Noojin, and B. A. Rockwell, Opt. Express **19**, 18885 (2011).

77. V. Schweikhard, A. Baral, V. Krishnamachari, W. C. Hay, and M. Fuhrmann, BioRxiv 789248 (2019).

78. Y. Ozeki, W. Umemura, Y. Otsuka, S. Satoh, H. Hashimoto, K. Sumimura, N. Nishizawa, K. Fukui, and K. Itoh, Nat. Photonics **6**, 845 (2012).

79. Y. Ozeki, Y. Kitagawa, K. Sumimura, N. Nishizawa, W. Umemura, S. Kajiyama, K. Fukui, and K. Itoh, Opt. Express **18**, 13708 (2010).

80. Y. Ozeki, W. Umemura, K. Sumimura, N. Nishizawa, K. Fukui, and K. Itoh, Opt. Lett. **37**, 431 (2012).

81. L. Kong, M. Ji, G. R. Holtom, D. Fu, C. W. Freudiger, and X. S. Xie, Opt. Lett. **38**, 145 (2013).

82. B. Liu, H. J. Lee, D. Zhang, C.-S. Liao, N. Ji, Y. Xia, and J.-X. Cheng, Appl. Phys. Lett. **106**, 173704 (2015).

83. D. Huang, E. A. Swanson, C. P. Lin, J. S. Schuman, W. G. Stinson, W. Chang, M. R. Hee, T. Flotte, K. Gregory, C. A. Puliafito, and A. Et, Science **254**, 1178 (1991).

84. C.-S. Liao, K.-C. Huang, W. Hong, A. J. Chen, C. Karanja, P. Wang, G. Eakins, and J.-X. Cheng, Optica **3**, 1377 (2016).

85. R. He, Z. Liu, Y. Xu, W. Huang, H. Ma, and M. Ji, Opt. Lett. **42**, 659 (2017).

86. B. Figueroa, W. Fu, T. Nguyen, K. Shin, B. Manifold, F. Wise, and D. Fu, Biomed. Opt. Express **9**, 6116 (2018).

87. D. Fu, W. Yang, and X. S. Xie, J. Am. Chem. Soc. **139**, 583 (2017).

88. P. Tournois, Opt. Commun. **140**, 245 (1997).

89. F. Verluise, V. Laude, Z. Cheng, C. Spielmann, and P. Tournois, Opt. Lett. **25**, 575 (2000).

90. M. S. Alshaykh, C.-S. Liao, O. E. Sandoval, G. Gitzinger, N. Forget, D. E. Leaird, J.-X. Cheng, and A. M. Weiner, Opt. Lett. **42**, 1548 (2017).

91. X. Audier, N. Forget, and H. Rigneault, Opt. Express **28**, 15505 (2020).

92. D. Fu, F.-K. Lu, X. Zhang, C. Freudiger, D. R. Pernik, G. Holtom, and X. S. Xie, J. Am. Chem. Soc. **134**, 3623 (2012).

93. S. P. Laptenok, V. P. Rajamanickam, L. Genchi, T. Monfort, Y. Lee, I. I. Patel, A. Bertoncini, and C. Liberale, J. Biophotonics **12**, e201900028 (2019).

94. B. R. Bachler, M. E. Fermann, and J. P. Ogilvie, Opt. Express **20**, 835 (2012).

95. C. W. Freudiger, M. B. J. Roeffaers, X. Zhang, B. G. Saar, W. Min, and X. S. Xie, J. Phys. Chem. B **115**, 5574 (2011).

96. W. Rock, M. Bonn, and S. H. Parekh, Opt. Express **21**, 15113 (2013).

97. G. Sciortino, A. Ragni, A. De la Cadena, M. Sampietro, G. Cerullo, D. Polli, and G. Ferrari, IEEE J. Solid-State Circuits **56**, 1859 (2021).

98. K. Seto, Y. Okuda, E. Tokunaga, and T. Kobayashi, Rev. Sci. Instrum. **84**, 083705 (2013).

99. F.-K. Lu, M. Ji, D. Fu, X. Ni, C. W. Freudiger, G. Holtom, and X. S. Xie, Mol. Phys. **110**, 1927 (2012).

100. C.-S. Liao, M. N. Slipchenko, P. Wang, J. Li, S.-Y. Lee, R. A. Oglesbee, and J.-X. Cheng, Light Sci. Appl. **4**, e265 (2015).

101. M. N. Slipchenko, R. A. Oglesbee, D. Zhang, W. Wu, and J.-X. Cheng, J. Biophotonics **5**, 801 (2012).

102. J. Nallala, G. R. Lloyd, M. Hermes, N. Shepherd, and N. Stone, Vib. Spectrosc. **91**, 83 (2017).

103. C. Hughes, G. Clemens, B. Bird, T. Dawson, K. M. Ashton, M. D. Jenkinson, A. Brodbelt, M. Weida, E. Fotheringham, M. Barre, J. Rowlette, and M. J. Baker, Sci. Rep. **6**, 20173 (2016).

104. S. P. Davis, M. C. Abrams, and J. W. Brault, Fourier Transform Spectrom. Sumner P Davis Al San Diego Calif Acad. Press C2001 (2001).

105. M. Z. Kastyak-Ibrahim, M. J. Nasse, M. Rak, C. Hirschmugl, M. R. Del Bigio, B. C. Albensi, and K. M. Gough, NeuroImage **60**, 376 (2012).

106. L. M. Miller and P. Dumas, Biochim. Biophys. Acta BBA - Biomembr. **1758**, 846 (2006).

107. O. J. Old, G. R. Lloyd, J. Nallala, M. Isabelle, L. M. Almond, N. A. Shepherd, C. A. Kendall, A. C. Shore, H. Barr, and N. Stone, The Analyst **142**, 1227 (2017).

108. D. Perez-Guaita, K. Kochan, M. Martin, D. W. Andrew, P. Heraud, J. S. Richards, and B. R. Wood, Vib. Spectrosc. **91**, 46 (2017).

109. A. B. Seddon, Phys. Status Solidi B **250**, 1020 (2013).

110. E. Levenson, P. Lerch, and M. C. Martin, Infrared Phys. Technol. **49**, 45 (2006).

111. C. Petibois, M. Cestelli-Guidi, M. Piccinini, M. Moenner, and A. Marcelli, Anal. Bioanal. Chem. **397**, 2123 (2010).

112. I. Amenabar, S. Poly, M. Goikoetxea, W. Nuansing, P. Lasch, and R. Hillenbrand, Nat. Commun. **8**, 14402 (2017).

113. J. Faist, F. Capasso, D. L. Sivco, C. Sirtori, A. L. Hutchinson, and A. Y. Cho, Science **264**, 553 (1994).

114. C. Petibois, G. Déléris, M. Piccinini, M. Cestelli-Guidi, and A. Marcelli, Nat. Photonics **3**, 179 (2009).

115. T. Steinle, F. Neubrech, A. Steinmann, X. Yin, and H. Giessen, Opt. Express **23**, 11105 (2015).

116. M. J. Nasse, M. J. Walsh, E. C. Mattson, R. Reininger, A. Kajdacsy-Balla, V. Macias, R. Bhargava, and C. J. Hirschmugl, Nat. Methods **8**, 413 (2011).

117. S. Slivken, N. Bandyopadhyay, Y. Bai, Q. Y. Lu, and M. Razeghi, Appl. Phys. Lett. **103**, 231110 (2013).

118. P. B. Fellgett, JOSA **39**, 970 (1949).

119. P. Jacquinot, Rep. Prog. Phys. **23**, 267 (1960).

120. B. C. Smith, Routledge CRC Press (2011).

121. F. Siebert and P. Hildebrandt, *Vibrational Spectroscopy in Life Science* (John Wiley & Sons, 2008).

122. D. C. Fernandez, R. Bhargava, S. M. Hewitt, and I. W. Levin, Nat. Biotechnol. **23**, 469 (2005).

123. E. Neil. Lewis, P. J. Treado, R. C. Reeder, G. M. Story, A. E. Dowrey, Curtis. Marcott, and I. W. Levin, Anal. Chem. **67**, 3377 (1995).

124. P. Garidel and M. Boese, Microsc. Res. Tech. **70**, 336 (2007).

125. P. Dumas, N. Jamin, J. L. Teillaud, L. M. Miller, and B. Beccard, Faraday Discuss. **126**, 289 (2004).

126. J. Nallala, G. R. Lloyd, N. Shepherd, and N. Stone, Analyst **141**, 630 (2016).

127. C. Kuepper, A. Kallenbach-Thieltges, H. Juette, A. Tannapfel, F. Großerueschkamp, and K. Gerwert, Sci. Rep. **8**, 7717 (2018).

128. S. Mittal, K. Yeh, L. S. Leslie, S. Kenkel, A. Kajdacsy-Balla, and R. Bhargava, Proc. Natl. Acad. Sci. **115**, E5651 (2018).

129. S. Junaid, S. C. Kumar, M. Mathez, M. Hermes, N. Stone, N. Shepherd, M. Ebrahim-Zadeh, P. Tidemand-Lichtenberg, and C. Pedersen, Optica **6**, 702 (2019).

130. W. B. Jackson, N. M. Amer, A. C. Boccara, and D. Fournier, Appl. Opt. **20**, 1333 (1981).

131. M. D. Morris and K. Peck, Anal. Chem. **58**, 811A (1986).

132. Jiaqi. Wu, Takehiko. Kitamori, and Tsuguo. Sawada, Anal. Chem. **63**, 217 (1991).

133. Masaaki. Harada, Kouji. Iwamoto, Takehiko. Kitamori, and Tsuguo. Sawada, Anal. Chem. **65**, 2938 (1993).

134. D. Boyer, P. Tamarat, A. Maali, B. Lounis, and M. Orrit, Science **297**, 1160 (2002).

135. A. Gaiduk, P. V. Ruijgrok, M. Yorulmaz, and M. Orrit, Chem. Sci. **1**, 343 (2010).

136. E. Absil, G. Tessier, M. Gross, M. Atlan, N. Warnasooriya, S. Suck, M. Coppey-Moisan, and D. Fournier, Opt. Express **18**, 780 (2010).

137. D. Lasne, G. A. Blab, S. Berciaud, M. Heine, L. Groc, D. Choquet, L. Cognet, and B. Lounis, Biophys. J. **91**, 4598 (2006).

138. P. Zijlstra, P. M. R. Paulo, and M. Orrit, Nat. Nanotechnol. **7**, 379 (2012).

139. D. Lasne, G. A. Blab, F. D. Giorgi, F. Ichas, B. Lounis, and L. Cognet, Opt. Express **15**, 14184 (2007).

140. J. Miyazaki and Y. Toumon, Biomed. Opt. Express **10**, 5852 (2019).

141. J. Miyazaki, H. Tsurui, K. Kawasumi, and T. Kobayashi, Opt. Express **23**, 3647 (2015).

142. E. S. Lee and J. Y. Lee, Appl. Phys. Lett. **94**, 261101 (2009).

143. A. Mërtiri, T. Jeys, V. Liberman, M. K. Hong, J. Mertz, H. Altug, and S. Erramilli, Appl. Phys. Lett. **101**, 044101 (2012).

144. P. D. Samolis and M. Y. Sander, Opt. Express **27**, 2643 (2019).

145. D. Zhang, C. Li, C. Zhang, M. N. Slipchenko, G. Eakins, and J.-X. Cheng, Sci. Adv. **2**, e1600521 (2016).

146. Y. Bai, D. Zhang, L. Lan, Y. Huang, K. Maize, A. Shakouri, and J.-X. Cheng, Sci. Adv. **5**, eaav7127 (2019).

147. R. Chatterjee, I. M. Pavlovetc, K. Aleshire, G. V. Hartland, and M. Kuno, ACS Energy Lett. **3**, 469 (2018).

148. Z. Li, K. Aleshire, M. Kuno, and G. V. Hartland, J. Phys. Chem. B **121**, 8838 (2017).

149. I. M. Pavlovetc, K. Aleshire, G. V. Hartland, and M. Kuno, Phys. Chem. Chem. Phys. **22**, 4313 (2020).

150. C. Li, D. Zhang, M. N. Slipchenko, and J.-X. Cheng, Anal. Chem. **89**, 4863 (2017).

151. J. M. Lim, C. Park, J.-S. Park, C. Kim, B. Chon, and M. Cho, J. Phys. Chem. Lett. **10**, 2857 (2019).

152. D. Zhang, L. Lan, Y. Bai, H. Majeed, M. E. Kandel, G. Popescu, and J.-X. Cheng, Light Sci. Appl. **8**, 116 (2019).

153. K. Toda, M. Tamamitsu, Y. Nagashima, R. Horisaki, and T. Ideguchi, Sci. Rep. **9**, 9957 (2019).

154. M. Schnell, S. Mittal, K. Falahkheirkhah, A. Mittal, K. Yeh, S. Kenkel, A. Kajdacsy-Balla, P. S. Carney, and R. Bhargava, Proc. Natl. Acad. Sci. **117**, 3388 (2020).

155. M. Tamamitsu, K. Toda, R. Horisaki, R. Horisaki, T. Ideguchi, and T. Ideguchi, Opt. Lett. **44**, 3729 (2019).

156. J. L. Abraham and E. S. Etz, Science **206**, 716 (1979).

157. A. Mahadevan-Jansen and R. R. Richards-Kortum, J. Biomed. Opt. **1**, 31 (1996).

158. R. Manoharan, Y. Wang, and M. S. Feld, Spectrochim. Acta. A. Mol. Biomol. Spectrosc. **52**, 215 (1996).

159. H. J. Butler, P. M. Brennan, J. M. Cameron, D. Finlayson, M. G. Hegarty, M. D. Jenkinson, D. S. Palmer, B. R. Smith, and M. J. Baker, Nat. Commun. **10**, 1 (2019).

160. C. Morasso, M. Truffi, R. Vanna, S. Albasini, S. Mazzucchelli, F. Colombo, L. Sorrentino, G. Sampietro, S. Ardizzone, and F. Corsi, J. Crohns Colitis **14**, 1572 (2020).

161. C. Otto, C. J. de Grauw, J. J. Duindam, N. M. Sijtsema, and J. Greve, J. Raman Spectrosc. **28**, 143 (1997).

162. A. Nijssen, T. C. Bakker Schut, F. Heule, P. J. Caspers, D. P. Hayes, M. H. A. Neumann, and G. J. Puppels, J. Invest. Dermatol. **119**, 64 (2002).

163. I. T. Jolliffe, in *Princ. Compon. Anal.*, edited by I. T. Jolliffe (Springer, New York, NY, 1986), pp. 129–155.

164. A. K. Jain and R. C. Dubes, Englewood Cliffs Prentice Hall 1988 (1988).

165. M. Stone, J. R. Stat. Soc. Ser. B Methodol. **36**, 111 (1974).

166. S. Koljenović, L.-P. Choo-Smith, T. C. B. Schut, J. M. Kros, H. J. van den Berge, and G. J. Puppels, Lab. Invest. **82**, 1265 (2002).

167. K. E. Shafer-Peltier, A. S. Haka, M. Fitzmaurice, J. Crowe, J. Myles, R. R. Dasari, and M. S. Feld, J. Raman Spectrosc. **33**, 552 (2002).

168. A. S. Haka, K. E. Shafer-Peltier, M. Fitzmaurice, J. Crowe, R. R. Dasari, and M. S. Feld, Proc. Natl. Acad. Sci. U. S. A. **102**, 12371 (2005).

169. G. Shetty, C. Kendall, N. Shepherd, N. Stone, and H. Barr, Br. J. Cancer **94**, 1460 (2006).

170. N. Amharref, A. Beljebbar, S. Dukic, L. Venteo, L. Schneider, M. Pluot, and M. Manfait, Biochim. Biophys. Acta BBA - Biomembr. **1768**, 2605 (2007).

171. M. Larraona-Puy, W. Perkins, I. H. Leach, A. A. Koloydenko, H. Williams, I. Notingher, S. Varma, A. Ghita, and A. Zoladek, J. Biomed. Opt. **14**, 054031 (2009).

172. M. D'Acunto, R. Gaeta, R. Capanna, and A. Franchi, Sci. Rep. **10**, 2155 (2020).

173. F. L. Cals, T. C. Bakker Schut, J. A. Hardillo, R. J. Baatenburg de Jong, S. Koljenović, and G. J. Puppels, Lab. Invest. **95**, 1186 (2015).

174. R. Vanna, C. Morasso, B. Marcinnò, F. Piccotti, E. Torti, D. Altamura, S. Albasini, M. Agozzino, L. Villani, L. Sorrentino, O. Bunk, F. Leporati, C. Giannini, and F. Corsi, Cancer Res. **80**, 1762 (2020).

175. K. Kong, C. J. Rowlands, S. Varma, W. Perkins, I. H. Leach, A. A. Koloydenko, H. C. Williams, and I. Notingher, Proc. Natl. Acad. Sci. **110**, 15189 (2013).

176. K. Kong, F. Zaabar, E. Rakha, I. Ellis, A. Koloydenko, and I. Notingher, Phys. Med. Biol. **59**, 6141 (2014).

177. D. W. Shipp, E. A. Rakha, A. A. Koloydenko, R. D. Macmillan, I. O. Ellis, and I. Notingher, Breast Cancer Res. **20**, 69 (2018).

178. X. Nan, E. O. Potma, and X. S. Xie, Biophys. J. **91**, 728 (2006).

179. Y. Fu, T. B. Huff, H.-W. Wang, H. Wang, and J.-X. Cheng, Opt. Express **16**, 19396 (2008).

180. C. L. Evans, E. O. Potma, M. Puoris'haag, D. Côté, C. P. Lin, and X. S. Xie, Proc. Natl. Acad. Sci. U. S. A. **102**, 16807 (2005).

181. J.-X. Cheng and X. S. Xie, Science **350**, (2015).

182. C. L. Evans and X. S. Xie, Annu. Rev. Anal. Chem. **1**, 883 (2008).

183. S. Yue and J.-X. Cheng, Curr. Opin. Chem. Biol. **33**, 46 (2016).

184. H. Wang, Y. Fu, P. Zickmund, R. Shi, and J.-X. Cheng, Biophys. J. **89**, 581 (2005).

185. T. T. Le, C. W. Rehrer, T. B. Huff, M. B. Nichols, I. G. Camarillo, and J.-X. Cheng, Mol. Imaging **6**, 7290.2007.00018 (2007).

186. T. Meyer, N. Bergner, C. Krafft, D. Akimov, B. Dietzek, J. Popp, C. Bielecki, B. F. M. Romeike, R. Reichart, and R. Kalff, J. Biomed. Opt. **16**, 021113 (2011).

187. E. Ploetz, S. Laimgruber, S. Berner, W. Zinth, and P. Gilch, Appl. Phys. B **87**, 389 (2007).

188. Y. Ozeki, F. Dake, S. Kajiyama, K. Fukui, and K. Itoh, Opt. Express **17**, 3651 (2009).

189. C. W. Freudiger, R. Pfannl, D. A. Orringer, B. G. Saar, M. Ji, Q. Zeng, L. Ottoboni, W. Ying, C. Waeber, J. R. Sims, P. L. De Jager, O. Sagher, M. A. Philbert, X. Xu, S. Kesari, X. S. Xie, and G. S. Young, Lab. Invest. **92**, 1492 (2012).

190. P. D. Chowdary, Z. Jiang, E. J. Chaney, W. A. Benalcazar, D. L. Marks, M. Gruebele, and S. A. Boppart, Cancer Res. **70**, 9562 (2010).

191. M. Ji, D. A. Orringer, C. W. Freudiger, S. Ramkissoon, X. Liu, D. Lau, A. J. Golby, I. Norton, M. Hayashi, N. Y. R. Agar, G. S. Young, C. Spino, S. Santagata, S. Camelo-Piragua, K. L. Ligon, O. Sagher, and X. S. Xie, Sci. Transl. Med. **5**, 201ra119 (2013).

192. O. Uckermann, R. Galli, S. Tamosaityte, E. Leipnitz, K. D. Geiger, G. Schackert, E. Koch, G. Steiner, and M. Kirsch, PLOS ONE **9**, e107115 (2014).

193. X. Zhang, M. B. J. Roeffaers, S. Basu, J. R. Daniele, D. Fu, C. W. Freudiger, G. R. Holtom, and X. S. Xie, ChemPhysChem **13**, 1054 (2012).

194. F.-K. Lu, S. Basu, V. Igras, M. P. Hoang, M. Ji, D. Fu, G. R. Holtom, V. A. Neel, C. W. Freudiger, D. E. Fisher, and X. S. Xie, Proc. Natl. Acad. Sci. **112**, 11624 (2015).

195. F.-K. Lu, D. Calligaris, O. I. Olubiyi, I. Norton, W. Yang, S. Santagata, X. S. Xie, A. J. Golby, and N. Y. R. Agar, Cancer Res. **76**, 3451 (2016).

196. S. Heuke, N. Vogler, T. Meyer, D. Akimov, F. Kluschke, H.-J. Röwert-Huber, J. Lademann, B. Dietzek, and J. Popp, Healthcare **1**, 64 (2013).

197. S. Heuke, O. Chernavskaia, T. Bocklitz, F. B. Legesse, T. Meyer, D. Akimov, O. Dirsch, G. Ernst, F. von Eggeling, I. Petersen, O. Guntinas–Lichius, M. Schmitt, and J. Popp, Head Neck **38**, 1545 (2016).

198. T. Meyer, O. Guntinas-Lichius, F. von Eggeling, G. Ernst, D. Akimov, M. Schmitt, B. Dietzek, and J. Popp, Head Neck **35**, E280 (2013).

199. E. Rodner, T. Bocklitz, F. von Eggeling, G. Ernst, O. Chernavskaia, J. Popp, J. Denzler, and O. Guntinas-Lichius, Head Neck **41**, 116 (2019).

200. D. A. Orringer, B. Pandian, Y. S. Niknafs, T. C. Hollon, J. Boyle, S. Lewis, M. Garrard, S. L. Hervey-Jumper, H. J. L. Garton, C. O. Maher, J. A. Heth, O. Sagher, D. A. Wilkinson, M. Snuderl, S. Venneti, S. H. Ramkissoon, K. A. McFadden, A. Fisher-Hubbard, A. P. Lieberman, T. D. Johnson, X. S. Xie, J. K. Trautman, C. W. Freudiger, and S. Camelo-Piragua, Nat. Biomed. Eng. **1**, 1 (2017).

201. L. Shamir, N. Orlov, D. M. Eckley, T. Macura, J. Johnston, and I. G. Goldberg, Source Code Biol. Med. **3**, 13 (2008).

202. T. C. Hollon, S. Lewis, B. Pandian, Y. S. Niknafs, M. R. Garrard, H. Garton, C. O. Maher, K. McFadden, M. Snuderl, A. P. Lieberman, K. Muraszko, S. Camelo-Piragua, and D. A. Orringer, Cancer Res. **78**, 278 (2018).

203. K. S. Shin, A. T. Francis, A. H. Hill, M. Laohajaratsang, P. J. Cimino, C. S. Latimer, L. F. Gonzalez-Cuyar, L. N. Sekhar, G. Juric-Sekhar, and D. Fu, Sci. Rep. **9**, 20392 (2019).

204. L. Zhang, Y. Wu, B. Zheng, L. Su, Y. Chen, S. Ma, Q. Hu, X. Zou, L. Yao, Y. Yang, L. Chen, Y. Mao, Y. Chen, and M. Ji, Theranostics **9**, 2541 (2019).

205. B. Sarri, R. Canonge, X. Audier, E. Simon, J. Wojak, F. Caillol, C. Cador, D. Marguet, F. Poizat, M. Giovannini, and H. Rigneault, Sci. Rep. **9**, 1 (2019).

206. T. C. Hollon, B. Pandian, A. R. Adapa, E. Urias, A. V. Save, S. S. S. Khalsa, D. G. Eichberg, R. S. D'Amico, Z. U. Farooq, S. Lewis, P. D. Petridis, T. Marie, A. H. Shah, H. J. L. Garton, C. O. Maher, J. A. Heth, E. L. McKean, S. E. Sullivan, S. L. Hervey-Jumper, P. G. Patil, B. G. Thompson, O. Sagher, G. M. McKhann, R. J. Komotar, M. E. Ivan, M. Snuderl, M. L. Otten, T. D. Johnson, M. B. Sisti, J. N. Bruce, K. M. Muraszko, J. Trautman, C. W. Freudiger, P. Canoll, H. Lee, S. Camelo-Piragua, and D. A. Orringer, Nat. Med. **26**, 52 (2020).

207. H. Lin, H. J. Lee, N. Tague, J.-B. Lugagne, C. Zong, F. Deng, W. Wong, M. J. Dunlop, and J.-X. Cheng, Nat. Commun. **12**, 3052 (2021).

208. E. R. Blout and R. C. Mellors, Science **110**, 137 (1949).

209. D. L. Woernley, Cancer Res. **12**, 516 (1952).

210. A. Barth, Biochim. Biophys. Acta BBA - Bioenerg. **1767**, 1073 (2007).

211. G. Bellisola and C. Sorio, Am. J. Cancer Res. **2**, 1 (2011).

212. M. Diem, S. Boydston-White, and L. Chiriboga, Appl. Spectrosc. **53**, 148A (1999).

213. F. Parker, *Applications of Infrared Spectroscopy in Biochemistry, Biology, and Medicine* (Springer Science & Business Media, 2012).

214. I. W. Levin and R. Bhargava, Annu. Rev. Phys. Chem. **56**, 429 (2004).

215. P. Lasch and D. Naumann, Cell. Mol. Biol. Noisy--Gd. Fr. **44**, 189 (1998).

216. E. N. Lewis, I. W. Levin, and P. J. Treado, US5377003A (27 December 1994).

217. L. H. Kidder, V. F. Kalasinsky, J. L. Luke, I. W. Levin, and E. N. Lewis, Nat. Med. **3**, 235 (1997).

218. H. Fabian, P. Lasch, M. Boese, and W. Haensch, Biopolymers **67**, 354 (2002).

219. P. Lasch, W. Haensch, E. N. Lewis, L. H. Kidder, and D. Naumann, Appl. Spectrosc. **56**, 1 (2002).

220. W. Steller, J. Einenkel, L.-C. Horn, U.-D. Braumann, H. Binder, R. Salzer, and C. Krafft, Anal. Bioanal. Chem. **384**, 145 (2006).

221. A. J. Sommer, L. G. Tisinger, C. Marcott, and G. M. Story, Appl. Spectrosc. **55**, 252 (2001).

222. M. J. Walsh, S. E. Holton, A. Kajdacsy-Balla, and R. Bhargava, Vib. Spectrosc. **60**, 23 (2012).

223. A. Benard, C. Desmedt, M. Smolina, P. Szternfeld, M. Verdonck, G. Rouas, N. Kheddoumi, F. Rothé, D. Larsimont, C. Sotiriou, and E. Goormaghtigh, Analyst **139**, 1044 (2014).

224. M. R. Kole, R. K. Reddy, M. V. Schulmerich, M. K. Gelber, and R. Bhargava, Anal. Chem. **84**, 10366 (2012).

225. P. Bassan, M. J. Weida, J. Rowlette, and P. Gardner, Analyst **139**, 3856 (2014).

226. M. J. Pilling, A. Henderson, and P. Gardner, Anal. Chem. **89**, 7348 (2017).

227. A. Mërtiri, A. Totachawattana, Hui Liu, M. K. Hong, T. Gardner, M. Y. Sander, and S. Erramilli, in *2014 Conf. Lasers Electro-Opt. CLEO - Laser Sci. Photonic Appl.* (2014), pp. 1–2.

228. A. Spadea, J. Denbigh, M. J. Lawrence, M. Kansiz, and P. Gardner, Anal. Chem. **93**, 3938 (2021).

229. T. Kobayashi, K. Nakata, I. Yajima, M. Kato, and H. Tsurui, Bioengineering **5**, 67 (2018).

230. A. Totachawattana, M. S. Regan, N. Y. R. Agar, N. Y. R. Agar, S. Erramilli, M. Y. Sander, and M. Y. Sander, in *Conf. Lasers Electro-Opt. 2017 Pap. ATu4A3* (Optical Society of America, 2017), p. ATu4A.3.

231. J. Sacharz, D. Perez-Guaita, M. Kansiz, S. S. Nazeer, A. Wesełucha-Birczyńska, S. Petratos, B. R. Wood, and P. Heraud, Anal. Methods **12**, 4334 (2020).

232. H. J. Byrne, M. Baranska, G. J. Puppels, N. Stone, B. Wood, K. M. Gough, P. Lasch, P. Heraud, J. Sulé-Suso, and G. D. Sockalingum, Analyst **140**, 2066 (2015).

233. J. M. Cameron, C. Rinaldi, S. H. Rutherford, A. Sala, A. G. Theakstone, and M. J. Baker, Appl. Spectrosc. 00037028211021846 (2021).

234. M. Jackson, Faraday Discuss. **126**, 1 (2004).

235. S. Tanwar, S. K. Paidi, R. Prasad, R. Pandey, and I. Barman, Spectrochim. Acta. A. Mol. Biomol. Spectrosc. **260**, 119957 (2021).

236. *The International Society for Clinical Spectroscopy - CLIRSPEC* (https://clirspec.org/, n.d.).

237. *Raman4clinics.Eu | Raman Spectroscopies for the Clinical Diagnostics* (https://www.raman4clinics.eu/, n.d.).

238. S. Fornasaro, F. Alsamad, M. Baia, L. A. E. Batista De Carvalho, C. Beleites, H. J. Byrne, A. Chiadò, M. Chis, M. Chisanga, A. Daniel, J. Dybas, G. Eppe, G. Falgayrac, K. Faulds, H. Gebavi, F. Giorgis, R. Goodacre, D. Graham, P. La Manna, S. Laing, L. Litti, F. M. Lyng, K. Malek, C. Malherbe, M. P. M. Marques, M. Meneghetti, E. Mitri, V. Mohaček-Grošev, C. Morasso, H. Muhamadali, P. Musto, C. Novara, M. Pannico, G. Penel, O. Piot, T. Rindzevicius, E. A. Rusu, M. S. Schmidt, V. Sergo, G. D. Sockalingum, V. Untereiner, R. Vanna, E. Wiercigroch, and A. Bonifacio, Anal. Chem. **92**, 4053 (2020).

239. S. Guo, C. Beleites, U. Neugebauer, S. Abalde-Cela, N. K. Afseth, F. Alsamad, S. Anand, C. Araujo-Andrade, S. Aškrabić, E. Avci, M. Baia, M. Baranska, E. Baria, L. A. E. Batista de Carvalho, P. de Bettignies, A. Bonifacio, F. Bonnier, E. M. Brauchle, H. J. Byrne, I. Chourpa, R. Cicchi, F. Cuisinier, M. Culha, M. Dahms, C. David, L. Duponchel, S. Duraipandian, S. F. El-Mashtoly, D. I. Ellis, G. Eppe, G. Falgayrac, O. Gamulin, B. Gardner, P. Gardner, K. Gerwert, E. J. Giamarellos-Bourboulis, S. Gizurarson, M. Gnyba, R. Goodacre, P. Grysan, O. Guntinas-Lichius, H. Helgadottir, V. M. Grošev, C. Kendall, R. Kiselev, M. Kölbach, C. Krafft, S. Krishnamoorthy, P. Kubryck, B. Lendl, P. Loza-Alvarez, F. M. Lyng, S. Machill, C. Malherbe, M. Marro, M. P. M. Marques, E. Matuszyk, C. F. Morasso, M. Moreau, H. Muhamadali, V. Mussi, I. Notingher, M. Z. Pacia, F. S. Pavone, G. Penel, D. Petersen, O. Piot, J. V. Rau, M. Richter, M. K. Rybarczyk, H. Salehi, K. Schenke-Layland, S. Schlücker, M. Schosserer, K. Schütze, V. Sergo, F. Sinjab, J. Smulko, G. D. Sockalingum, C. Stiebing, N. Stone, V. Untereiner, R. Vanna, K. Wieland, J. Popp, and T. Bocklitz, Anal. Chem. **92**, 15745 (2020).